Title

Dissecting the Spire/Cappuccino interactome and its role in Drosophila oogenesis

ISBN

9798190906431

Author

Wu, Carolyn

Publication Date

2026-09-04

Peer reviewed|Thesis/dissertation

UNIVERSITY OF CALIFORNIA

Los Angeles

Dissecting the Spire/Cappuccino interactome and its role in *Drosophila* oogenesis

A dissertation submitted in partial satisfaction of the

requirements for the degree Doctor of Philosophy

in Biochemistry, Molecular, and Structural Biology

by

Carolyn Wu

2026

ABSTRACT OF THE DISSERTATION

Dissecting the Spire/Cappuccino interactome and its role in *Drosophila* oogenesis

by

Carolyn Wu

Doctor of Philosophy in Biochemistry, Molecular, and Structural Biology

University of California, Los Angeles, 2026

Professor Margot Elizabeth Quinlan, Co-chair

Professor James Akira Wohlschlegel, Co-chair

Actin networks are dynamic components of the cytoskeleton, present in all eukaryotic cells and responsible for many important cellular processes, including cell motility and cell division. Improper regulation of actin can lead to detrimental effects in embryology and development. In *Drosophila* egg development, an actin mesh is assembled by the collaboration of two actin nucleators, Spire (Spir) and Cappuccino (Capu). The persistence of this mesh during mid-oogenesis contributes to slow cytoplasmic streaming, and its subsequent disappearance during late-oogenesis leads to fast streaming. This transition from slow to fast streaming is critical for establishing polarity and future embryo patterning. Besides Spir and Capu, the molecular machinery and mechanisms governing the regulation of the actin mesh remain unknown. To gain deeper insight into the regulation of the mesh as well as Spir and Capu, we used TurboID-based proximity labeling and co-immunoprecipitation combined with quantitative mass

spectrometry to characterize the Spir/Capu interactome. These complementary methods not only validated well-established interactors but also uncovered many potential candidates, several of which we investigated. We focused specifically on Capu-associated proteins – Semaphorin-2a (Sema2a), Cut-up (Ctp), Homer, and TBC1D23.

We discovered that Sema2a associates with Capu and plays a previously unidentified role in oogenesis. Notably, Sema2a-nulls contain considerably smaller or undetectable ovaries, with egg chambers that do not develop past mid-oogenesis. Sema2a-nulls and Sema2a/Capu trans-heterozygote mutants exhibit decreased mesh density and disruption of *oskar (osk)* mRNA localization. Furthermore, preliminary data from fluorescence anisotropy and cross-linking mass spectrometry (XL-MS) demonstrate that Ctp binds directly to the N-terminal half of Capu. Ctp mutants as well as Homer and TBC1D23 mutants display *osk* mRNA displacements that are sensitive to Capu protein levels. Together, these findings offer valuable insight into the Capu interaction network and extend beyond its well-known association with Spir. Further elucidation into the novel, high-confidence interactors will allow deeper understanding of the complex and dynamic processes underlying oogenesis and potentially translate to mammalian systems where the same set of actin nucleators are used to build a similar actin network.

The dissertation of Carolyn Wu is approved.

Alvaro Sagasti

Ellen Sletten

Jorge Torres

Margot Elizabeth Quinlan, Committee Co-Chair

James Akira Wohlschlegel, Committee Co-Chair

University of California, Los Angeles

2026

谨以此论文献给我的家人,尤其是我的爸爸妈妈。

TABLE OF CONTENTS

List of figures

List of tables

Acknowledgements

I would like to thank my committee co-chairs, Professor Margot Quinlan and Professor James Wohlschlegel. Professor Quinlan has supported and helped me with everything, no matter how small the task was. She also always has so much faith in me and believes I can be capable of so much, even when I never think so. Professor Wohlschlegel has also helped me tremendously, and I could not have gotten this far without him. He really pushed my project forward and gave me the motivation to do better. I'm truly grateful to have two amazing professors and I appreciate all their support and guidance throughout the years.

Thank you to each member of my committee for all their feedback and enthusiasm for science. I would like to extend my gratitude particularly to Professor Sletten, who has been a part of my journey since undergrad. I gained so much from being in her lab, from presenting my first poster to being an author on a manuscript. Her mentorship has played a huge role in my success today.

To all the past and current members of the Quinlan lab – Hannah Bailey, Dylan Valencia, Bryan Christian, Merin Rixen, Peter Cullimore, Angela Koeberlein, and Josefina Reyes – thank you for the fun times we had during game nights, kbbq, white elephant, and many others. To Bryan for always being there for me when I needed help in science and in life. Thanks to him and his wife for treating me to dim sum and ice cream and for making things fun by trying to do the dances I suggest. To Merin for all the deep and fun conversations. We've had so many funny moments, especially in the fly room and at the fly conference, that I still laugh about when I think about them. To Peter for being the

reason that lab is more lively and for bringing out my peppy side. Thanks for all the chats and laughs we've shared over the years.

To the members of the Wohlschlegel lab – Hee Jong Kim, Vijaya Pandey, Adarsh Mayank, and Jihui Sha – for letting me bother them with so many questions and for all the advice and help they've given me. Hee Jong has been a great support, always listening to my rants and complaints even though he was probably tired of hearing me repeating the same things over and over again.

Thanks to Professor Emil Reisler for allowing me to use his lab and office space. He has been so welcoming that I've been in his lab almost every day for the past year. To Sudeepa Rajan, who has become a great friend that I eat lunch with and talk to every day. We can talk for so long that we sometimes don't know when to stop. We've also spent a lot of time outside of lab, eating at good restaurants and sightseeing places. Thanks also to Professor Orkun Akin and his lab for sharing reagents and microscopes. I never dreaded working in the dark, isolated microscope room because we always had fun chats.

To my childhood friend, Jamilla Abugazia, for her constant support and for all the amazing times we continue to share when we're both back in our hometown. To one of the best girlies, Alyssa Togle, for being with me through all the good and the bad. She's not only someone who's gotten me through difficult times, but she's also someone that I laugh so much with. To another amazing girlie, Luoting Zhuang, who has continued to support me since the very first day of undergrad. All of the times we've spent eating good food, going to cool places around LA, and taking recreational classes together have really made life more enjoyable. To Thaksaporn Chitrakorn and Melinda Liu, who are on the

east coast but continue to support me despite the distance. To Nikki Cheung, who has made grad school more fun by playing tennis or pickleball, watching basketball games, and even running 5k races together. To all my friends that have been a part of any chapter of my life.

Most importantly, I thank my family, who I would not have been able to do this without. To my grandma and brother for taking care of me and for always being people I can rely on. To my dad for always doing everything he can to support me, cooking me amazing food whenever I'm back home, and being so proud of me and my brother. To my mom, who is my number 1 bestie and supporter. She's someone I've always looked up to, and I hope that someday I become half the person she is.

Just a note that Chapter 2 is a manuscript that is to be submitted and the preprint can be found on bioRxiv. Authors Sudeepa Rajan and Merin Rixen helped with gathering data for the pyrene assays and brightfield images of ovaries, respectively. Hee Jong Kim helped with the cross-linking mass spectrometry data shown in Chapter 3. Chapter 4 is a reprint of the manuscript as it appears in the Journal of Biological Chemistry. First author Kathryn Bremer led the project, and I was fortunate to have contributed to this work with the rest of the authors. Financial support for these works was provided by the UCLA Cell and Molecular Biology Training Program, which is supported by the NIH.

Vita

Education

M.S., Biochemistry, Molecular, and Structural Biology — March 2022
University of California, Los Angeles

B.S., Biochemistry with a Minor in Earth and Environmental Science — June 2020
University of California, Los Angeles

Research experience

Graduate Student Researcher — September 2024 – August 2026
Laboratory of Dr. James Wohlschlegel
Department of Biological Chemistry, David Geffen School of Medicine
University of California, Los Angeles

Graduate Student Researcher — March 2021 – August 2026
Laboratory of Dr. Margot Quinlan
Department of Chemistry and Biochemistry
University of California, Los Angeles

Undergraduate Researcher — June 2019 – June 2020
Laboratory of Dr. Ellen Sletten
Department of Chemistry and Biochemistry
University of California, Los Angeles

Publications

Wu C, Rajan S, Rixen M, Wohlschlegel JA, Quinlan ME. The Cappuccino interactome reveals an intracellular role for Semaphorin-2a in *Drosophila* oogenesis. Manuscript to be submitted. BioRxiv preprint: doi.org/10.64898/2026.05.11.724452

Bremer KV, **Wu C**, Patel AA, He KL, Grunfeld AM, Chanfreau GF, Quinlan ME. Formin tails act as a switch, inhibiting or enhancing processive actin elongation. J Biol Chem. 2024 Jan;300(1):105557. doi:10.1016/j.jbc.2023.105557. Epub 2023 Dec 12. PMID: 38097186; PMCID: PMC10797183.

Li L, El Khoury A, Clement BO, **Wu C**, Harran PG. Asymmetric Organocatalysis Enables Rapid Assembly of Portimine Precursor Chains. Org Lett. 2022 Apr 15;24(14):2607-2612. doi: 10.1021/acs.orglett.2c00556. Epub 2022 Apr 4. PMID: 35377667.

Day RA, Estabrook DA, **Wu C**, Chapman JO, Togle AJ, Sletten EM. Systematic Study of Perfluorocarbon Nanoemulsions Stabilized by Polymer Amphiphiles. ACS Appl Mater Interfaces. 2020 Sep 2;12(35):38887- 38898. doi: 10.1021/acsami.0c07206. Epub 2020 Aug 24. PMID: 32706233; PMCID: PMC8341393.

Awards

Herbert Newby McCoy Commencement Award, *April 2026*
Roberts A. Smith Excellence in Research Award, *May 2025*
John Stauffer Excellence in Second Year Academics and Research Award, *May 2023*
UCLA Cell and Molecular Biology Training Program, *July 2022*
National Science Foundation Graduate Research Fellowship Program Honorable Mention, *April 2022*
Geissman Award for Outstanding Achievement in Organic Chemistry, *June 2020*
Lorraine H. and Masuo Toji Fund Summer Research Fellowship, *March 2019*
Dean's Honors List, *Spring 2018 – Spring 2020*
Certification of Proficiency in Sports Medicine 1*, June 2016*
Presidents Education Awards Program Outstanding Academic Excellence*, 2016*
AP Scholar With Distinction Award, *August 2015*
Junior Honor Guard, *June 2015*
California Scholarship Federation, *April 2014 – June 2016*

Mentorship

Nathan Muck, Graduate, Biochemistry, Molecular, and Structural Biology	Winter 2026
Peter Cullimore, Graduate, Cellular and Developmental Biology	Spring 2023
Evan Clark, Graduate, Biochemistry, Biophysics, and Structural Biology	Spring 2023
Angel Arce, Graduate, Biochemistry, Molecular, and Structural Biology	Fall 2021

Teaching

TA – Chem 14CL	Winter 2026
TA – Chem 153A	Spring 2021
TA – Chem 153A	Winter 2021

Chapter 1: Introduction

The cytoskeleton

The cytoskeleton is essential for many biological processes, including cell division, cell morphology, and intracellular transport. Three cytoskeletal networks exist to give cells their shape and drive motility – actin, microtubules, and intermediate filaments. The polymerization and depolymerization of actin and microtubules allow for changes in cell shape and organization. The structural polarity of these cytoskeletal components also permits the movement of motor proteins, such as kinesin and myosin, that are responsible for intracellular transport (Pollard, 2003; Fletcher and Mullins, 2010). Intermediate filaments, on the other hand, do not have polarity, cannot use molecular motors, and mainly interact with actin and microtubules (Pollard, 2003; Fletcher and Mullins, 2010). The integrated network of all three cytoskeletal components is important in cellular structure and function during embryogenesis (Lim and Plachta, 2021). One ideal model system to study development and the cytoskeleton is *Drosophila melanogaster*, or the fruit fly, due to its completely sequenced genome, relatively facile genetic manipulation, and short generation times (Adams et al., 2000; Venken et al., 2016; Victor Atoki et al., 2025). *Drosophila* oogenesis, in particular, has been used extensively to study cell polarity, intercellular transport, and cytoskeletal regulation, all of which are required for cell survival and growth (Hudson and Cooley, 2014).

Drosophila oogenesis

Drosophila oogenesis occurs in the ovaries, which are composed of approximately 18 ovarioles. Within each ovariole are egg chambers that consist of 15 nurse cells and 1 oocyte (Bastock and Johnston, 2008; Bor et al., 2015; Quinlan, 2016). These egg

chambers are connected to each other, with increasing developmental stages (1-14) toward the posterior end (**Figure 1-1**). Nurse cells produce necessary RNAs and proteins that are transported into the oocyte through ring canals (Bastock and Johnston, 2008). During early oogenesis (stages 1-6), a microtubule network called the microtubule-organizing center (MTOC) extends from the oocyte to the nurse cells in order to transport key polarity determinants, such as *bicoid* (*bcd*), *oskar* (*osk*), *gurken* (*grk*), and *nanos* (*nos*) mRNA, into the oocyte (Johnstone and Lasko, 2001; Theurkauf et al., 1992).

By mid-oogenesis (stages 7-10A), microtubules rearrange to form a gradient from the anterior to the posterior pole of the oocyte. This new microtubule organization asymmetrically localizes *bcd* mRNA to the anterior of the oocyte and directs some *osk* mRNA to the posterior, thereby forming the anterior-posterior axes of the oocyte. The rest of the *osk* mRNA is transported by diffusion and slow cytoplasmic streaming (Serbus et al., 2005; Ganguly et al., 2012; Khuc Trong et al., 2015). The microtubule network also directs *grk* to the anterior-dorsal corner, where it patterns the dorsal-ventral axes of the oocyte (Thio et al., 2000).

In the late stages of oogenesis (stages 10B-14), *nos* is localized to the posterior after nurse cells transfer their cytoplasm in a process called “dumping” (Johnstone and Lasko, 2001; Dahlgaard et al., 2007). During this time, microtubules form parallel arrays at the cortex of the oocyte. The plus-end directed motor, Kinesin, moves along the anchored microtubules and also slides free microtubules to generate the force required for fast cytoplasmic streaming, with flows that are approximately 10 times faster than slow streaming (Palacios and St Johnston, 2002; Lu et al., 2016; Dahlgaard et al., 2007; Quinlan, 2016). This streaming enhances the localization and maintenance of *nos* at the

posterior end. While the role of microtubules is well-characterized, the function of the actin cytoskeleton is more elusive.

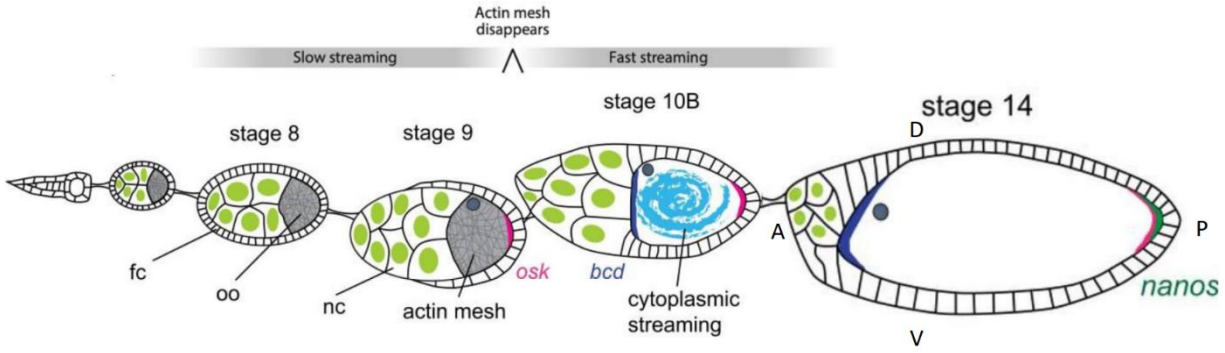

Figure 1-1. Schematic of Drosophila oogenesis. Oogenesis is divided into 14 stages based on morphological features, with stages 1-6 as early oogenesis, 7-10A as mid-oogenesis, and 10B-14 as late-oogenesis. Abbreviations: fc, follicle cells; oo, oocyte; nc, nurse cells; osk, oskar mRNA; bcd, bicoid mRNA; A, anterior; P, posterior; D, dorsal; V, ventral. (Adapted from Bor et al., 2015)

Spir and Capu cooperate to build the actin mesh

During mid-oogenesis, an isotropic actin mesh is established that maintains the microtubule arrangement and slows cytoplasmic streaming, which is essential for transporting and localizing polarity determinants. There are a few models in which the mesh is proposed to contribute to slow streaming: increasing the viscosity of the oocyte to resist fluid flows, cross-linking microtubules to maintain microtubule architecture, or limiting the motion of Kinesin-transported cargo (Quinlan, 2016; Dahlgaard et al., 2007). During late-oogenesis, this mesh disappears, leading to fast, microtubule-dependent streaming (Dahlgaard et al., 2007). Absence of this mesh during mid-oogenesis results in premature fast streaming, and persistence of this mesh past mid-oogenesis prevents fast streaming (Dahlgaard et al., 2007; Bor et al., 2015; Theurkauf, 1994). In both cases, localization of *osk, grk,* and *nanos* mRNA is disrupted, ultimately leading to loss of

polarity, fertility, and defects in the future embryo (Dahlgaard et al., 2007; Bor et al., 2015; Theurkauf, 1994; Lantz et al., 1999; Quinlan, 2016).

The loss of actin mesh and onset of premature streaming were found in *spire (spir)*, *cappuccino (capu)*, and *chickadee (chic)* mutants, suggesting that these genes are required to build the mesh (Dahlgaard et al. 2007; Quinlan, 2013; Manseau and Schüpbach, 1989). Consistent with this earlier hypothesis, Spir and Capu collaborate synergistically to assemble the mesh (Rosales-Nieves et al., 2006; Quinlan, 2013; Dahlgaard et al. 2007; Montaville et al., 2014; Bradley et al., 2020). Spir is a member of the WASP homology 2 (WH2) family of nucleators and as the name suggests, contains a cluster of four WH2 domains that facilitates actin nucleation from the slow-growing pointed end of actin filaments (Quinlan et al., 2005). It also consists of the kinase inactive domain (KIND) that is necessary to bind Capu (**Figure 1-2**; Quinlan et al, 2007; Vizcarra et al., 2011). Capu is a member of the Formin family of nucleators defined by the well-conserved formin homology 2 (FH2) and proline-rich FH1 domains, which mediates actin nucleation by remaining processively bound to the fast-growing barbed end of filaments and promotes actin elongation by capturing profilin-actin and delivering it to the barbed end of filaments, respectively (Higgs and Peterson, 2005; Goode and Eck, 2007; Pruyne et al., 2002). In addition to the FH1 and FH2 domains that stimulate actin polymerization, Capu contains a distinct N-terminal Capu inhibitory domain (CID) and C-terminal tail that both function in inhibiting actin polymerization (**Figure 1-2**). The intramolecular interaction between the CID and tail serves as an autoinhibitory mechanism, ensuring that Capu remains in an inactive, closed state when necessary (Bor et al., 2012).

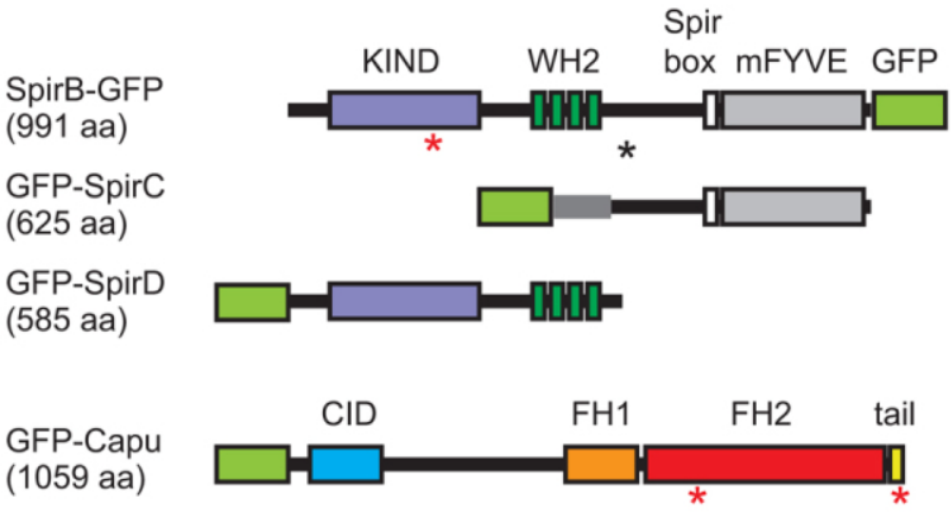

Figure 1-2. Spir and Capu domains. Spir consists of the KIND, WH2 and mFYVE domains. Capu is comprised of the CID, FH1, FH2, and tail domains. Abbreviations: KIND = Kinase non-catalytic C-lobe domain; WH2: Wiscott-Aldrich homology 2; mFYVE: modified Fab1/YOTB/Vac1/EEA1 zinc-binding domain; CID: Capu inhibitory domain; FH1: Formin homology 1; FH2: Formin homology 2. (Adapted from Quinlan, 2013)**.**

Spir cannot form an actin mesh in the absence of Capu, but Capu can induce a significantly less dense mesh in the absence of Spir, consistent with a model in which they synergize (Dahlgaard et al., 2007). Detailed analysis from *in vitro* and *in vivo* studies have shown that the Spir KIND domain interacts directly with the Capu tail (Vizcarra et al., 2011, Quinlan et al., 2013). Structural and biochemical assays show that the point mutation Y232K in the Spir KIND domain completely eliminates the KIND/tail binding, no longer able to promote the dissociation of Capu from the barbed-end of the actin filament and prevent Capu-mediated nucleation and polymerization (Vizcarra et al., 2011). Similarly, the point mutation L1048A in the Capu tail abolishes the KIND/tail interaction and prevents the KIND from inhibiting Capu-mediated polymerization (Vizcarra et al., 2011). The same point mutations Spir(Y232K) and Capu(L1048) also have implications *in vivo,* as flies expressing these mutations have no detectable actin mesh, exhibit

premature fast streaming, and loss of fertility (Quinlan, 2013). Together, these investigations give rise to models in which Spir and Capu must interact directly but also separate. One such model proposes that Spir and Capu interact to nucleate actin, and Spir is released from the complex, thereby freeing Capu to elongate actin (**Figure 1-3**; Quinlan, 2013; Bradley et al., 2019). Another model put forward is one called the "ping pong" mechanism, whereby Spir and Fmn2 (Capu ortholog) form transient complexes at the end of filaments in order to alternately release each other from the barbed ends (Montaville et al., 2014).

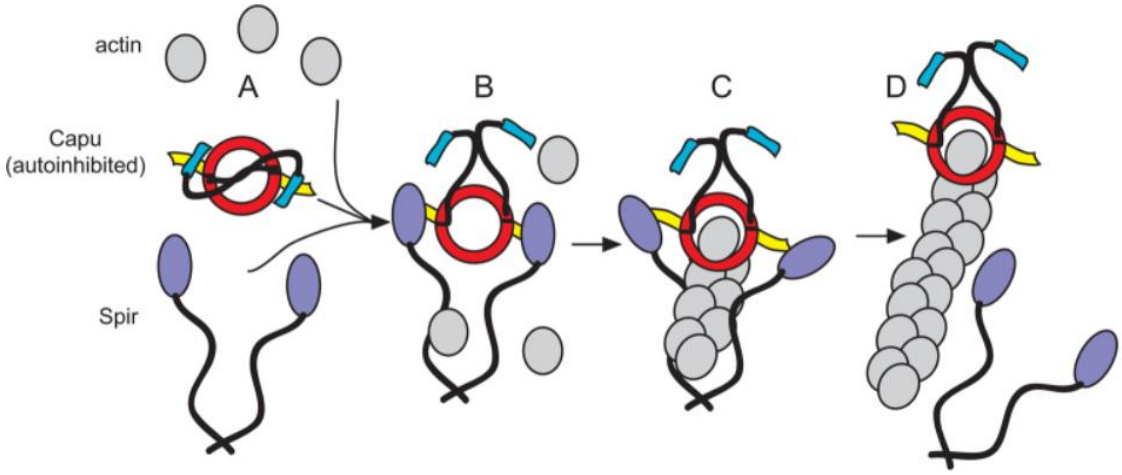

Figure 1-3. Model of Spir and Capu interaction in oogenesis. A) Spir and Capu on their own before any interaction. B) Spir and Capu interact directly. C) Spir and Capu promote actin nucleation. D) Spir dissociates from filament in order for Capu to elongate actin. (Adapted from Quinlan, 2013).

Because the timely assembly and disassembly of the actin mesh is important, it is necessary to investigate the regulation of Spir and Capu and their role in actin mesh removal. While it is well-established that Spir and Capu build the actin mesh, it remains unclear how the mesh is maintained and removed. Immunoblot experiments have revealed that the endogenous levels of both Spir and Capu decrease at similar levels

when the actin mesh is absent. By stage 11 of late-oogenesis, Spir and Capu levels drastically decrease to less than 10% of those in the whole ovary (Quinlan, 2013). The reduction in protein levels coincides with the disappearance of the actin mesh at this stage, indicating that Spir and Capu activity must be tightly regulated. However, further studies are required to determine the components and mechanisms behind Spir/Capu regulation as well as mesh maintenance and removal.

Methods to identify protein-protein interactions

Protein-protein interactions (PPI) are essential in biological and cellular processes. The various functions of proteins are attributed to their ability to form complexes and expansive networks. There are many methods (*in vitro, in vivo, in silico*) to map interactors and better understand protein function and regulation, including affinity purification, co-immunoprecipitation, Yeast 2 hybrid, and proximity labeling (Rao et al., 2014). Specifically, co-immunoprecipitation (co-IP) is a technique that allows the isolation of protein complexes ("prey") by using an antibody specific to the protein of interest (POI) ("bait") (Iqbal et al., 2018; Kim and Weidberg et al., 2025). The antibody is typically attached to solid substrates, such as agarose and magnetic beads, through antibody-binding proteins like Protein A/G. The antibody-bead complex can then be incubated with a solution containing the protein "bait". All unassociated proteins are removed through extensive washes, leaving behind the protein bait and its stable interactors (**Figure 1-4**). To identify interactors, co-immunoprecipitation can be combined with Sodium Dodecyl Sulfate-Polyacrylamide Gel Electrophoresis (SDS-PAGE) followed by Western blotting or mass spectrometry analysis.

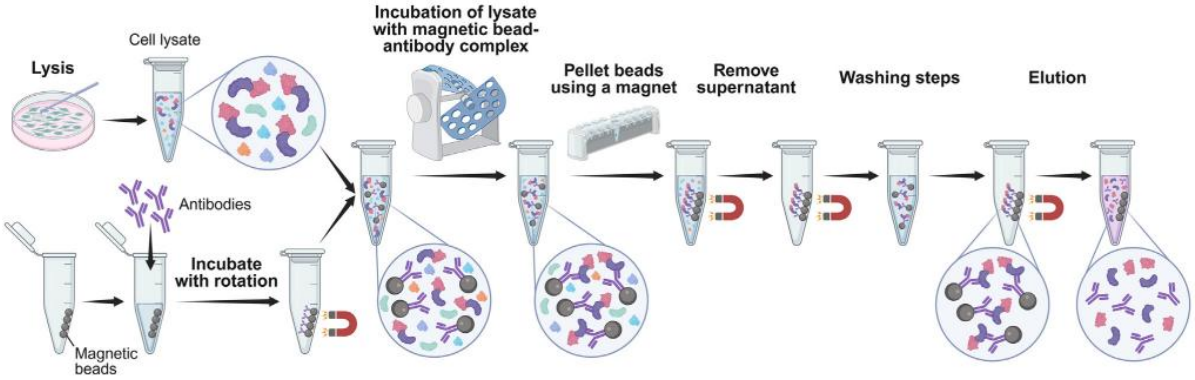

Figure 1-4. Workflow of co-immunoprecipitation. Cell lysate is incubated with antibody conjugated to magnetic beads. Flow-through is removed, extensive washing steps are performed, and finally, protein bait and its interactors are eluted (Adapted from Kim ad Weidberg, 2025).

A complementary approach to the traditional method of co-IP is proximity labeling, which utilizes an engineered enzyme fused to the POI to catalyze the biotinylation of proteins within a radius of ~10-20 nm of the POI (**Figure 1-5**). These engineered enzymes include peroxidases (HRP, APEX2) and biotin ligases (BioID2, TurboID, miniTurbo). Some advantages of horseradish peroxidase (HRP) and ascorbate peroxidase (APEX2) are high temporal resolution and very quick labeling times (~1 minute). However, some disadvantages include low sensitivity and the use of reagents (digitonin and hydrogen peroxide) that are toxic to living cells (Kotani et al., 2008; Lam et al. 2015). In contrast, biotin ligases are non-toxic and only require either endogenous or exogenous biotin to catalyze the reaction. However, the early biotin ligases (BioID and BioID2) require at least 18 hours for labeling, and there is poor temporal resolution as a result of low catalytic activity (Roux et al., 2012; May and Roux, 2019; Rao et al., 2014). The next generation

of biotin ligases, TurboID and miniTurbo, need only 10 minutes for labeling and have the highest catalytic activity (Branon et al., 2018). In contrast to co-IPs that could miss more weak interactions, proximity labeling captures both transient and stable interactions. Both co-IPs and TurboID downstream workflows involve SDS-PAGE followed by immunoblotting or mass spectrometry.

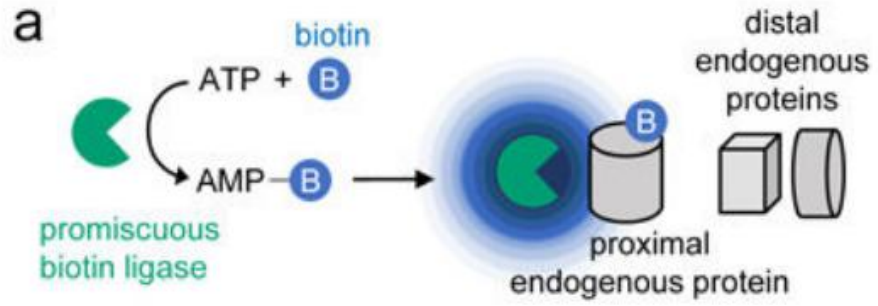

Figure 1-5. Biotinylation of proximal proteins catalyzed by biotin ligases. a) Biotin ligases use ATP and biotin to form biotin-5'-AMP-hydride, which reacts and forms a covalent bond with the lysines of proximal proteins (Adapted from Branon et al., 2018).

Overview of the dissertation

We used co-immunoprecipitation and TurboID-mediated proximity labeling coupled with quantitative mass spectrometry to extract the Spir/Capu interactome and better understand both Spir/Capu and actin mesh regulation. Using these complementary approaches, we discovered a novel Capu-binding protein, Semaphorin-2A (Sema2a), which has been extensively studied in the central nervous system (CNS). We find that Sema2a plays a previously unestablished role in oogenesis that is independent of Plexin-B (PlexB), its receptor in the CNS (**Chapter 2**). Preliminary results also provide better understanding of other Capu-binding proteins, namely Ctp, Homer, and TBC1D23

(**Chapter 3**). In addition, we delved into the role of formin tails and their effects on actin polymerization (**Chapter 4**).

References

Adams, M. D., Celniker, S. E., Holt, R. A., Evans, C. A., Gocayne, J. D., Amanatides, P. G., Scherer, S. E., Li, P. W., Hoskins, R. A., Galle, R. F., George, R. A., Lewis, S. E., Richards, S., Ashburner, M., Henderson, S. N., Sutton, G. G., Wortman, J. R., Yandell, M. D., Zhang, Q., Chen, L. X., … Venter, J. C. (2000). The genome sequence of Drosophila melanogaster. *Science (New York, N.Y.)*, 287, 2185–2195.

Bastock, R. and Johnston, D.S. (2008). Drosophila oogenesis. Current Biology, 18, PR1082 R1087.

Bor, B. et al. (2015). Regulation of formin Cappuccino is critical for polarity of Drosophila oocytes. Cytoskeleton, 72, 1-15.

Bor, B., Vizcarra, C. L., Phillips, M. L., & Quinlan, M. E. (2012). Autoinhibition of the formin Cappuccino in the absence of canonical autoinhibitory domains. *Molecular biology of the cell*, 23, 3801–3813.

Bradley, A. O., Vizcarra, C. L., Bailey, H. M., & Quinlan, M. E. (2020). Spire stimulates nucleation by Cappuccino and binds both ends of actin filaments. *Molecular biology of the cell*, 31, 273–286.

Branon, T. C., Bosch, J. A., Sanchez, A. D., Udeshi, N. D., Svinkina, T., Carr, S. A., Feldman, J. L., Perrimon, N., & Ting, A. Y. (2018). Efficient proximity labeling in living cells and organisms with TurboID. *Nature biotechnology*, 36, 880–887.

Dahlgaard, K. et al. (2007). Capu and Spire Assemble a Cytoplasmic Actin Mesh that Maintains Microtubule Organization in the Drosophila Oocyte. Dev Cell. 13, 539-553.

Fletcher, D.A. and Mullins, R.D. (2010). Cell mechanics and the cytoskeleton. *Nature*, 463, 485-492.

Ganguly, S., Williams, L. S., Palacios, I. M., & Goldstein, R. E. (2012). Cytoplasmic streaming in Drosophila oocytes varies with kinesin activity and correlates with the microtubule cytoskeleton architecture. *Proceedings of the National Academy of Sciences of the United States of America*, 109, 15109–15114.

Goode, B.L., and Eck, M.J. (2007) Mechanism and function of formins in the control of actin assembly. *Annu. Rev. Biochem.* **76**, 593-627

Higgs, H. N., and Peterson, K. J. (2005). Phylogenetic analysis of the formin homology 2 domain. *Molecular biology of the cell*, 16, 1–13.

Hudson, A.M. and Cooley, L. (2014). Methods for studying oogenesis. *Methods*. 68, 207-217.

Iqbal, H., Akins, D. R., & Kenedy, M. R. (2018). Co-immunoprecipitation for Identifying Protein-Protein Interactions in Borrelia burgdorferi. *Methods in molecular biology (Clifton, N.J.)*, 1690, 47–55.

Johnstone, O. and Lasko, P. (2001). Translational Regulation and RNA Localization in Drosophila Oocytes and Embryos. Annual Review of Genetics, 35, 365-406.

Khuc Trong, P., Doerflinger, H., Dunkel, J., St Johnston, D., & Goldstein, R. E. (2015). Cortical microtubule nucleation can organise the cytoskeleton of Drosophila oocytes to define the anteroposterior axis. *eLife*, 4, e06088.

Kim, J., & Weidberg, H. (2025). Protocol for assessing the clogging of the mitochondrial translocase of the outer membrane by precursor proteins in human cells. *STAR protocols*, *6*, 103617.

Kotani, N., Gu, J., Isaji, T., Udaka, K., Taniguchi, N., & Honke, K. (2008). Biochemical visualization of cell surface molecular clustering in living cells. *Proceedings of the National Academy of Sciences of the United States of America*, 105, 7405–7409.

Lam, S. S., Martell, J. D., Kamer, K. J., Deerinck, T. J., Ellisman, M. H., Mootha, V. K., & Ting, A. Y. (2015). Directed evolution of APEX2 for electron microscopy and proximity labeling. *Nature methods*, 12, 51–54.

Lantz, V. A., Clemens, S. E., & Miller, K. G. (1999). The actin cytoskeleton is required for maintenance of posterior pole plasm components in the Drosophila embryo. *Mechanisms of development*, 85, 111–122.

Lim, H.Y.G and Plachta, N. (2021). Cytoskeletal control of early mammalian development. *Nature Reviews Molecular Cell Biology*, 22, 548-562.

Lu, W., Winding, M., Lakonishok, M., Wildonger, J., & Gelfand, V. I. (2016). Microtubule-microtubule sliding by kinesin-1 is essential for normal cytoplasmic streaming in Drosophila oocytes. *Proceedings of the National Academy of Sciences of the United States of America*, 113, E4995–E5004.

Manseau, L. J., & Schüpbach, T. (1989). cappuccino and spire: two unique maternal-effect loci required for both the anteroposterior and dorsoventral patterns of the Drosophila embryo. *Genes & development*, 3, 1437–1452.
May, D. G., & Roux, K. J. (2019). BioID: A Method to Generate a History of Protein Associations. *Methods in molecular biology (Clifton, N.J.)*, 2008, 83–95.

Montaville, P., Jégou, A., Pernier, J., Compper, C., Guichard, B., Mogessie, B., Schuh, M., Romet-Lemonne, G., & Carlier, M. F. (2014). Spire and Formin 2 synergize and antagonize in regulating actin assembly in meiosis by a ping-pong mechanism. *PLoS biology*, 12, e1001795.

Palacios, I. M., & St Johnston, D. (2002). Kinesin light chain-independent function of the Kinesin heavy chain in cytoplasmic streaming and posterior localisation in the Drosophila oocyte. *Development (Cambridge, England)*, 129, 5473–5485.

Pollard, T.D. (2003). The cytoskeleton, cellular motility and the reductionist agenda. *Nature*, 422, 741-745.

Pruyne, D., Evangelista, M., Yang, C., Bi, E., Zigmond, S., Bretscher, A., & Boone, C. (2002). Role of formins in actin assembly: nucleation and barbed-end association. *Science (New York, N.Y.)*, 297, 612–615.

Quinlan M. E. (2013). Direct interaction between two actin nucleators is required in Drosophila oogenesis. *Development (Cambridge, England)*, 140, 4417–4425.

Quinlan, M. E., Heuser, J. E., Kerkhoff, E., & Mullins, R. D. (2005). Drosophila Spire is an actin nucleation factor. *Nature*, 433, 382–388.

Quinlan, M. E., Hilgert, S., Bedrossian, A., Mullins, R. D., & Kerkhoff, E. (2007). Regulatory interactions between two actin nucleators, Spire and Cappuccino. *The Journal of cell biology*, 179, 117–128.

Quinlan, M.E. (2016). Cytoplasmic Streaming in the Drosophila Oocyte. Annual Review of Cell and Developmental Biology, 32, 173-195.

Rao, V. S., Srinivas, K., Sujini, G. N., & Kumar, G. N. (2014). Protein-protein interaction detection: methods and analysis. *International journal of proteomics*, 2014, 147648.

Rosales-Nieves, A.E., Johndrow, J.E., Keller, L.C., Magie, C.R., Pinto-Santini, D.M., Parkhurst, S.M. (2006). Coordination of microtubule and microfilament dynamics by Drosophila Rho1, Spire and Cappuccino. *Nat Cell Biol,* 8, 367–76.

Roux, K. J., Kim, D. I., Raida, M., & Burke, B. (2012). A promiscuous biotin ligase fusion protein identifies proximal and interacting proteins in mammalian cells. *The Journal of cell biology*, 196, 801–810.

Serbus, L. R., Cha, B. J., Theurkauf, W. E., & Saxton, W. M. (2005). Dynein and the actin cytoskeleton control kinesin-driven cytoplasmic streaming in Drosophila oocytes. *Development (Cambridge, England)*, 132, 3743–3752.

Theurkauf W. E. (1994). Microtubules and cytoplasm organization during Drosophila oogenesis. *Developmental biology*, *165*(2), 352–360.

Theurkauf, W. E., Smiley, S., Wong, M. L., & Alberts, B. M. (1992). Reorganization of the cytoskeleton during Drosophila oogenesis: implications for axis specification and intercellular transport. *Development (Cambridge, England)*, 115, 923–936.

Thio, G. L., Ray, R. P., Barcelo, G., & Schüpbach, T. (2000). Localization of gurken RNA in Drosophila oogenesis requires elements in the 5' and 3' regions of the transcript. *Developmental biology*, 221, 435–446.

Venken, K. J., Sarrion-Perdigones, A., Vandeventer, P. J., Abel, N. S., Christiansen, A. E., & Hoffman, K. L. (2016). Genome engineering: Drosophila melanogaster and beyond. *Wiley interdisciplinary reviews. Developmental biology*, 5, 233–267.

Victor Atoki, A., Aja, P. M., Shinkafi, T. S., Ondari, E. N., Adeniyi, A. I., Fasogbon, I. V., Dangana, R. S., Shehu, U. U., & Akin-Adewumi, A. (2025). Exploring the versatility of *Drosophila melanogaster* as a model organism in biomedical research: a comprehensive review. *Fly*, 19, 2420453.

Vizcarra, C.L., Kreutz, B., Rodal, A.A., Toms, A.V., Lu, J., Zheng, W., Quinlan, M.E., Eck, M.J., (2011). Structure and function of the interacting domains of Spire and Fmn-family formins. *Proc. Natl. Acad. Sci*. 108, 11884–11889.

Chapter 2: The Cappuccino interactome reveals an intracellular role for Semaphorin-2a in *Drosophila* oogenesis

The Cappuccino interactome reveals an intracellular role for Semaphorin-2a in *Drosophila* oogenesis

Running title: Capu and Sema2a interaction in the oocyte

Carolyn Wu[1], Sudeepa Rajan[1], Merin Rixen[1], James Wohlschlegel[2,3*], Margot Elizabeth Quinlan[1,3*]

[1]Department of Chemistry and Biochemistry, University of California Los Angeles, 607 Charles E. Young Drive, Los Angeles, CA 90095
[2]Department of Biological Chemistry, David Geffen School of Medicine, University of California, Los Angeles, CA 90095
[3]Molecular Biology Institute, University of California Los Angeles, 611 Charles E. Young Drive, Los Angeles, CA 90095

[*]Co-corresponding authors: jwohl@ucla.edu and margot@chem.ucla.edu

Summary

This study reveals a novel interaction between the actin nucleator Cappuccino and the typically secreted neural guidance factor Semaphorin-2a. It is shown that Semaphorin-2a inhibits the actin polymerization activity of Cappuccino *in vitro* and plays an intracellular role in oogenesis.

Abstract

The spatiotemporal regulation of an actin mesh during *Drosophila* oogenesis is essential for proper localization of cell polarity determinants that establish the future patterning of the embryo. Here, we reveal an unexpected role for Semaphorin-2a (Sema2a) in actin mesh regulation and oogenesis. Sema2a classically functions as a secreted guidance cue that binds its cognate Plexin-B (PlexB) receptor to establish neural circuits. In contrast, we find that Sema2a is expressed inside the germarium, germline, and follicle cells of the developing ovary. Sema2a mutants possess small ovaries that fail to develop past mid-oogenesis. We demonstrate that Sema2a interacts with Cappuccino (Capu), a key actin nucleator crucial for building the actin mesh in *Drosophila* oocytes. Sema2a inhibits the actin assembly activity of Capu *in vitro*. Furthermore, genetic interaction between Sema2a and Capu influences mesh density and disrupts *oskar* mRNA localization. PlexB mutants, however, exhibit wild-type size ovaries with *osk*ar mRNA localization distinct from Sema2a mutants, confirming the non-canonical role of Sema2a in oogenesis.

Introduction

Proper regulation of actin is crucial for egg development. For example, an isotropic actin mesh that fills the *Drosophila* oocyte during mid-oogenesis is critical to microtubule organization and polarity establishment (Dahlgaard et al., 2007). The mesh slows microtubule-driven cytoplasmic flows, facilitating proper transport of several mRNAs, including *oskar* (*osk), bicoid (bcd), gurken (grk), and nanos (nos),* that define the anterior-posterior and dorsal-ventral axes of the oocyte and future embryo. By late-oogenesis, the mesh disappears, and fast, microtubule-dependent streaming ensues (Dahlgaard et al., 2007). Disappearance of this mesh controls the transition from slow to fast streaming, during which cytoplasmic flows are approximately 10 times faster than slow streaming to allow efficient distribution of mRNAs and proteins as the oocyte increases in size (Quinlan, 2016). Understanding the molecular machinery and mechanisms underlying the dynamically regulated actin mesh is important because absence of the mesh and premature fast streaming lead to loss of polarity and infertility (Dahlgaard et al., 2007; Manseau and Schupbach, 1989; Theurkauf, 1994), while persistence of the mesh prevents fast streaming and delays mRNA delivery, decreasing fertility (Bor et al., 2015; Dahlgaard et al., 2007).

A genetic screen first identified *cappuccino* (*capu)* and *spire (spir)* as maternal-effect loci responsible for patterning the anterior-posterior and dorsal-ventral axes of the embryo (Manseau and Schupbach, 1989). These two genes were implicated in regulating the cytoskeleton, as mutations in both *capu* and *spir* resulted in premature or delayed streaming, leading to disruption of *osk, grk,* and *nos* localization (Bor et al.,

2015; Emmons et al., 1995; Manseau et al., 1996; Manseau and Schupbach, 1989; Theurkauf, 1994; Wellington et al., 1999). Capu is part of the FMN family of formin nucleators and Spir is the defining member of a class of actin nucleators commonly referred to as tandem WASP homology 2 (WH2) domain nucleators (Dominguez, 2016; Higgs and Peterson, 2005). They both nucleate actin, but Capu also processively elongates actin filaments. Deeper investigation into the roles of Capu and Spir led to the finding that these two proteins build the actin mesh (Dahlgaard et al., 2007; Quinlan, 2013). Functional interaction between Capu and Spir is observed both *in vitro* and *in vivo* (Bradley et al., 2019; Montaville et al., 2014; Quinlan, 2013; Quinlan et al., 2007; Vizcarra et al., 2011; Zeth et al., 2011). In *Drosophila,* point mutations that prevent Capu/Spir interaction result in failure to build an actin mesh, premature fast streaming, and fertility loss (Quinlan, 2013; Vizcarra et al., 2011). Moreover, during late-oogenesis, Capu and Spir protein levels decrease to less than 10% of those in the whole ovary (Quinlan, 2013). The reduction in protein levels coincides with the disappearance of the actin mesh, suggesting that their activity needs to be regulated for proper mesh formation and removal. An analogous mesh is also found in mouse oocytes, where mammalian homologs of Capu and Spir, Formin-2 (Fmn2) and Spire1/Spire2 respectively, are required to build an actin network for asymmetric spindle positioning (Azoury et al., 2011; Pfender et al., 2011; Schuh, 2011). Thus, the importance of Capu/Spir is evolutionarily conserved, yet there is little known about the factors that regulate these proteins or the actin mesh.

Large-scale proteomic screens are powerful tools for studying protein-protein interactions in a range of biological processes. Conventional methods like co-

immunoprecipitation (co-IP) require stable, high-affinity complexes to survive cell lysis while more current methods like proximity labeling allow detection of transient interactions in a native environment. Combining these complementary methods offers a more complete view of the protein interaction landscape and provides added confidence when novel interactors are enriched in both datasets. With the goal of understanding Capu and Spir as well as actin mesh regulation, we combined co-IP and proximity labeling with quantitative mass spectrometry to identify both transient and stable interactors and build a comprehensive map of the Capu/Spir interactome. We used GFP-Traps for co-immunoprecipitation and the biotin ligase, TurboID, to perform proximity labeling (Baker et al., 2021; Branon et al., 2018). These two approaches validate known Capu and Spir interactors as well as reveal previously unrecognized interactors.

Here, we elucidate the unanticipated, intracellular role of the novel Capu interactor, Semaphorin-2a (Sema2a). Semaphorins and their cognate plexin receptors are known for their role in neural guidance. Indeed, Sema2a has been extensively studied in the central nervous system (CNS) as a secreted signaling protein that binds to its canonical receptor, Plexin-B (PlexB), to mediate axon guidance (Ayoob et al., 2006; Hu et al., 2001; Roh et al., 2016). In fact, the large family of Semaphorin signaling proteins contributes to a range of processes in development (Jongbloets and Pasterkamp, 2014). Notably, Sema2a mRNA is detected in the embryonic gonad, in addition to neurons, suggesting it could play a role in gametogenesis (Kolodkin et al., 1993). Here we describe a role for Sema2a in oogneesis. Although normally secreted, we observe that Sema2a is abundant inside the germarium, germline, and follicle cells

of the ovary. Confirming its importance in oogenesis, loss of Sema2a leads to decreased ovary size, with ovaries often too small to find or possibly non-existent. When the ovaries are visible, egg chambers have not developed past mid-oogenesis. Loss of PlexB results in ovaries that develop normally and are wild-type in size, indicating that Sema2a functions independently of PlexB in oogenesis. Using biochemical assays and genetic analyses, we demonstrate that Sema2a interacts with Capu. In fact, Sema2a inhibits the actin assembly activity of Capu *in vitro*. Consistently, we find that actin mesh density as well as *osk* mRNA localization are sensitive to relative levels of Sema2a and Capu. While *osk* mRNA localization is also altered in PlexB mutants, the phenotypes are distinct. Together, our findings establish a previously uncharacterized, intracellular role for Sema2a in oogenesis that is independent of PlexB and provide new insight into the regulation of the actin cytoskeleton during oogenesis.

Results

The Capu/Spir interactome identified with quantitative mass spectrometry

To identify the interactors of Capu and Spir, we performed co-immunoprecipitation combined with mass spectrometry (co-IP/MS) in ovaries expressing UASp-GFP-CapuA, UASp-CapuA-GFP, or UASp-SpirC-GFP driven by *capu*-GAL4, a "Trojan-GAL4" driver within the *capu* locus and optimized for germline expression (**Figure 2-1A**)(Bailey et al., 2024; Diao et al., 2015). We compared these data to the results of co-IP/MS data from wild-type flies and negative controls lacking the driver. Data-independent acquisition (DIA) mass spectrometry data processed by DIA-NN and analyzed by FragPipe Analyst (FC > 2 and p-value < 0.05) revealed 9 significantly enriched proteins for GFP-tagged Capu and 130 proteins for GFP-tagged Spir, in three biological replicates (**Figures 2-1B-E and Table 1**) (Demichev et al., 2020; Hsiao et al., 2024). As expected, Capu and Spir were both significantly enriched in their respective co-IPs. In order to distinguish potential interactions through actin filaments, we repeated the co-IPs in the presence of the actin depolymerizing agent, Latrunculin A. The same sets of proteins were enriched, indicating that none of the interactions that we report here are solely indirect binding to Capu or Spir through filamentous actin (**Figures 2-S1A-B**). We performed GO analysis using clusterProfiler in R and found that for Spir co-IPs, the top biological processes compared to the background proteome were related to actin and mRNA localization, which are consistent with known functions of Spir (**Figure 2-1G**) (Yu et al., 2012). Interestingly, for Capu co-IPs, the top biological processes were more specifically locomotion- and

axon-related, based on the genes w, Sema2a, Sema2b, and homer (**Figure 2-1F, Table 1**).

In parallel, we performed TurboID-proximity labeling experiments in ovaries expressing UASp-CapuA-GFP or UASp-SpirC-GFP and UASp-GBP-TurboID, driven by matα-GAL4 (**Figure 2-2A**). The data were compared to the UASp-GBP-TurboID controls. Ovaries were stained with an anti-GFP antibody to visualize GFP-tagged Capu and Spir constructs, phalloidin for actin structures, and streptavidin for proteins biotinylated by GBP-TurboID. The colocalization of the GFP-tagged Capu/Spir and biotinylated proteins suggested successful labeling (**Figures 2-S1E-F'''**). However, expression levels of Capu and Spir were relatively low, and streptavidin was detected throughout the egg chamber in experimental and control flies, making the GBP-TurboID negative control essential (**Figures 2-S1C-F'''**). We next purified the biotinylated proteins with streptavidin magnetic beads and identified them by DIA-based mass spectrometry. Capu and Spir were preferentially isolated from their respective TurboID lines, showing that GBP-TurboID was efficiently labeling the GFP-tagged Capu and Spir constructs as well as proximal proteins. We identified 6 components in the Capu-TurboID data set that were similarly significantly co-purifying with the Capu co-IPs and 22 proteins significantly co-purifying in both the Spir-TurboID and Spir co-IPs (**Figures 2-2B-E and Table 2**). Similar to the co-IPs, GO analysis of the TurboID data showed enrichment of locomotion for Capu and actin-related processes for Spir (**Figures 2-2F-G**).

Very few Capu or Spir interactors have been identified to date. Supporting the validity of our assays we detected several of the reported binders. For example, we

identified Myosin V (*didum*), which interacts with Spir in *Drosophila* and mammalian cells (**Figures 2-1C and 2C**) (Ong et al., n.d.; Pylypenko et al., 2016). In the Spir-TurboID dataset specifically, we identified Jun N-terminal kinase (*bsk*), which was previously reported to bind Spir in a yeast two-hybrid assay (**Figure 2-2C**) (Otto et al., 2000). We did not expect to detect Capu in Spir datasets because the SpirC isoform we used as bait lacks the KIND domain that binds to Capu. On the other hand, Spir (endogenous, full length) was significantly enriched in the Capu-TurboID dataset, as expected (**Figure 2-2B**). Consistent with evidence that the Spir/Capu interaction is transient, we did not observe Spir in Capu co-IP datasets (**Figure 2-1B**). Lastly, of the 6 proteins associated with Capu in both co-IP and TurboID datasets, we identified Cut-up (Ctp), which we previously detected with TAP-tagged Capu (**Figures 2-2B, 2D, and Table 2**; TAP data not shown). Taken together, these data not only validate biological relevance of the Capu/Spir interactome in actin-related processes, but they also highlight unexpected links between Capu and multiple neuronal proteins.

We were interested in characterizing Sema2a in greater detail considering the extensive work that has been done establishing Sema2a as vital for axon guidance (Ayoob et al., 2006; Hu et al., 2001; Roh et al., 2016). Semaphorins and more specifically, the Semaphorin-Plexin-Mical signaling pathway, play a role in depolymerizing actin networks in growth cones and other motile cells (Ayoob et al., 2006; Fan et al., 1993; Hung et al., 2010; Kolodkin et al., 1993; Luo et al., 1993; Stedden et al., 2019). We hypothesized that Sema2a might interact with Capu to disassemble the actin mesh during oogenesis but the story was more complex. While Sema2a was significantly enriched in the Capu co-IPs (FC ≈ 64, $p < 1E\text{-}7$), we note

that it was only moderately enriched in the TurboID dataset (FC ≈ 5, p = 0.0514). Its receptor, PlexB, was also present in the TurboID dataset at even lower levels (FC ≈ 3.5, p = 0.173). Differences in co-IP and TurboID datasets are not uncommon, as each method provides overlapping but also distinct sets of protein based on many factors, such as the duration of a given interaction in the cell (Moreira et al., 2023). The presence of Sema2a at high levels in the co-IPs suggest that Sema2a and Capu bind stably. Its lower enrichment levels in the TurboID experiment suggest that Sema2a may not have accessible lysines in the vicinity of Capu or it may be part of a larger Capu-binding complex but not close enough in proximity to be efficiently labeled.

Sema2a plays an intracellular role in oogenesis

To test whether Sema2a plays a role in oogenesis, we generated presumptive Sema2a-nulls by crossing the loss-of-function allele *sema2a*^{03021} to a deficiency line (Df(2R)B65) *(sema2a*^{03021}*/sema2aDf)*. After eclosion of *sema2a*^{03021}*/sema2aDf* mutants, we observed decreased viability, with an average of ~50% of flies (N=95 total in 7 replicates) dying upon CO_2 anesthetization (**Figure 2-3A**). An earlier study reported that Sema2a-nulls only survive for 2 days (Kolodkin et al., 1993). We reasoned that the added stress of CO_2 caused earlier lethality. Very brief CO_2 exposure resulted in slightly increased viability. Among the flies that survived (n=65 total), around 36% had relatively normal-sized ovaries after overnight fattening with yeast paste. The remaining 64% had small ovaries, if they could be found at all (**Figures 2-3B,C**). Despite being fattened, these small ovaries did not contain egg chambers that matured beyond mid-oogenesis, showing the importance of Sema2a in

oogenesis (**Figure 2-3C**). The ovaries of flies that did not survive CO_2 exposure had no observable ovaries but could not be directly compared because they could not be fattened. In contrast, *sema2a*^{03021}*/+* and *sema2aDf/+* heterozygotes appeared wild-type, with no loss of viability or diminished ovary-size (**Figure 2-3C**).

Because Sema2a acts in axon guidance as a secreted protein, we asked whether it localizes within the egg chamber. We stained ovaries with an antibody against Sema2a that had been validated in motor axons (**Figure 2-3D**) (Winberg et al., 1998). To confirm the specificity of the Sema2a antibody in the egg chamber, we stained *sema2a*^{03021}*/sema2aDf* mutants and found vastly reduced staining compared to the abundant signal in the oocyte and follicle cells of wild-type egg chambers (**Figures 2-3E and S2A**). Importantly, Sema2a was highly expressed throughout the ovariole. We detected it in the early germarium, consistent with reports with a GFP-trapped Sema2a (**Figure 2-3D**) (Hsu and Drummond-Barbosa, 2017). It also filled early egg chambers, both somatic follicle cells and the germline cyst. By stage 3, Sema2a was enriched in the oocyte compared to the nurse cells. High levels of Sema2a were seen primarily in the oocyte and follicle cells during early and mid-oogenesis. By stage 9, however, Sema2a levels in the oocyte decreased. We detected little to no Sema2a in stage 11 germline cells, though protein remained in the follicle cells (**Figure 2-3D**).

We questioned how it is possible that Sema2a localizes at such high levels in the oocyte and follicle cells, given that Sema2a is known to be secreted in the CNS (Bates and Whitington, 2007; Kolodkin et al., 1993; Wu et al., 2011). Upon examination of the Sema2a gene structure on FlyBase (Gramates et al., 2022; Öztürk-Çolak et al.,

2024), we found that while Sema2a splice variants A, B, and E have a signal peptide sequence, Sema2a variant C has a distinct N-terminal extension lacking this sequence. Thus, we hypothesized that Sema2a-C was the intracellular variant we were observing. To determine which splice variant(s) were expressed in the egg chamber, we performed reverse transcription polymerase chain reaction (RT-PCR) on RNA extracted from w^{1118} (wild-type) ovaries. We reverse transcribed Sema2a mRNA, performed first strand cDNA synthesis, and amplified the N-terminal region specific to the Sema2a isoforms. We first confirmed the presence of Sema2a by amplifying a region present in all isoforms, as indicated by the band at ~900 bp (**Figure 2-3F**). We were unable to detect Sema2a isoform C with multiple primer pairs (**Figure 2-3F**). Nor were we able to detect Sema2a isoform E (data not shown). Because the Sema2a isoform B sequence is entirely contained within isoform A, its presence cannot be confirmed or ruled out. However, isoform A can be uniquely identified due to a short, unique sequence not present in isoform B. Sema2a isoform A expression was abundant, based on the prominent band at ~800 bp (**Figure 2-3F**). Sequencing the amplified product corroborated that it was the sequence specific to isoform A (**Figure 2-S2B).** We conclude that Sema2a isoform A and not isoform C is present in the egg chamber despite the fact that this splice variant contains the signal peptide sequence that directs it to be secreted (**Figure 2-3F**).

Sema2a interacts with Capu during oogenesis

The Capu co-IP and TurboID data suggested that Sema2a could be directly binding to Capu or part of a complex. To compare the subcellular localizations of

Sema2a and Capu, we performed immunofluorescence experiments on ovaries expressing Capu-mScarlet-OLLAS, under control of the endogenous gene (Bailey et al., 2024). These ovaries were stained with antibodies against Sema2a and OLLAS. Consistent with previous studies, Capu localized to the follicle cells, the oocyte, and nurse cells, with enrichment at the cortex of nurse cells (**Figures 2-4A',B',C'**) (Bailey et al., 2024; Bor et al., 2015). In stage 8 and younger egg chambers, the Sema2a and Capu signals colocalize in the oocyte and more specifically at the posterior (**Figures 2-4A-A''**). Like Sema2a, Capu levels in the oocyte decreased during stage 9 and their localization overlaps in the follicle cells (**Figures 2-4B-B''**). Capu and Sema2a were also present in the migrating border cells, a cluster of 6-10 follicle cells that are necessary for the formation of the eggshell (Figure S2C, boxed in yellow) (Montell et al., 1992). By stage 11, Capu remained at the nurse cell cortex but like Sema2a, it was undetectable in the oocyte (**Figure 2-4C-C''**). Thus, Sema2a and Capu localizations overlap in the oocyte as well as in the follicle cells, and their expression levels follow similar temporal patterns.

We further examined the localization patterns of Sema2a and Capu by analyzing intensity profiles from the anterior to the posterior of the oocyte and through the follicle cells (**Figures 2-4D-F**, yellow arrows). In stage 8 egg chambers, Sema2a and Capu filled the oocyte but the highest levels of the two were near the posterior of the oocyte and in the follicle cells (**Figure 2-4D**). In stage 9, Sema2a and Capu were most concentrated in follicle cells with the highest intensity and overlap starting at approximately the oocyte/follicle cell interface (**Figure 2-4E**). By stage 11, Sema2a

and Capu were still present but not concentrated in a specific area in the follicle cells (**Figure 2-4F**).

Given that *spir*- and *capu*-null egg chambers completely lack a mesh, we examined the mesh in a Sema2a-null background. In wild-type oocytes, the mesh is present during mid-oogenesis from stages 6-10A and disappears during stage 10B. We measured mesh density by staining egg chambers with phalloidin and collected data from stage 7 and stage 9 egg chambers (**Figure 2-5**) (Dahlgaard et al., 2007; Quinlan, 2013). In each sample, we included egg chambers expressing histone-GFP, which served as a wild-type internal control to compensate for staining variability (Bor et al., 2015). In *sema2a*^{03021}*/sema2aDf* oocytes, the mesh was not different from wild-type at stage 7 (**Figures 2-5A and M**; all statistics are given in figure legends). In contrast, mesh density decreased significantly by stage 9 (**Figures 2-5B and M**). We noted that the standard deviation at stage 7 was almost twice that at stage 9, and there seemed to be a bimodal distribution. When analyzed as two groups, one set displayed a decrease in mesh density comparable to the stage 9 level and the other, an increase in mesh density that differed significantly from each other. In fact, the mesh was difficult to detect in multiple independent runs, suggesting that it is often less dense. We note that the eggs examined were potentially biased by the issues of viability loss in Sema2a-null flies. Furthermore, a fraction of *sema2a*^{03021}*/sema2aDf* mutants have normal-sized ovaries and may have other differences compared to the smaller ovaries. Data were collected from both ovary types but later stages usually had to be acquired from the larger ovaries.

We confirmed a genetic interaction between Sema2a and Capu by crossing Sema2a (*sema2a^{03021}*) and Capu (*capu^{HK3}*) loss-of-function alleles to generate *sema2a^{03021}/capu^{HK3}* trans-heterozygotes. Viability and ovary size were not detectably affected in either the Capu heterozygote (*capu^{HK3}/+*) or the trans-heterozygote (*sema2a^{03021}/capu^{HK3}*). However, examination of the actin mesh provided evidence of the genetic interaction. At stage 9, in both *sema2a^{0302}/+* and *capu^{HK3}/+* oocytes, the meshes were significantly denser than wild-type (**Figures 2-5E,H,O**). Interestingly, the mesh density in the stage 9 *sema2a^{03021}/capu^{HK3}* trans-heterozygote recovered; it was not different from wild-type, consistent with a dosage compensation effect (Figures 5K,O). Furthermore, both *sema2a^{03021}/+* and *capu^{HK3}/+* significantly differ from *sema2a^{03021}/capu^{HK3}* (**Figure 2-5O**). The same trend was apparent at stage 7 except that the increase in mesh density for *capu^{HK3}/+* was less dramatic and less statistically significant (**Fig 2-5D,G,J,N**). As is the case for wild-type, no mesh was detected in stage 11 oocytes of any of the experimental genotypes (**Figures 2-5C,F,I,L**). The presence of the mesh during mid-oogenesis and its absence during late-oogenesis implies that there is a proper transition from slow to fast streaming in these genotypes. Together, the data suggest that Sema2a and Capu protein levels are important for mutual regulation and mesh assembly.

Sema2a inhibits Capu in vitro

To determine whether Sema2a regulates Capu's actin assembly activity, we tested purified recombinant proteins in a pyrene-actin polymerization assay. The C-terminal half of Capu, (Capu-CT, amino acids 467-1059) contains the proline-rich

formin homology 1 (FH1), the well-conserved FH2, and the tail domains (Higgs and Peterson, 2005; Pruyne, 2016; Vizcarra et al., 2011). We found that Sema2a inhibited Capu-mediated actin assembly in a dose-dependent manner (4 μM actin, **Figure 2-6A**; 2 μM actin, **Figure 2-S2D**). Sema2a alone had no effect on actin assembly, demonstrating that the inhibition is due to interaction between Sema2a and Capu-CT (**Figure 2-6A**).

Next, we performed a similar assay in the presence of profilin, which is known to strongly inhibit Capu-CT's nucleation activity while it accelerates elongation (Bor et al., 2012; Yoo et al., 2015). Sema2a again inhibited Capu-CT–mediated actin polymerization in a dose-dependent manner (**Figure 2-6B**). It had no impact on profilin-actin assembly.

Capu is autoinhibited by an interaction between the N-terminal Capu Inhibitory domain (CID) and the Capu-tail, C-terminal to the FH2 domain (Bor et al., 2012). We asked whether Sema2a influenced this interaction. The N-terminal half of Capu (Capu-NT, amino acids 1-466), which contains the CID, has no effect on actin assembly on its own, as we have previously reported (**Figure 2-6C**) (Bor et al., 2012). Addition of 200 nM Capu-NT reduces actin assembly in the presence of 20 nM Capu-CT to just above the baseline actin alone rate (**Figure 2-6C**). We observed no difference when Sema2a was added to this combination (**Figure 2-6C**). The same was true when profilin was present (**Figure 2-6D**). However, addition of Sema2a in the presence of a lower concentration (50 nM instead of 200 nM) of Capu-NT reduces Capu-CT-mediated actin assembly more than Capu-NT (**Figure 2-S2E**). We interpret this as evidence that Capu-NT competes with Sema2a binding to Capu-CT.

Overall, these data demonstrate that Sema2a regulates Capu-CT-mediated actin nucleation directly, whether profilin is present or not. Consistent with these *in vitro* studies, the mesh density is increased in *sema2a*^{03021}/+ oocytes, compared to wild-type controls and *sema2a*^{03021}/*capu*^{HK3}. Together, these data suggest that lower levels of Sema2a permit higher levels of Capu activity in the oocyte (**Figures 2-5N and O**).

Sema2a mutants disrupt osk mRNA localization

Additional evidence of interaction between Sema2a and Capu comes from examining *osk* mRNA localization in mid-oogenesis. Proper localization of polarity determinants is necessary to establish the major body axes of the oocyte and future embryo. Localization of some of these polarity determinants depends on the presence of the actin mesh during mid-oogenesis. One such component is *osk* mRNA, which is distributed throughout the ooplasm during stages 1-7 and is then directed to and enriched at the posterior pole of the oocyte from stage 8 onward (Kim-Ha et al., 1991). Other polarity factors that are localized during mid-oogenesis include *bcd* and *grk*, which localize to the anterior and anterodorsal poles of the oocyte, respectively (Thio et al., 2000; Trovisco et al., 2016). We examined the localization patterns of these mRNAs in mutant backgrounds of stages 7 and 8 oocytes. *sema2a*^{03021}/*sema2aDf* mutants showed normal localization of *bcd* and *grk,* comparable to that of wild-type (*w*^{1118}) at all stages (**Figures 2-S3A-H'**). In contrast, there was major disruption of *osk* mRNA in *sema2a*^{03021}/*sema2aDf* oocytes, evidenced by clumps or foci as opposed to the more diffuse distribution of *osk* mRNA in wild-type and *capu*^{HK3}/+

oocytes (**Figures 2-7A-A'', D-D'', G-G'', J-J'', M-M''**). While a fraction of *sema2a*^{03021}/+ oocytes (40%, n=25) showed clumping of *osk* mRNA, the phenotype was highly penetrant in *sema2a*^{03021}/*capu*^{HK3} (100%, n=14) and *sema2a*^{03021}/*sema2aDf* egg chambers (97% n=31) (**Figure 2-7P**). This coalescence of clumps was detectable as early as stage 3 (**Figures 2-S3I-I''**). We observed comparable abnormal foci of Staufen (Stau) in *sema2a*^{03021}/*sema2aDf* mutants and *sema2a*^{03021}/*capu*^{HK3} trans-heterozygotes, consistent with Stau's role in *osk* mRNA transport (**Figures 2-6C,F,I,L,O**) (Micklem et al., 2000). There was no evidence of premature Osk translation (**Figures 2-7B,E,H,K**) (Besse et al., 2009; Kim-Ha et al., 1995). By stage 9, there was some evidence of residual mRNP aggregation in *sema2a*^{03021}/*capu*^{HK3} oocytes, but the majority of *osk* mRNA and Stau were at the posterior pole, and Oskar translation appeared wild-type (**Figures 2-S4A-O**).

Similar clumps of *osk* mRNA are not observed in *spir*- or *capu*-nulls. Instead, *osk* mRNA appears scattered and fails to localize to the posterior pole at stage 9, presumably due to absence of the mesh and presence of premature fast streaming (Dahlgaard et al., 2007; Manseau and Schupbach, 1989; Theurkauf, 1994; Wellington et al., 1999). Given that *osk* mRNA clumps are present in *sema2a*^{03021}/*capu*^{HK3} at stage 7 but mesh density is indistinguishable from wild-type in the trans-heterozygote, the mislocalization of *osk* is unlikely to be a direct result of altered mesh. Instead, the difference in phenotypes suggests that Sema2a and Capu play more than one role, directly or indirectly, in mRNA localization.

Sema2a and its canonical receptor PlexB have different phenotypes

Because the major Sema2a isoform identified was the canonical isoform A that has been extensively studied in the CNS, we chose to also examine its interacting partner, PlexB (Ayoob et al., 2006). Recall that PlexB was present in the Capu-TurboID dataset but not at significant levels (FC ≈ 3.5, p = 0.173). We tried to generate PlexB-nulls using the loss-of-function allele *plexB*^{KG00878}. However, we did not recover any homozygous *plexB*^{KG00878} flies (Ayoob et al. 2006 recovered ~6% escapers). Instead, when we crossed *plexB*^{KG00878} to a deficiency line (Df(4)M101-62f) (*plexB*^{KG00878}*/plexB-Df)*, we recovered 5 or fewer escapers from each cross (Ayoob et al., 2006 recovered none). The *plexB*^{KG00878}*/plexB-Df* mutants all survived CO_2 exposure, with viability and ovary size resembling that of wild-type, unlike *sema2a*^{03021}*/sema2aDf* mutants. In assessing the *osk* mRNA localization in stage 7, we found that *plexB*^{KG00878}*/+* heterozygotes had multiple phenotypes – 50% with diffuse mRNA localization similar to wild-type, 39% with clumpy spots similar to *sema2a*^{03021}*/sema2aDf,* and 11% (n=36) with a distinct single spot in the center of the oocyte (**Figures 2-8A-A'', P**). The coalescence of one single spot of *osk* is comparable to the phenotypes seen in stage 9 Par-1 and *didum* mutants among others (Doerflinger et al., 2006; Krauss et al., 2009). These proportions shifted in *plexB*^{KG00878}*/plexB-Df* egg chambers, such that only 5% had apparently normal mRNA localization, 28% had clumpy spots, and the majority, 67%, contained a single cluster of *osk* mRNA in the center of the oocyte (n=18) (**Figure 2-8D-D'', P**). As expected, the Stau distribution in *plexB*^{KG00878}*/plexB-Df* oocytes tracked that of *osk* mRNA in the same background (**Figure 2-8F**). However, *plexB*^{KG00878}*/+* heterozygotes predominantly contained Stau foci, inconsistent with the majority of *osk* mRNA localization being wild-type and more comparable to that of

sema2a^{03021}*/sema2aDf* (**Figure 2-8C**). By stage 9 *osk* mRNA and Stau were concentrated at the posterior pole, and Oskar translation appeared wild-type, in both *plexB*^{KG00878}*/+* and *plexB*^{KG00878}*/plexB-Df* oocytes (**Figures 2-S5A-F**).

To test for a role that PlexB might play in the Sema2a/Capu pathway, we crossed *plexB*^{KG00878} to *sema2a*^{03021} or *capu*^{HK3} to generate trans-heterozygotes. We also drove expression of PlexB lacking the Sema2a binding domain (UASt-PlexBΔSema2a) using the matα-GAL4 driver. We frequently observed one central concentration of *osk* mRNA in stage 7 *capu*^{HK3}*/+;;plexB*^{KG00878}*/+* (55%, n=47), UASt-PlexBΔSema2a (50%, n=14), and *sema2a*^{03021}*/+;;plexB*^{KG00878}*/+* oocytes (35%, n=17) (**Figures 2-8G-G'', J-J'', M-M'', P**). We note that *sema2a*^{03021}*/+;; plexB*^{KG00878}*/+* oocytes had 41% clumpy spots, consistent with some overlap in the pathways they influence. Of the 11% that contained more concentrated spots in *capu*^{HK3}*/+;;plexB*^{KG00878}*/+*oocytes, the *osk* mRNA distributions seemed to capture transient images of mRNA being moved toward to the posterior pole, akin to multiple transport defects (**Figures 2-S5P-P''**). In all of these backgrounds, the Stau distribution tracked the *osk* mRNA (**Figures 2-8I, L, O**) and there was no evidence of premature or ectopic Osk protein translation (**Figures 2-8B,E,H,K,N**). Once again, by stage 9, *osk* mRNA, Osk protein, and Stau were all properly localized to the posterior pole of the oocyte in these different *plexB* mutant backgrounds (**Figures 2-S5A-O**). The altered *osk* mRNA localization patterns suggest that Sema2a and PlexB both operate in the *osk* transport pathway. The predominance of centralized *osk* mRNA rather than clumps and the wild-type ovary size in *plexB* mutant backgrounds suggest that Sema2a plays a role that is independent of PlexB in oogenesis.

Discussion

Defining the Spir/Capu interactome using complementary proteomic approaches

Combining both co-immunoprecipitation and TurboID-proximity labeling enables us to capture both transient and stable interactions, potentially offering a wide range of spatial and temporal information. We discovered proteins that were consistent with previous studies, such as Myosin V in both Spir co-IPs and TurboID datasets, suggesting that it is a stable and spatially close interaction (**Figure 2-1B', 2B, Table 1, Table 2**). On the other hand, Spir was not enriched in Capu co-IPs but was enriched in Capu-TurboID datasets, indicating that it is spatially close but perhaps too weak or transient of an interaction to be detected in co-IPs (**Figure 2-1C, 2C, Table 1, Table 2**). This notion fits with protein localization studies and a model of Spir/Capu interaction, whereby Spir and Capu coordinate to nucleate actin, then releasing Capu to elongate the filaments independently (Bailey et al., 2024; Bradley et al., 2019; Quinlan, 2013). We note again that Capu was not expected in either Spir co-IP or Spir TurboID datasets because the SpirC isoform does not contain the KIND domain that binds to Capu.

It was intriguing to find that multiple neuronal-related proteins were enriched in Capu co-IPs, such as Sema2a, Sema2b, and homer. In fact, homologs of Capu, Fmn2 in mammals and Fmn2b in zebrafish, play roles in neurons (Almuqbil et al., 2013; Kundu et al., 2020; Nagar et al., 2021). Other parallels between the central nervous system and reproductive system have been reported. For example, Vap33 (VAMP-associated protein) is an essential gene critical to synaptic homeostasis (Kamiyama et al., 2025). It was also identified in Egl-TurboID datasets from ovaries as well as shown

to be enriched in oocytes and transported in a Egl/Dynein-dependent manner (Baker et al., 2021). In addition, several proteins critical for transport and post-transcriptional regulation of mRNAs in the ovary, such as Nanos and Pumilio, play important roles in dendrite morphogenesis (Ye et al., 2004).

We performed secondary screens on a number of proteins enriched in the co-IP and TurboID datasets. While not yet independently validated, we expect that proteins found highly enriched in both co-IPs and TurboID are likely to be bona fide interactors. Preliminary data suggest that several will provide new opportunities for understanding Spir-Capu regulation and mesh dynamics.

Sema2a plays a role in Drosophila oogenesis

We report here a previously unidentified role for Sema2a in the female reproductive system. What is most unusual is the intracellular localization of the protein. TurboID detection, immunofluorescence, and stage-specific changes in enrichment argue strongly that Sema2a is acting within the oocyte. Another semaphorin, Sema5c is known to operate in the follicle cells of the developing egg chamber (Stedden et al., 2019). In contrast to Sema2a, Sema5c acts through its canonical signaling pathway with PlexA. The protein is planar-polarized and reduces “backwards” motility, coordinating essential epithelial migration. Sema5c functions as a transmembrane protein. It is also detected intracellularly in a sparse and punctate pattern, consistent with endosomes and regulation of transmembrane protein signaling.

Interestingly, human semaphorins, including the ortholog of Sema2a, SEMA3A, play multiple roles in female fertility (Emery et al., 2023; Giacobini, 2015; Zhang et al., 2025). In fact, SEMA3A levels increase in the plasma of women with depleted ovary reserves. Thus, SEMA3A may be an effective biomarker for diagnosis and treatment (Palese et al., 2024). To date, the known ovarian roles of semaphorins are classical signaling roles, with the help of plexin and neuropilin receptors. They influence follicle development and ovulation, both remotely through the gonadotropin hormone system and by locally influencing cell motility and remodeling (Messina and Giacobini, 2013; Zhang et al., 2025).

Drosophila Sema2a is clearly critical to oogenesis. Absence of Sema2a has a strong impact on ovary development, resulting in a majority of ovaries that are considerably smaller than wild-type, even not detected at times (**Figure 2-3B-C**). Development appears to stall during early to mid-oogenesis in these small ovaries. The presence of normal-sized ovaries that proceed to later stages in the Sema2a-nulls suggests that the ovary may compensate for the loss of Sema2a to some degree, which could contribute to the complexity we observe in mesh density data.

Inhibition of Capu-mediated actin assembly is consistent with some of the mesh phenotypes we observed. Higher mesh intensity correlated with decreased levels of functional Sema2a in *sema2a*^{03021}/+ oocytes. In addition, in the *sema2a*^{03021}/*capu*^{HK3} trans-heterozygote mutants, the mesh density is similar to that of wild-type, suggesting that relative amounts of these two proteins are important for function. However, the mesh in the Sema2a-null was usually less dense than wild-type. Perhaps, alternate regulatory pathways overcompensate in the absence of Sema2a.

The CID and Spir-KIND both inhibit Capu by binding to the Capu-tail. Based on the lack of an effect when Sema2a was added to Capu-CT plus Capu-NT, we speculate that Sema2a binds in the same region. However, Sema2a is not a particularly potent Capu-inhibitor. The K_i is hundreds of nanomolar, whereas K_i's for Capu-NT and the Spir-KIND domain are ~10 nM (Bor et al., 2012; Vizcarra et al., 2011). The fact that we identified Sema2a in Capu co-IPs, suggests that the *in vivo* interaction is fairly stable. Together, these data suggest that the stability of the interaction may depend on a complex of proteins. Notably, Sema2a functions as a dimer and can heterodimerize with Sema2b, which was also enriched in the Capu interactome.

Previous investigations showed no correlation between mesh density and streaming velocities beyond the all or nothing impact of the *capu*-null (Bor et al., 2015; Emmons et al., 1995; Yoo et al., 2015). Furthermore, egg chambers that lack a mesh continue to develop well past mid-oogenesis. Together, these data lead us to conclude that mesh density is not the critical factor impacting development when it fails in Sema2a mutants during mid-oogenesis. The fact that a strong *osk* mRNA phenotype in the same $sema2a^{03021}/capu^{HK3}$ transheterozygote that rescues the mesh phenotype indicates that at least two pathways are mediated by Sema2a-Capu interaction.

osk mRNA localization

The mechanisms controlling *osk* mRNA are dependent on the interplay of many different and complex processes, including the cooperation of the cytoskeleton, molecular motors, and repression/activation factors that contribute to proper

localization of *osk* mRNA and its spatiotemporally controlled translation (Lasko, 2012; Lehmann, 2016). During stages 7 and 8, microtubules are oriented with plus-ends biased toward the posterior of the oocyte, enabling the plus-end directed motor, kinesin, to transport *osk* mRNA across the oocyte (Brendza et al., 2000; Parton et al., 2011; Zimyanin et al., 2008). During this time, *osk* mRNA is silenced by Bruno1 and other proteins to prevent ectopic translation of Osk protein (Besse et al., 2009; Kim-Ha et al., 1995; Mhlanga et al., 2009). By stages 9-10, Bruno1 repression is lifted and Makorin1 is able to stabilize and anchor Osk (Dold et al., 2020).

The consequences of *osk* mislocalization specifically during stage 7 and earlier are unknown and need to be further investigated. The clumps of concentrated *osk* mRNA that are formed in *sema2a*^{03021}*/capu*^{HK3} and *sema2a*^{03021}*/sema2aDf* mutants are similar to those detected in PTB (polypyrimidine tract-binding protein) mutants (**Figure 2-7**) (Besse et al., 2009). PTB is part of the ribonucleoprotein complex required for *osk* mRNA transport, which contributes to translation suppression. Consistently, premature Osk protein colocalizes with the abnormal *osk* mRNA punctae in the PTB-mutant oocyte. The fact that Osk protein does not appear ectopically in Sema2a mutants in stages 8 and earlier and properly translates during stage 9 and later suggests that the Bruno1 and Makorin1 pathway is functioning.

The accumulation of *osk* mRNA foci rather than the typical diffuse distribution throughout the oocyte could be due to a cytoskeletal malfunction. Dosage compensation in *sema2a*^{03021}*/capu*^{HK3} transheterozygotes that results in wild-type actin mesh density during stage 7 oocytes is in direct contrast with the severe *osk* mRNA phenotype observed at this stage. This observation suggests that *osk* mRNA

mislocalization is not a consequence of an altered actin mesh. The fact that *bcd* and *grk* are properly localized at the anterior suggests that microtubules and their motors are not entirely dysfunctional. However, bcd and grk are localized at the pointed ends of microtubules, which may be normally distributed even when the plus ends are not.

We found one other report of aggregated *osk* mRNA that was corrected by stage 9. Snee and MacDonald (Snee and Macdonald, 2009) found that sponge bodies can be organized along a spectrum from a diffuse distribution to a more clumpy, reticulated structure. They found that virgin females and flies that are not fed extra yeast, in addition to the typically rich food they grow on, were more likely to have reticulated sponge bodies. In contrast, 3-5 day old females fed a normal diet supplemented with dry yeast had consistently diffuse small sponge bodies. In the initial report, *osk* mRNA and Stau localized to the clumps but not consistently. Based on FRAP data and the fact that *osk* mRNA and Stau were properly concentrated at the oocyte posterior by stage 9, it was concluded that the interaction between RNPs and the sponge body are transient as opposed to structural or functional. Our experiments were performed under conditions that favor diffuse sponge bodies. Perhaps Sema2a and Capu play a role in sponge body organization, resulting in clumps in these mutants.

Conclusion

The discovery of interaction between Capu and Sema2a is an excellent example of the power of unbiased proteomics approaches. Neither would be on a list of predicted interactors with the other, based on their known roles and localizations,

i.e. intracellular vs. secreted. Nevertheless, the genetic, cell biological, and biochemical data strongly support the proteomics data. Notably, Sema2b was also enriched in our proteomics datasets. Sema2a functions as a dimer and can heterodimerize with Sema2b (Rozbesky et al., 2019). In fact, there is evidence of significant crosstalk between the Sema2 proteins and the Plexin receptors (Winberg et al., 1998; Wu et al., 2011). It remains to be seen if Sema2b functions with Sema2a in oogenesis. It will be important to determine if Sema2b upregulation is responsible for compensation in the Sema2a-null background. It is curious that Sema2a's canonical receptor PlexB also function in a pathway that temporarily alters *osk* localization when disrupted yet gives a distinct phenotype at the whole animal level, the ovary level, and in the specific mRNA mislocalization. Many exciting questions remain, including how Sema2a is retained intracellularly, whether it plays additional intracellular roles, and how the transient mislocalization of *osk* affects other processes in oocyte progression, embryogenesis, and overall fertility.

Methods

Drosophila stocks

The following fly lines were obtained from Bloomington Drosophila Stock Center: w^{1118}, Sema2a^{03021}/SM5 (RRID:BDSC_11257, (Kolodkin et al., 1993)), Df(2R)B65/CyO (RRID:BDSC_65746, (Wu et al., 2011)), PlexB^{KG00878}/ciD (RRID:BDSC_14579 (Bellen et al., 2004)), PlexB-Df(4)M101-62f/eyD (RRID:BDSC_9433), UASp-SpirC-GFP (RRID:BDSC_24765 (Rosales-Nieves et al., 2006)), His2AV-EGFP/SM6A (RRID:BDSC_24163). UASp-CapuA-GFP, UASp-GFP-CapuA, Capu-mScarlet-OLLAS,and capu-GAL4 were constructed in the Quinlan lab and reported in earlier publications (Bailey et al., 2024; Quinlan, 2013). *capu*^{HK3} was provided by the Schupbach lab (Manseau and Schupbach, 1989) and UASp-GBP-TurboID, matα-GAL4 was built and generously provided by the Gonsalvez lab (Baker et al., 2021).

Co-immunoprecipitation

Flies expressing UASp-CapuA-GFP/capu-GAL4 or UASp-SpirC-GFP/capu-GAL4 were fattened with yeast paste overnight at 25°C. 40-100 pairs of ovaries were dissected in 1X PBS and homogenized in lysis buffer (50 mM Tris-HCl pH 7.5, 150 mM NaCl, 1 mM EDTA, 1% Nonidet P40 Substitute, protease inhibitor cocktail). The homogenized samples were sonicated at 40% amplitude with 1 second pulses for 30 seconds. Lysates were spun down and the resulting supernatants were incubated with 25 μL of equilibrated GFP-Trap magnetic agarose (ChromoTek) bead slurry for an hour at 4°C. For experiments with Latrunculin A, 10 μM was added. After an hour, unbound proteins were removed with wash buffer (50 mM Tris-HCl pH 7.5, 150 mM NaCl, 0.5

mM EDTA, 0.05% Nonidet P40 Substitute, protease inhibitor cocktail). Bound proteins were eluted with 200 mM glycine pH 2.5 and immediately neutralized with 1 M Tris-Cl pH 10.4. Eluted proteins were either run on a gel and analyzed by Western blot or prepped for mass spectrometry. Proteomics experiments were analyzed in triplicate from three biologically independent runs.

Mass spectrometry

The eluted proteins were reduced with 5 mM Tris (2-Carboxyethyl) phosphine (TCEP) and alkylated with iodoacetamide (IAA) at RT for 30 min in the dark. SP3 protein clean-up was performed using carboxylate-modified magnetic beads at a ratio of 10:1 (w/w) beads to protein (Hughes et al., 2019). Protein binding was facilitated using ethanol (EtOH) to a final concentration of 50% and washed 3 times with 80% EtOH. Bound beads were then resuspended in 2 M urea and 100 mM Tris-HCl pH 7.5 and digested with 1:100 (w/w) LysC and 1:25 (w/w) trypsin overnight at 37°C, mixing at 1200 rpm. The next day, peptide binding was facilitated using 100% acetonitrile (ACN) and washed 3 times with 100% ACN. Peptides were eluted with 2% dimethyl sulfoxide (DMSO) at 37°C for 30 min. The eluate was collected, dried, and resuspended in 5% trifluoroacetic acid (TFA) for LC-MS/MS analysis.

Samples were analyzed with data-independent acquisition (DIA)-based quantitative proteomics using an UHPLC system coupled to an Orbitrap Astral mass spectrometer. Peptides were loaded onto a Pepsep C18 reverse-phase column (15 cm x 150 µm) at 52ºC and electrosprayed into an Orbitrap Astral mass spectrometer. Peptide separation was performed using the Vanquish Neo UHPLC system, with mobile phase

A and B consisting of 0.1% formic acid (FA) in water and 0.1% FA in ACN, respectively. A 15-minute gradient was used as follows: mobile phase B was increased to 5% from 0-1 min, 5-15% from 1-5 min, 15-25% from 5-12.6 min, 25-38% from 12.6-13.6 min, 38-80% from 13.6-13.7 min, and remained at 80% from 13.7-15 min. DIA spectra were acquired in positive ion mode with MS1 parameters as follows: resolution of 240,000, m/z range of 380-980, normalized AGC target of 500%, and maximum injection time of 3 ms. MS2 spectra were collected at 80,000 resolution, HCD energy of 25%, normalized AGC target of 500%, and maximum injection time of 7 ms. Thermo RAW files were processed using DIA-NN with peptide lengths set to 7-30 and maximum number of missed cleavages as 2. An *in silico* spectral library was generated from the *Drosophila melanogaster* reference proteome.

Proximity labeling

Flies expressing UASp-GBP-TurboID, matα-GAL4/UASp-CapuA-GFP or UASp-GBP-TurboID, matα-GAL4/UASp-SpirC-GFP were fattened with yeast paste overnight at 25°C. 50 pairs of ovaries were dissected in 1X PBS and homogenized in lysis buffer (50 mM Tris-HCl pH 7.5, 150 mM NaCl, 1 mM EDTA, 1% Nonidet P40 Substitute, protease inhibitor cocktail). Homogenized samples were sonicated at 40% amplitude with 1 second pulses for 30 seconds. Lysates were spun down and the resulting supernatant was incubated with 10 μL of equilibrated streptavidin magnetic bead (ThermoFisher) slurry for two hours at 4°C. Unbound proteins were washed 3x with lysis buffer, 3x with 1% SDS, 3x lysis buffer, 3x high salt lysis buffer, 3x lysis buffer, and 4x with PBS (Baker et al., 2021). After extensive washes, proteins were reduced,

alkylated, and digested on beads overnight at 37°C, mixing at 1200 rpm. The next day, SP3 clean-up was performed starting from the ACN step. Proteomics experiments were analyzed in triplicate.

Antibodies

The following antibodies were used: chicken anti-GFP (Aves Labs Inc.; 1:1000), mouse anti-Sema2a (Developmental Studies Hybridoma, 1:20), rat anti-OLLAS (Novus Biologicals; 1:2500), rabbit anti-Osk (gift from Ephrussi lab; 1:3000), mouse anti-Stau (gift from Doe lab, 1:50). The following secondary antibodies from Jackson Immunologicals were all used at 1:200: donkey anti-chicken AlexaFluor488, donkey anti-mouse AlexaFluor647, donkey anti-rat AlexaFluor488, donkey anti-rabbit AlexaFluor488. Samples were counterstained with rhodamine phalloidin (1:600), AlexaFluor647 phalloidin (1:600), or streptavidin AlexFluor647 (1:5000) (Molecular Probes).

Immunofluorescence

Flies were fattened with yeast paste overnight at 25°C. Samples were fixed using previously published protocols (Bailey et al., 2024; Cooley et al., 1992; Ong et al., n.d.). Briefly, ovaries were dissected in cold 1X PBS and fixed in 5% PFA, 16% 1X PBS, and hexane. After 10 minutes of fixation, ovaries were washed 3 times with PBST (1X PBS, 0.1% Triton X-100, 0.5% BSA). Ovaries were then stained with primary antibodies overnight at 4°C. The next day, ovaries were washed with PBST 3 times. The appropriate secondary antibodies were added for 2 hours at room temperature

and then ovaries were washed again 3 times with PBST. Ovaries were mounted in ProLong Gold and imaged the next day. Quantification of colocalization was performed using Fiji. Each channel of the image was normalized and a segment of interest was drawn (width: 5 and size: 10). Plot profile was used to generate a graph of intensity vs. distance (of the drawn segment).

Actin mesh staining

Samples were fixed using previously published protocols (Dahlgaard et al., 2007; Quinlan, 2013). Briefly, ovaries were dissected in 10% PFA in 1X PBS. Ovaries were washed 4 times with PBST and stained with 1 µM phalloidin for no longer than half an hour. Ovaries were washed again 4 times and mounted in ProLong Gold for imaging the next day. Quantification of the density of the actin mesh was performed using Fiji. The mean intensity of each oocyte was compared to the mean intensity of histone-GFP expressing ovaries stained in the same tube to calculate the fold-change of each fly construct (e.g. $sema2a^{03021}/capu^{HK3}$ mean intensity/histone-GFP mean intensity). Data were presented using SuperPlotsOfData (Goedhart, 2021). Statistical analysis of mesh density was performed by one-way ANOVA and post-hoc Dunnet and Tukey multiple comparison tests. Means ± standard deviations and adjusted p-values are reported in the figure legends.

smiFISH

Samples were prepared according to previously published protocols (Calvo et al., 2021; Lu et al., 2023; Tsanov et al., 2016). The probes were described in (Bailey et

al., 2024). Briefly, ovaries were dissected in 1X PBS and washed with PBST and smiFISH wash buffer (2X solution of 0.3 M sodium citrate and 3 M sodium chloride (SSC), 10% deionized formamide). Then, the appropriate annealed mRNA probes were added in hybridization buffer (10% dextran sulphate, 2X SSC, 10% deionized formamide) overnight at 37°C. The next day, ovaries were washed with smiFISH wash buffer and PBST and mounted in ProLong Gold for imaging the following day.

Microscopy

Localization, mesh, and smFISH images were acquired using Zeiss LSM 700 confocal microscope with a 40x/1.3 or 63x/1.4 oil objective (Banerjee lab). Brightfield images of whole ovaries were acquired using Zeiss Axio Zoom.V16 Macro Zoom with X-Cite TURBO LED 6-Channel light source, driven by SlideBook (3i).

RT-PCR

w^{1118} flies were fattened with yeast paste overnight at 25°C. 100 pairs of ovaries were dissected in 1X PBS. Total RNA extraction was performed as described (Bremer et al., 2024). Sema2a cDNA was synthesized with SuperScript III using a gene-specific primer 5' CTTGAATTTGCCATTGAAGGCAGC 3'. Ethanol precipitation was performed and the purity and concentration of the cDNA was assessed with a NanoDrop. The cDNA was amplified with Phusion High-Fidelity DNA Polymerase using the following steps: initial denaturation 98°C, 0:30; 30 cycles 98°C, 0:30, 68.2°C, 0:30, 72°C, 0:30, final extension 72°C, 5:00, and infinite hold 4°C.

For sequence present in all isoforms:

Forward primer: 5’ GAACGAAGATCGAGATACGCTCTATG 3’

Reverse primer: 5’ CTTGAATTTGCCATTGAAGGCAGC 3’

For Sema2a isoform A:

Forward primer: 5’ CCATTTGCCAGTGAAATCAATTCC 3’

Reverse primer: 5’ TAAATCGCAGTTGAGTTGTCGAGG 3’

The amplified product was sent to Plasmidsaurus to confirm sequence.

Detailed thermocycler protocols and primers for Sema2a isoforms C and E are available upon request.

Protein expression and purification

Acanthamoeba castellani actin, Capu-CT, and Capu-NT constructs were expressed and purified using published protocols (Vizcarra 2011, Bor et al 2012). Sema2a protein was gifted by Daniel Rozbesky.

Briefly, Capu-CT and Capu-NT were expressed in Rosetta competent cells and grown in Terrific Broth at 37°C until they reached an OD_{600} of 0.6-0.7. Cells were induced with 0.25 mM isopropyl-β-d-thiogalactoside at 18°C overnight. The resulting cell pellets were harvested, flash frozen with liquid nitrogen, and stored at -80°C. Purification of Capu-CT was performed using Talon resin and MonoQ anion exchange as described (Vizcarra et al., 2011). Purification of Capu-NT was performed using glutathione agarose resin and the protein was cleaved from GST using PreScission Protease overnight at 4°C. For CapuNT, the protein was concentrated and gel-filtered on the Superdex 200 10/300 GL column as described (Bor et al., 2012). Purified fractions were dialyzed into storage buffer (20 mM Tris pH 8.0, 100 mM NaCl, 1 mM

DTT, 50% glycerol). Aliquots were flash frozen with liquid nitrogen and stored at -80°C. The concentration of the Capu-CT construct was calculated based on quantitative Sypro-Red (Invitrogen) staining while the concentration of Capu-NT was based on the extinction coefficient from Bor et al. (Bor et al., 2012)

Human Profilin-1 was expressed and purified as described for Drosophila profilin (Chic) (Bor et al., 2012). Profilin-1 concentration was determined using the extinction coefficient 14,992 M−1 cm−1.

Pyrene-actin polymerization assays

Pyrene assays were performed essentially as described (Bor et al., 2012). Actin polymerization was initiated by the addition of 2× concentrated protein mix in 2× polymerization buffer (1× KMEH buffer: 10 mM HEPES, pH 7.5, 1 mM EGTA, 1 mM $MgCl_2$, 50 mM KCl, and 0.2 mM ATP) to 50 µl of 2× concentrated Mg^{2+}- ATP-actin at a final concentration of 4 µM with 5% pyrene-labeled actin. Mg^{2+}- ATP-actin was prepared just before initiation of the assay by incubating Ca^{2+}-actin in G-buffer with ME exchange buffer (final concentration, 0.05 mM $MgCl_2$ and 0.2 mM EGTA) for 2 minutes at room temperature. The final concentrations of additional proteins used are indicated in figures legends. For reactions containing profilin, actin was preincubated human profilin (at twice the actin molar ratio) prior to use. Pyrene fluorescence was monitored for 1.5-2 hours (with excitation at 365 nm and emission at 407 nm) at 25°C, in an Infinite M Nano+ plate reader (Tecan). The time between mixing of components and the beginning of data collection ranged between 20-30 seconds for each assay.

Acknowledgements

We thank Graydon Gonsalvez for providing us with the TurboID fly line and Daniel Rozbesky for the purified recombinant Sema2a protein. We also thank members of the Quinlan and Wohlschlegel lab for their help and support. Thanks to Orkun Akin for providing many reagents and useful discussions as well as Emil Reisler for lending resources. C.W. especially thanks family and friends for their love and support. This work was supported by NIH grant R01GM096133 to M.E.Q., R35GM153408 to J.W., and award number T32GM145388 to C.W.

Fig. 1

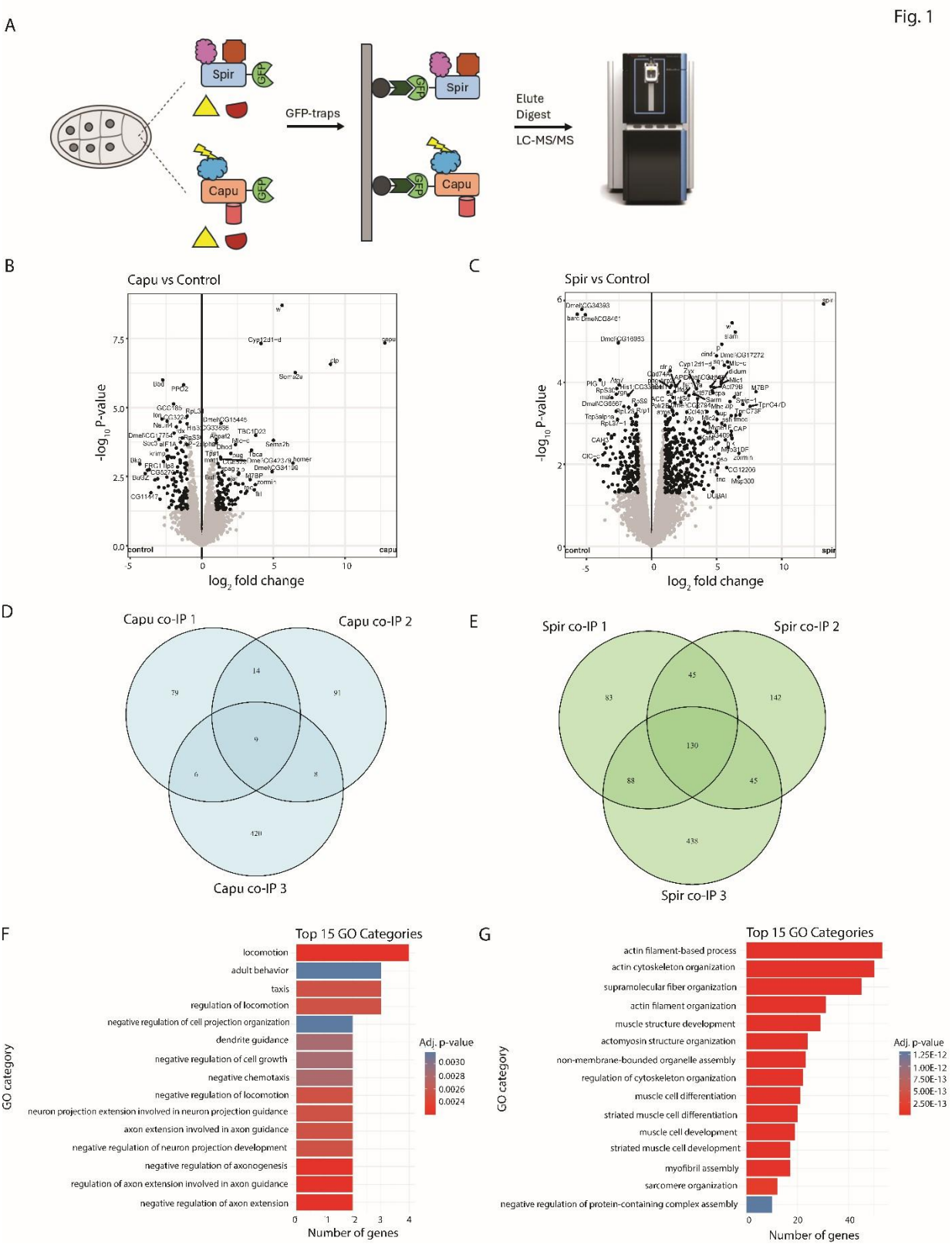
A
Spir
GFP
Capu
GFP-traps
Elute
Digest
LC-MS/MS
B
Capu vs Control
-log10 P-value
log2 fold change
control
capu
C
Spir vs Control
-log10 P-value
log2 fold change
control
spir
D
Capu co-IP 1
Capu co-IP 2
Capu co-IP 3
79
14
91
9
6
8
420
E
Spir co-IP 1
Spir co-IP 2
Spir co-IP 3
83
45
142
130
88
45
438
F
Top 15 GO Categories
GO category
locomotion
adult behavior
taxis
regulation of locomotion
negative regulation of cell projection organization
dendrite guidance
negative regulation of cell growth
negative chemotaxis
negative regulation of locomotion
neuron projection extension involved in neuron projection guidance
axon extension involved in axon guidance
negative regulation of neuron projection development
negative regulation of axonogenesis
regulation of axon extension involved in axon guidance
negative regulation of axon extension
Adj. p-value
0.0030
0.0028
0.0026
0.0024
Number of genes
G
Top 15 GO Categories
GO category
actin filament-based process
actin cytoskeleton organization
supramolecular fiber organization
actin filament organization
muscle structure development
actomyosin structure organization
non-membrane-bounded organelle assembly
regulation of cytoskeleton organization
muscle cell differentiation
striated muscle cell differentiation
muscle cell development
striated muscle cell development
myofibril assembly
sarcomere organization
negative regulation of protein-containing complex assembly
Adj. p-value
1.25E-12
1.00E-12
7.50E-13
5.00E-13
2.50E-13
Number of genes

Figure 2-1. Characterization of Spir and Capu interactomes using co-IP/MS.

(A) Schematic showing the experimental workflow. GFP-tagged SpirC and CapuA from lysed ovaries were incubated with ChromoTek GFP-trap magnetic agarose beads. Proteins bound to beads were eluted, digested, and analyzed on an Orbitrap Astral mass spectrometer. Three biological replicates were tested in triplicate for each construct, SpirC-GFP, CapuA-GFP, GFP-CapuA. (B-C) Volcano plots of Capu or Spir compared to controls. Gene names shown represent those that have FC > 2 and p-value < 0.05. (D-E) Venn diagrams comparing common proteins shared across three independent replicates of Capu or Spir co-IPs. (F-G) Plot from clusterProfiler in R, showing enriched annotated biological processes of Capu and Spir co-IPs.

Fig. 2

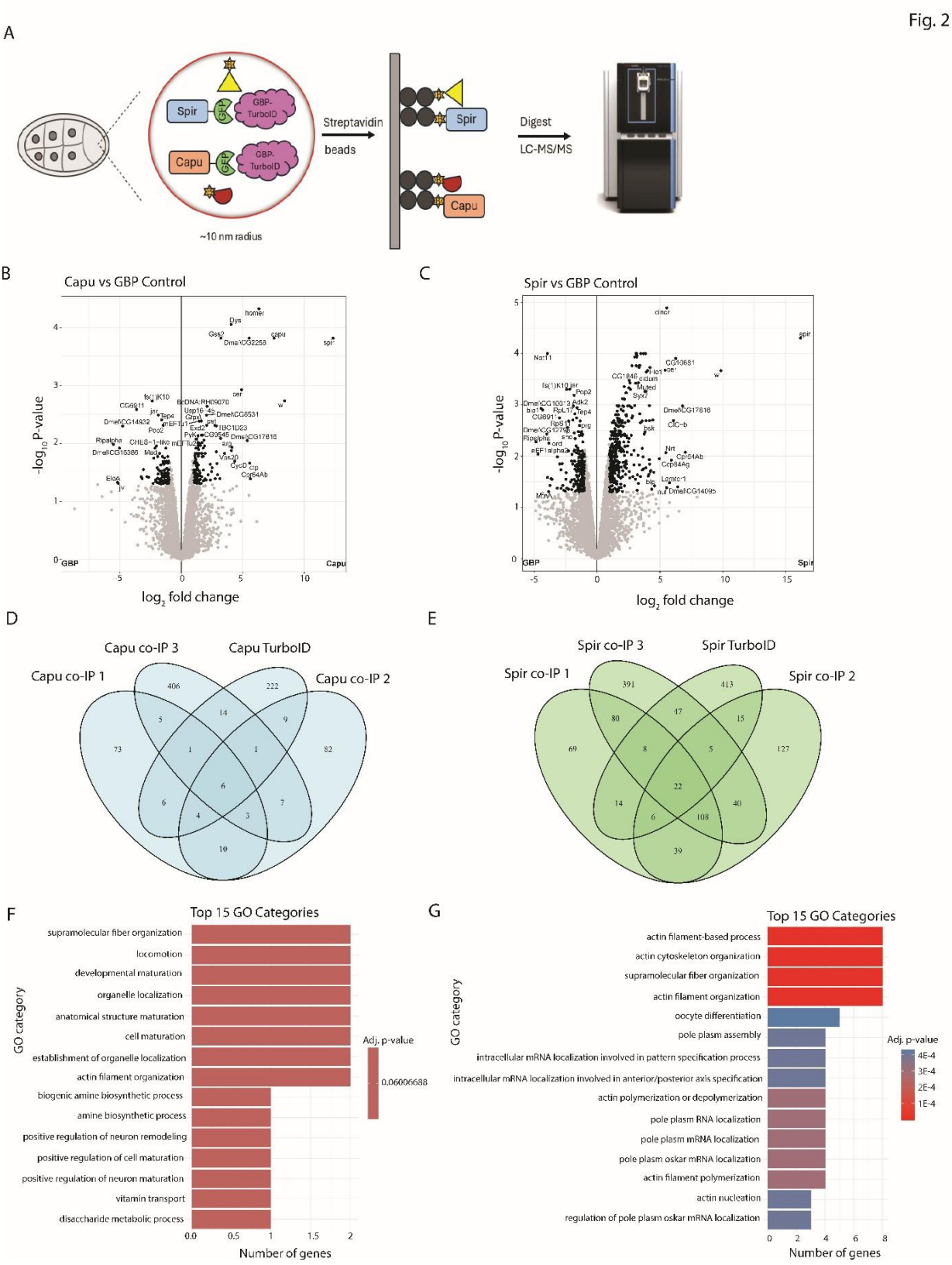
A
Spir
GBP-TurboID
Capu
GBP-TurboID
~10 nm radius
Streptavidin beads
Spir
Capu
Digest
LC-MS/MS
B
Capu vs GBP Control
-log10 P-value
log2 fold change
GBP
Capu
C
Spir vs GBP Control
-log10 P-value
log2 fold change
GBP
Spir
D
Capu co-IP 3
Capu TurboID
Capu co-IP 1
Capu co-IP 2
406
222
14
5
9
73
1
1
82
6
6
4
3
7
10
E
Spir co-IP 3
Spir TurboID
Spir co-IP 1
Spir co-IP 2
391
413
47
80
15
69
8
5
127
22
14
6
108
40
39
F
Top 15 GO Categories
GO category
supramolecular fiber organization
locomotion
developmental maturation
organelle localization
anatomical structure maturation
cell maturation
establishment of organelle localization
actin filament organization
biogenic amine biosynthetic process
amine biosynthetic process
positive regulation of neuron remodeling
positive regulation of cell maturation
positive regulation of neuron maturation
vitamin transport
disaccharide metabolic process
Adj. p-value
0.06006688
Number of genes
G
Top 15 GO Categories
GO category
actin filament-based process
actin cytoskeleton organization
supramolecular fiber organization
actin filament organization
oocyte differentiation
pole plasm assembly
intracellular mRNA localization involved in pattern specification process
intracellular mRNA localization involved in anterior/posterior axis specification
actin polymerization or depolymerization
pole plasm RNA localization
pole plasm mRNA localization
pole plasm oskar mRNA localization
actin filament polymerization
actin nucleation
regulation of pole plasm oskar mRNA localization
Adj. p-value
4E-4
3E-4
2E-4
1E-4
Number of genes

Figure 2-2. Characterization of Spir and Capu interactomes using TurboID proximity labeling. (A) Schematic showing the experimental workflow. GBP-TurboID biotinylates proteins within ~10 nm radius of GFP-tagged SpirC and CapuA. Lysate was incubated with streptavidin magnetic beads. Proteins bound to beads were digested and analyzed on an Orbitrap Astral mass spectrometer. Each construct was tested in triplicate. (B-C) Volcano plots of Capu or Spir compared to the controls. Gene names shown represent those that have FC > 2 and p-value < 0.05. (D-E) Venn diagrams comparing common proteins shared across Capu or Spir co-IPs and TurboID. (F-G) Plot from clusterProfiler in R, showing enriched annotated biological processes of Capu or Spir co-IPs and TurboID.

Table 1. Proteins enriched across all 3 replicates for Capu and Spir co-IPs.

Table 2. Proteins enriched across both coIP and TurboID datasets.

Table 1

Common proteins for Capu co-IPs	Common proteins for Spir co-IPs
w	Tmod
Ctp	M7BP
Capu	Cindr
Sema2a	Didum
Sema2b	Act42A
Agpat2	Spir
TBC1D23	Mlc1
Homer	Jar
Tps1	cpb

Table 2

Common proteins Capu co-IPs and TurboID	Common proteins Spir co-IPs and TurboID
w	Cindr
Ctp	Didum
Capu	W
TBC1D23	Arp2
Homer	Cpb
Tps1	Spir
	Ca
	Swip-1
	cpa
	Tps1
	Par-1
	Vinc
	swa
	Dmel\CG11892
	Strica
	Bor
	Mf
	CLIP-190
	Arpc4
	P5CS
	NP_649372
	Cmb

Fig. 3

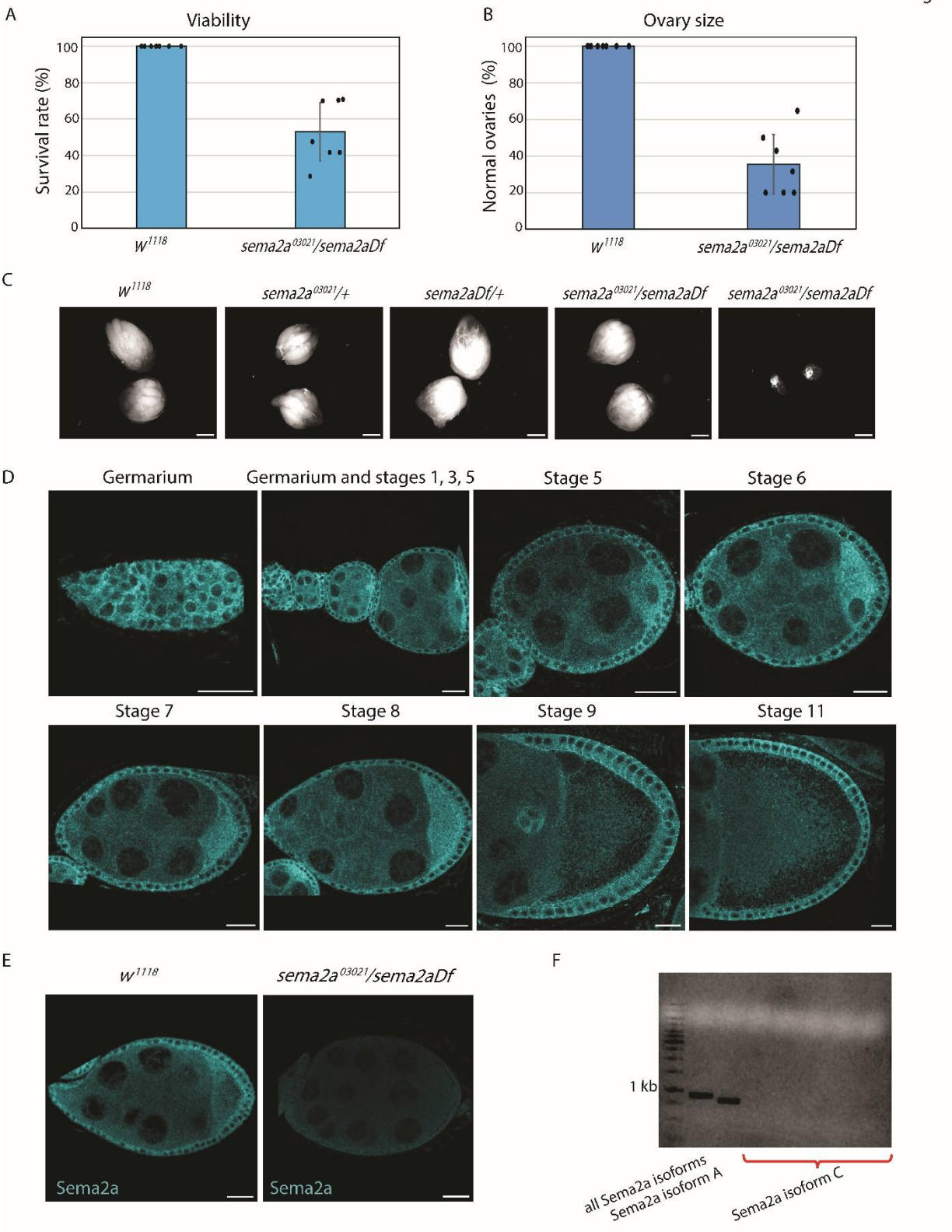
A
Viability
Survival rate (%)
100
80
60
40
20
0
w1118
sema2a03021/sema2aDf
B
Ovary size
Normal ovaries (%)
100
80
60
40
20
0
w1118
sema2a03021/sema2aDf
C
w1118
sema2a03021/+
sema2aDf/+
sema2a03021/sema2aDf
sema2a03021/sema2aDf
D
Germarium
Germarium and stages 1, 3, 5
Stage 5
Stage 6
Stage 7
Stage 8
Stage 9
Stage 11
E
w1118
sema2a03021/sema2aDf
Sema2a
Sema2a
F
1 kb
all Sema2a isoforms
Sema2a isoform A
Sema2a isoform C

Figure 2-3. Sema2a plays an intracellular role in oogenesis. (A) Viability of *sema2a*^{03021}/*sema2aDf* flies compared to *w*^{1118}. Individual dots represent biological replicates. N=95 across all 7 replicates. (B) Ovary size of *sema2a*^{03021}*/sema2aDf* flies compared to *w*^{1118}. Individual dots represent replicates from those that survived in (A). (C) Brightfield images of *sema2a*^{03021}*/sema2aDf* ovaries compared to wild type and heterozygotes. Both normal sized (~36%) and small (~64%) ovaries are shown for *sema2a*^{03021}*/sema2aDf.* Scale bars are 1 mm. (D) Sema2a detected with anti-Sema2a antibody. The protein is evident in the germarium. It is enriched in the oocytes from ~stage 3 – stage 9. Sema2a is present in the somatic follicle cells in all stages of the ovariole and in the migrating border cells during stage 9. Scale bars are 20 μm. (E) Sema2a staining for *w*^{1118} and *sema2a*^{03021}*/sema2aDf* stage 7 egg chambers. *sema2a*^{03021}*/sema2aDf* shows substantial decrease in signal compared to *w*^{1118} and confirms loss of Sema2a. (F) Agarose gel electrophoresis of RT-PCR samples amplifying a sequence present in all isoforms, Sema2a isoform A sequence, or Sema2a isoform C sequence. A total of three pairs of primers detected no product for isoform C. The gel above shows one primer set with a temperature gradient.

Fig. 4

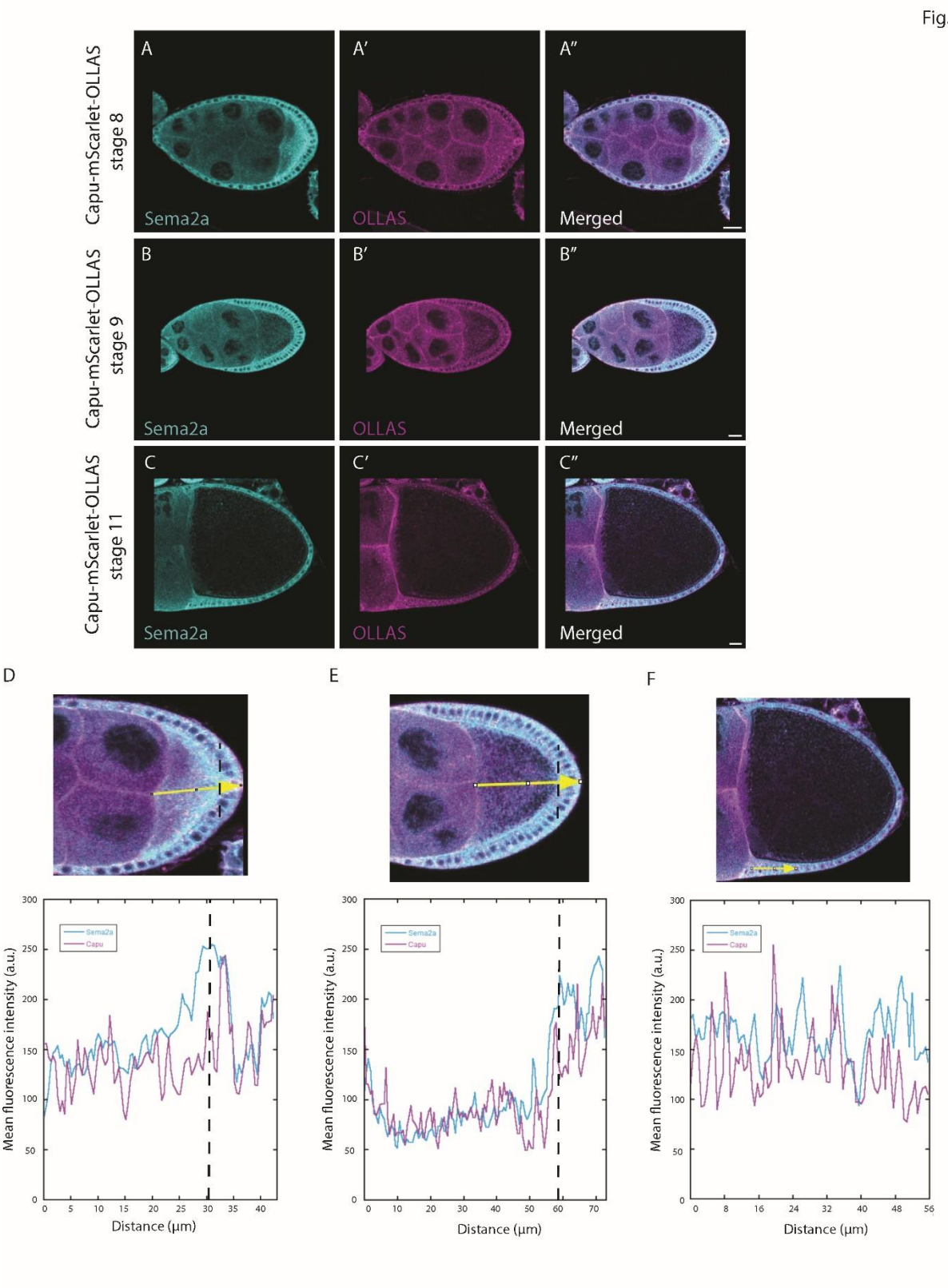
Capu-mScarlet-OLLAS stage 8
Capu-mScarlet-OLLAS stage 9
Capu-mScarlet-OLLAS stage 11
A
A′
A″
B
B′
B″
C
C′
C″
Sema2a
OLLAS
Merged
D
E
F
Mean fluorescence intensity (a.u.)
Distance (μm)
Sema2a
Capu

Figure 2-4. Colocalization of Sema2a and Capu. Egg chamber expressing Capu-mScarlet-OLLAS and stained with antibodies against Sema2a and OLLAS. (A) stage 8, (B) stage 9, and (C) stage 11. At stage 8, Sema2a and Capu colocalize mostly in the posterior of the oocyte and follicle cells. At stage 9, the majority of the overlap is in the follicle cells. At stage 11, Sema2a and Capu are not detected in the oocyte but remain in the follicle cells. Scale bars are 20 μm. (D-F) Intensity profiles from (A-C'') showing similar expression patterns of Sema2a and Capu.

Fig. 5

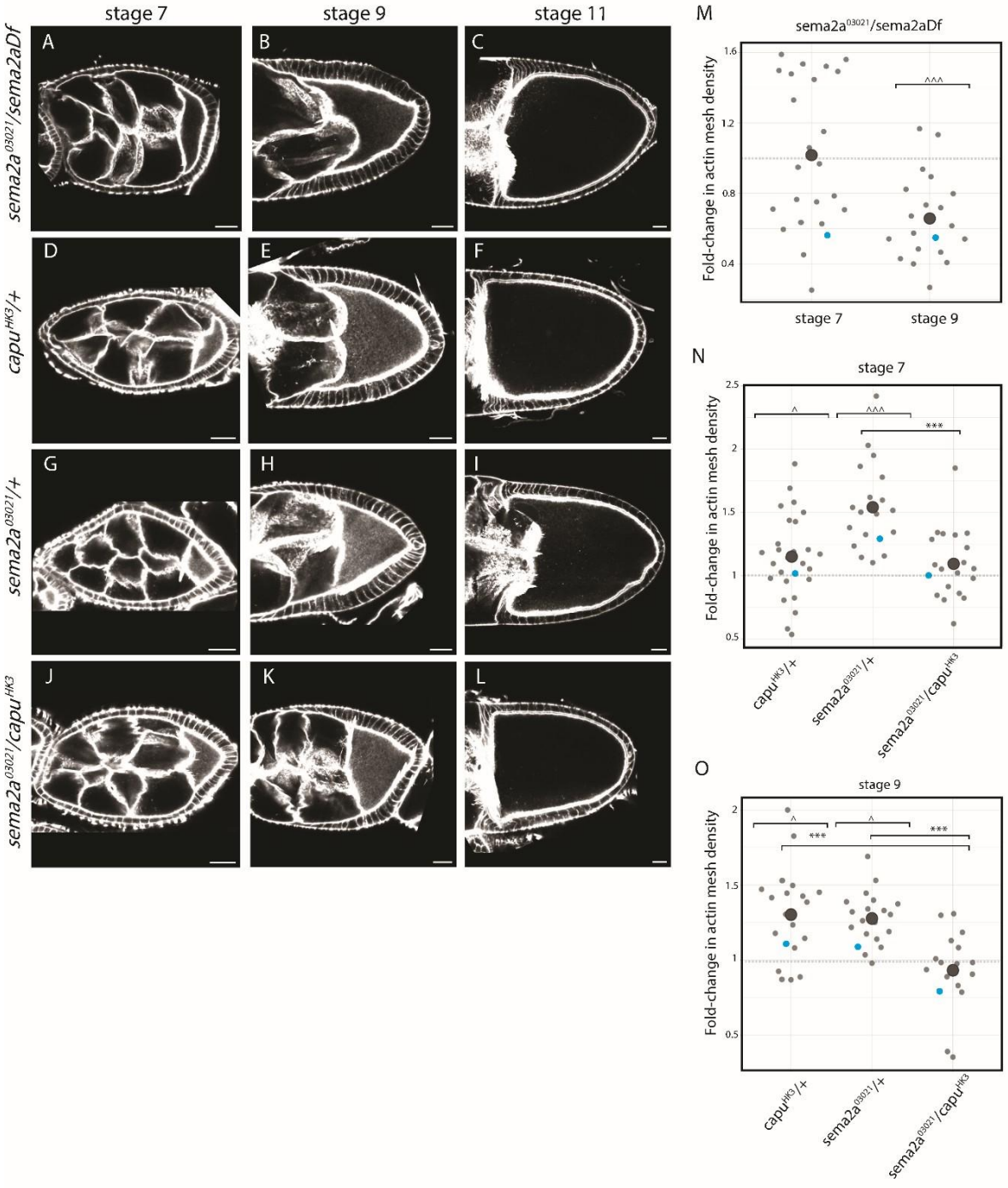
stage 7
stage 9
stage 11
sema2a03021/sema2aDf
capuHK3/+
sema2a03021/+
sema2a03021/capuHK3
A
B
C
D
E
F
G
H
I
J
K
L
M
sema2a03021/sema2aDf
Fold-change in actin mesh density
stage 7
stage 9
N
stage 7
capuHK3/+
sema2a03021/+
sema2a03021/capuHK3
O
stage 9

Figure 2-5. Sema2a and Capu protein levels affect actin mesh density. Egg chambers stained with phalloidin to measure actin mesh density, (A-C) *sema2a*^{03021}*/sema2aDf,* (D-F) *capu*^{HK3}/+, (G-I) *sema2a*^{03021}/+, and (J-L) *sema2a*^{03021}/ *capu*^{HK3}*.* Scale bars are 20 μm. (M-O) Quantification of actin mesh density. The average intensity within the oocyte was normalized to a population of egg chambers that express Histone-GFP, stained together, as a wild-type internal control. Dotted line at 1 represents the control intensity level. Blue data points correspond to the images in (A-L). (M) Average mesh intensity is the same as wild-type in Sema2a-nulls, stage 7 (1.0 ± 0.4, n = 24, p = 0.19). At stage 9, mesh intensity is below wild-type (0.65 ± 0.24 fold-change, n = 20, p = 0.0014) (Values are means ± standard deviations and p-values were determined with a one-way ANOVA and post-hoc Dunnet's multiple comparisons test to compare each experimental genotype against the wild-type control). When stage 7 data are analyzed as two groups, decrease in mesh density of one population is comparable to the stage 9 level (0.65 ± 0.19, n = 12), while the other had an increase in mesh density (1.38 ± 0.22, n = 12). The two groups differ significantly from each other ($p < 0.001$ based on a Student's two tailed T-test performed after an F-test confirmed that the two samples have equal variance, p = 0.586). (N) Comparison of heterozygotes and transheterozygotes to wild-type reveals a genetic interaction. Stage 7 *capu*^{HK3}/+ mesh density is slightly higher than wild-type (1.15 ± 0.33 fold change, n = 27, p = 0.016 with Dunnet and p = 0.051 with Tukey multiple comparison tests). The mesh density of *sema2a*^{03021}/+ oocytes is significantly higher (1.54 ± 0.35, n = 19, $p < 0.001$). The stage 7 *sema2a*^{03021}*/capu*^{HK3} trans-heterozygote did not differ from wild-type (0.93 ± 0.28, n = 21, p = 0.07), consistent with a dosage compensation effect. Between samples: *capu*^{HK3}/+ vs. *sema2a*^{03021}*/capu*^{HK3}, p = 0.980; *sema2a*^{03021}/+ vs. *sema2a*^{03021}*/capu*^{HK3}, $p < 0.001$. (O) At stage 9, the mesh density of both heterozygotes was denser than wild-type (1.3 ± 0.2-fold change, n = 20, p = 0.031 and 1.3 ± 0.3-fold change, n = 20, p = 0.016, respectively). A one-way ANOVA and Tukey post-hoc test indicates that the two phenotypes do not differ from one another (p = 1.00). Again, the transheterozygotes did not differ from wild-type (0.9 ± 0.3, n = 17, p = 0.75). Between samples: *capu*^{HK3}/+ vs. *sema2a*^{03021}*/capu*^{HK3}, $p < 0.001$; *sema2a*^{03021}/+ vs. *sema2a*^{03021}*/capu*^{HK3}, $p < 0.001$.

***p<0.001 for comparisons between experimental samples.

^p<0.05 and ^^^p<0.001 for comparisons between experimental and Histone-GFP within same sample.

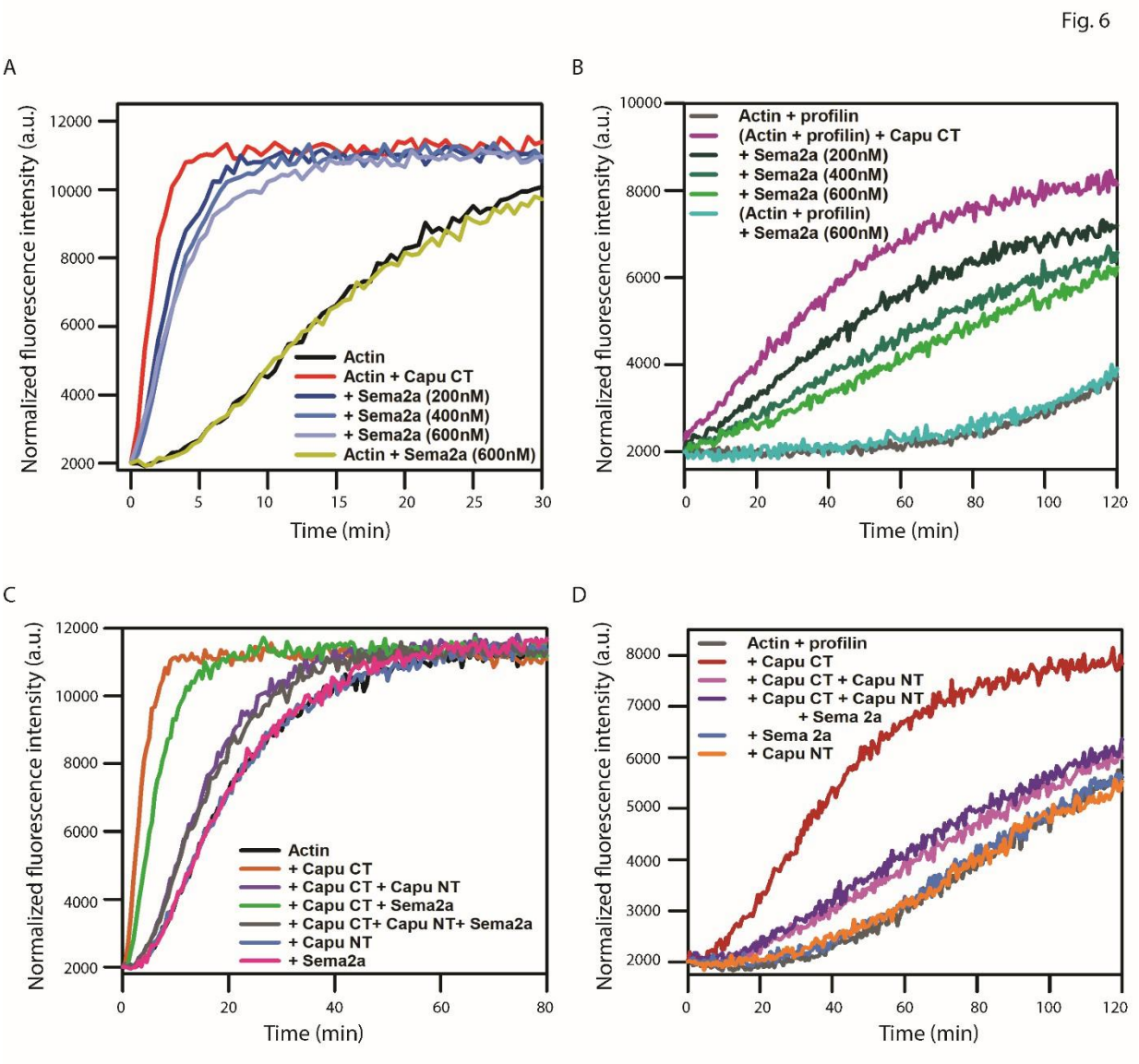

Figure 2-6. Effect of Sema2a on Capu-mediated actin assembly. (A) Representative normalized fluorescence traces of actin polymerization for samples containing 4 μM actin monomers (5% pyrene labeled), 20nM Capu CT, and a range of Sema2a. (B) Representative normalized fluorescence traces of actin polymerization for samples containing 4 μM actin monomers (5% pyrene labeled) with 8 μM human profilin, 20nM Capu CT, and a range of Sema2a. (C) Representative normalized fluorescence traces of actin polymerization for samples containing 4 μM actin monomers (5% pyrene labeled), 20nM Capu CT, 200 nM Capu NT, and 200 nM Sema2a. (D) Representative normalized fluorescence traces of actin polymerization for samples containing 4 μM actin monomers (5% pyrene labeled) with 8 μM human profilin., 20nM Capu CT, 200 nM Capu NT, and 600 nM Sema2a.

Fig. 7

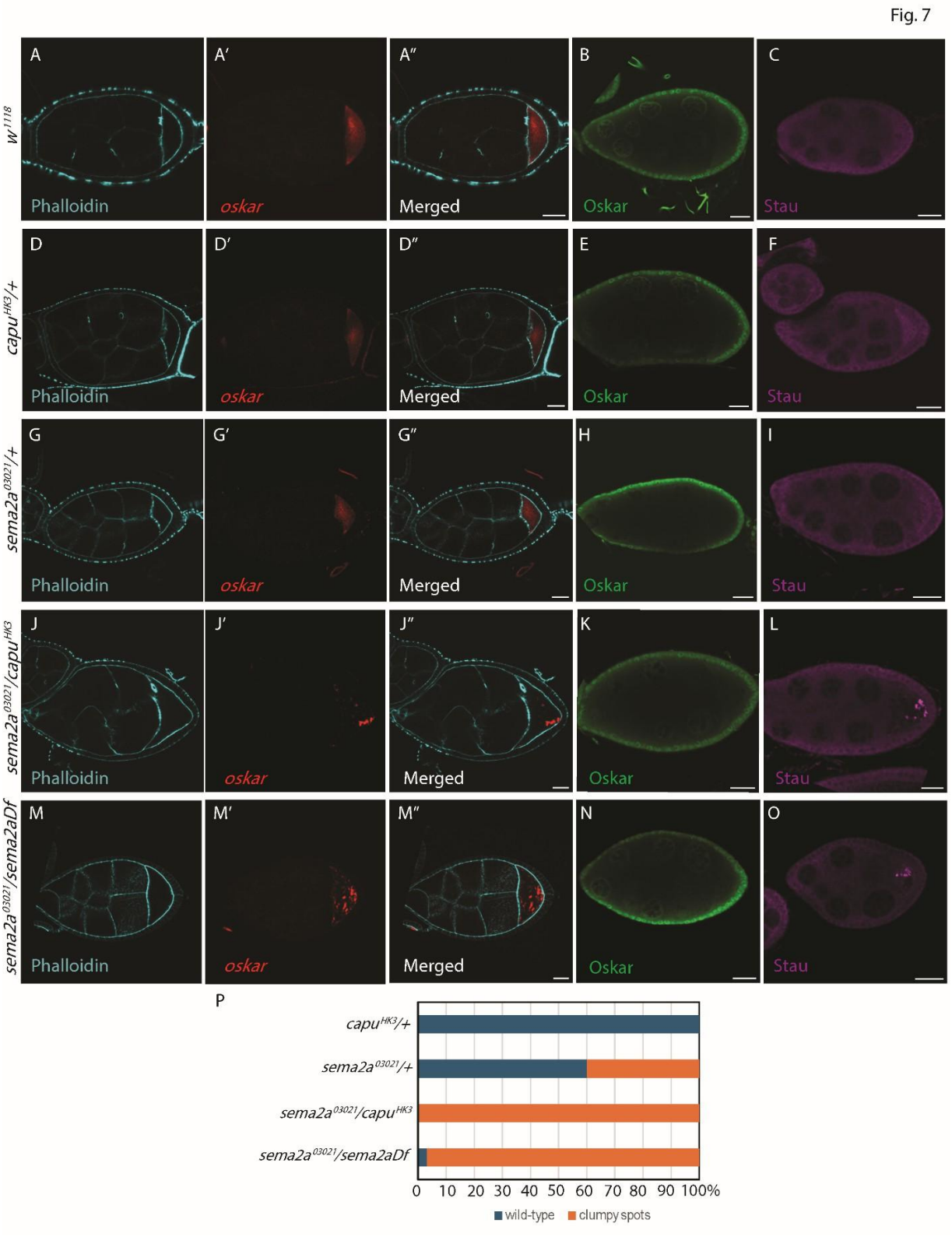
w1118
capuHK3/+
sema2a03021/+
sema2a03021/capuHK3
sema2a03021/sema2aDf
A
A′
A″
B
C
D
D′
D″
E
F
G
G′
G″
H
I
J
J′
J″
K
L
M
M′
M″
N
O
Phalloidin
oskar
Merged
Oskar
Stau
P
capuHK3/+
sema2a03021/+
sema2a03021/capuHK3
sema2a03021/sema2aDf
0 10 20 30 40 50 60 70 80 90 100%
wild-type
clumpy spots

Figure 2-7. Sema2a/Capu trans-heterozygote and Sema2a-nulls disrupt *osk* mRNA localization. Stage 7 egg chambers stained with phalloidin and *osk* mRNA probe, (A-A'') w^{1118}, (D-D'') $capu^{HK3}$/+, (G-G'') $sema2a^{03021}$/+, (J-J'') $sema2a^{03021}$/ $capu^{HK3}$, and (M-M'') $sema2a^{03021}$/$sema2aDf$. Both $sema2a^{03021}$/ $capu^{HK3}$ and $sema2a^{03021}$/$sema2aDf$ show displacement of *osk* to concentrated puncta, or clumps, compared to wild-type and heterozygotes. Scale bars are 20 μm. (B, E, H, K, N) Oskar protein staining for the respective constructs. Translation and localization of Osk is not impacted in any genotype. Scale bars are 20 μm. (C, F, I, L, O) Stau protein staining for the respective constructs. Stau displacement matches that of *osk* in $sema2a^{03021}$/ $capu^{HK3}$ and $sema2a^{03021}$/$sema2aDf$ egg chambers. Scale bars are 20 μm. (P) Quantification of different phenotypes for $capu^{HK3}$/+ (n=18), $sema2a^{03021}$/+ (n=25), $sema2a^{03021}$/$capu^{HK3}$ (n=14), and $sema2a^{03021}$/$sema2aDf$ (n=31). $sema2a^{03021}$/ $capu^{HK3}$ and $sema2a^{03021}$/$sema2aDf$ have all or almost all clumpy spots compared to the heterozygotes.

Fig. 8

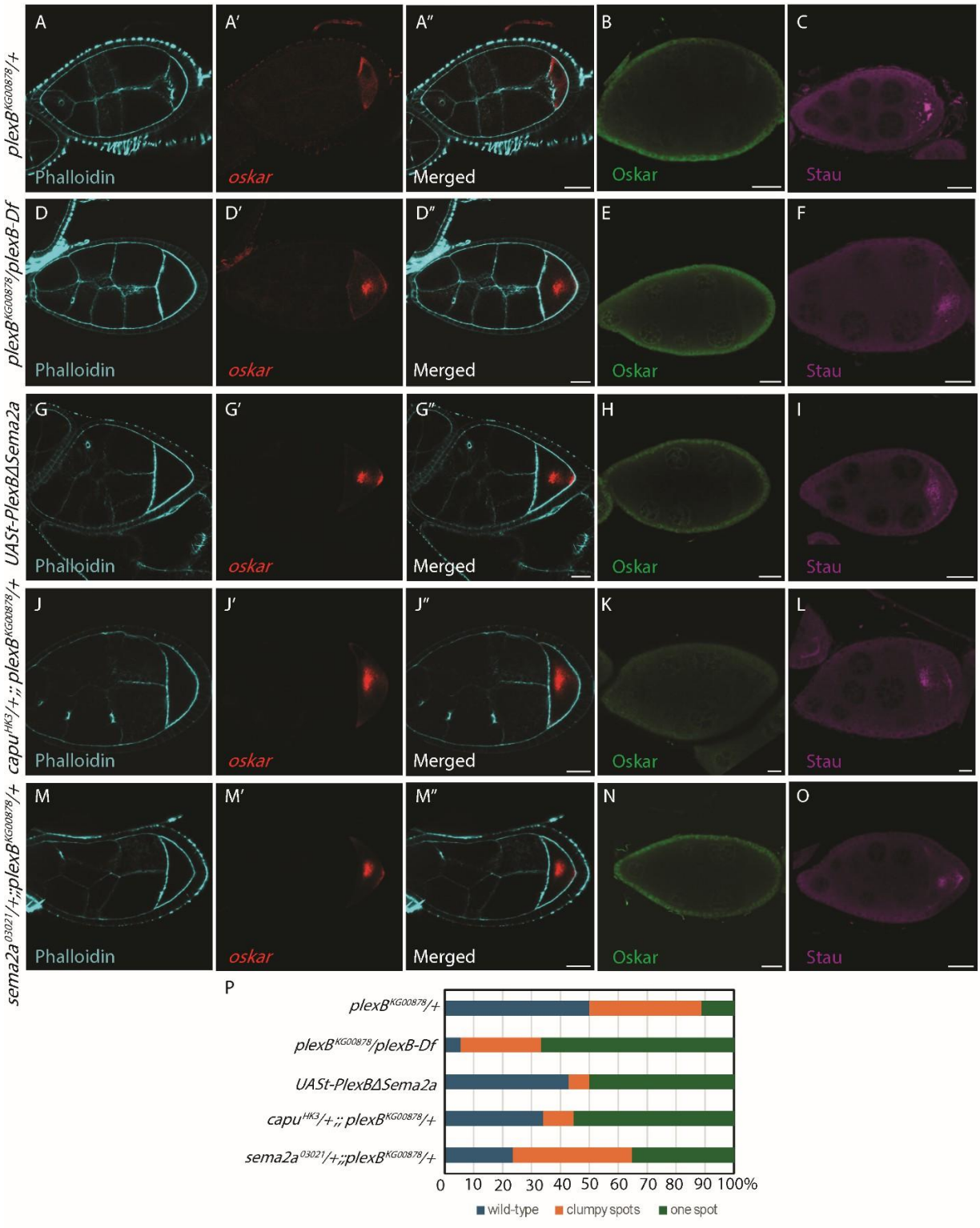
plexB^KG00878/+
plexB^KG00878/plexB-Df
UASt-PlexBΔSema2a
capu^HK3/+;; plexB^KG00878/+
sema2a^03021/+;;plexB^KG00878/+
A
A′
A″
B
C
D
D′
D″
E
F
G
G′
G″
H
I
J
J′
J″
K
L
M
M′
M″
N
O
Phalloidin
oskar
Merged
Oskar
Stau
P
plexB^KG00878/+
plexB^KG00878/plexB-Df
UASt-PlexBΔSema2a
capu^HK3/+;; plexB^KG00878/+
sema2a^03021/+;;plexB^KG00878/+
0 10 20 30 40 50 60 70 80 90 100%
wild-type
clumpy spots
one spot

Figure 2-8. PlexB mutants exhibit *osk* mRNA localization that is different from Sema2a mutants. Stage 7 egg chambers stained with phalloidin and *osk* mRNA probe. Phenotypes varied between diffuse, one large spot, and clumps of *osk* mRNA. (A-A'') *osk* mRNA is diffuse in most $plexB^{KG00878}$/+ chambers. A large single spot of osk mRNA is observed in most (D-D'') $plexB^{KG00878}$/*plexB-Df*, (G-G'') UASt-PlexBΔSema2a, and (J-J'') $capu^{HK3}$;; $plexB^{KG00878}$ oocytes. Similar frequency of clumpy and single spot *osk* mRNA in (M-M'') $sema2a^{03021}$/ $plexB^{KG00878}$. Scale bars are 20 μm. (B, E, H, K, N) Oskar protein staining for the respective genotypes. Translation and localization of Osk is not impacted in all genotypes. Scale bars are 20 μm. (C, F, I, L, O) Stau protein staining for the respective genotypes. Central cluster or spots of Stau matches that of *osk*. Scale bars are 20 μm. (P) Quantification of different phenotypes for $plexB^{KG00878}$/+ (n=36), $plexB^{KG00878}$/*plexB-Df* (n=18), UASt-PlexBΔSema2a (n=14), $capu^{HK3}$;; $plexB^{KG00878}$ (n=47), $sema2a^{03021}$/$plexB^{KG00878}$ (n=17). Most PlexB mutants have one central spot unlike Sema2a mutants which only had clumpy spots.

Fig. S1

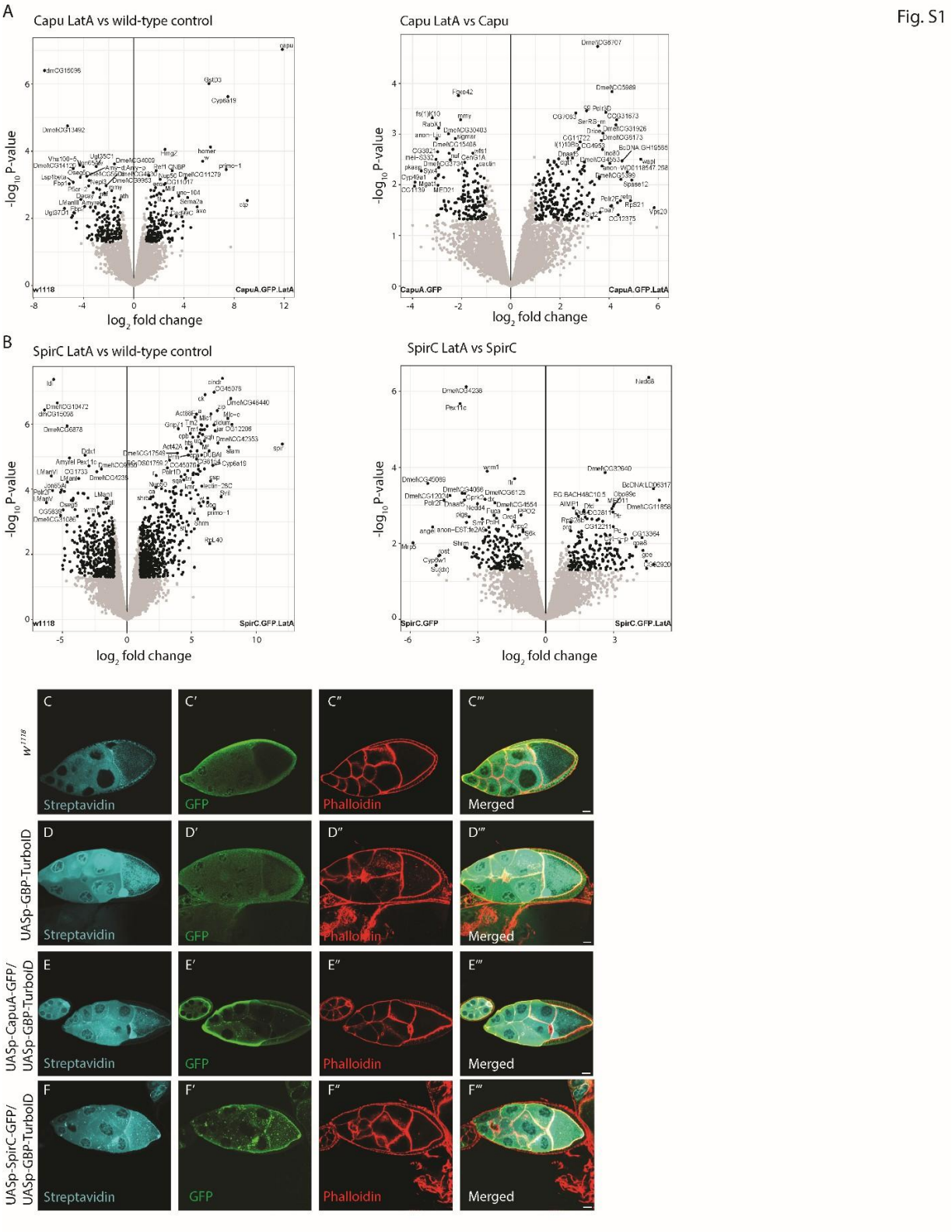
A
Capu LatA vs wild-type control
Capu LatA vs Capu
-log10 P-value
log2 fold change
w1118
CapuA.GFP.LatA
CapuA.GFP
B
SpirC LatA vs wild-type control
SpirC LatA vs SpirC
SpirC.GFP
SpirC.GFP.LatA
C
C′
C″
C‴
w1118
Streptavidin
GFP
Phalloidin
Merged
UASp-GBP-TurboID
D
D′
D″
D‴
UASp-CapuA-GFP/
UASp-GBP-TurboID
E
E′
E″
E‴
UASp-SpirC-GFP/
UASp-GBP-TurboID
F
F′
F″
F‴

Figure 2-S1. Enrichment of co-IPs performed with Latrunculin A present and validation of proximity labeling. (A) Volcano plots showing Capu with addition of 10 μM Lat A compared to wild-type or compared to Capu without addition of LatA. First plot shows same proteins – Ctp, Sema2a, Homer, etc. Second plot shows that there is no change between ± Lat A. (B) Volcano plots showing Spir with addition of 10 μM Lat A compared to wild-type or compared to Spir without addition of LatA. First plot shows same proteins – didum, Cpb, Cindr, etc. Second plot shows that there is no change between ± Lat A. Egg chambers stained with streptavidin, anti-GFP, or phalloidin (C-C’’’) w^{1118}, (D-D’’’) UASp-GBP-TurboID driven by matα-gal4, (E-E’’’) UASp-GBPTurboID and UASp-CapuA-GFP driven by matα-gal4, and (F-F’’’) UASp-TurboID and UASp-SpirC-GFP driven by matα-gal4. The colocalization of GFP-tagged Capu and Spir and streptavidin signal suggests successful biotinylation of proximal proteins within ~10 nm radius of Capu and Spir. Scale bars are 20 μm.

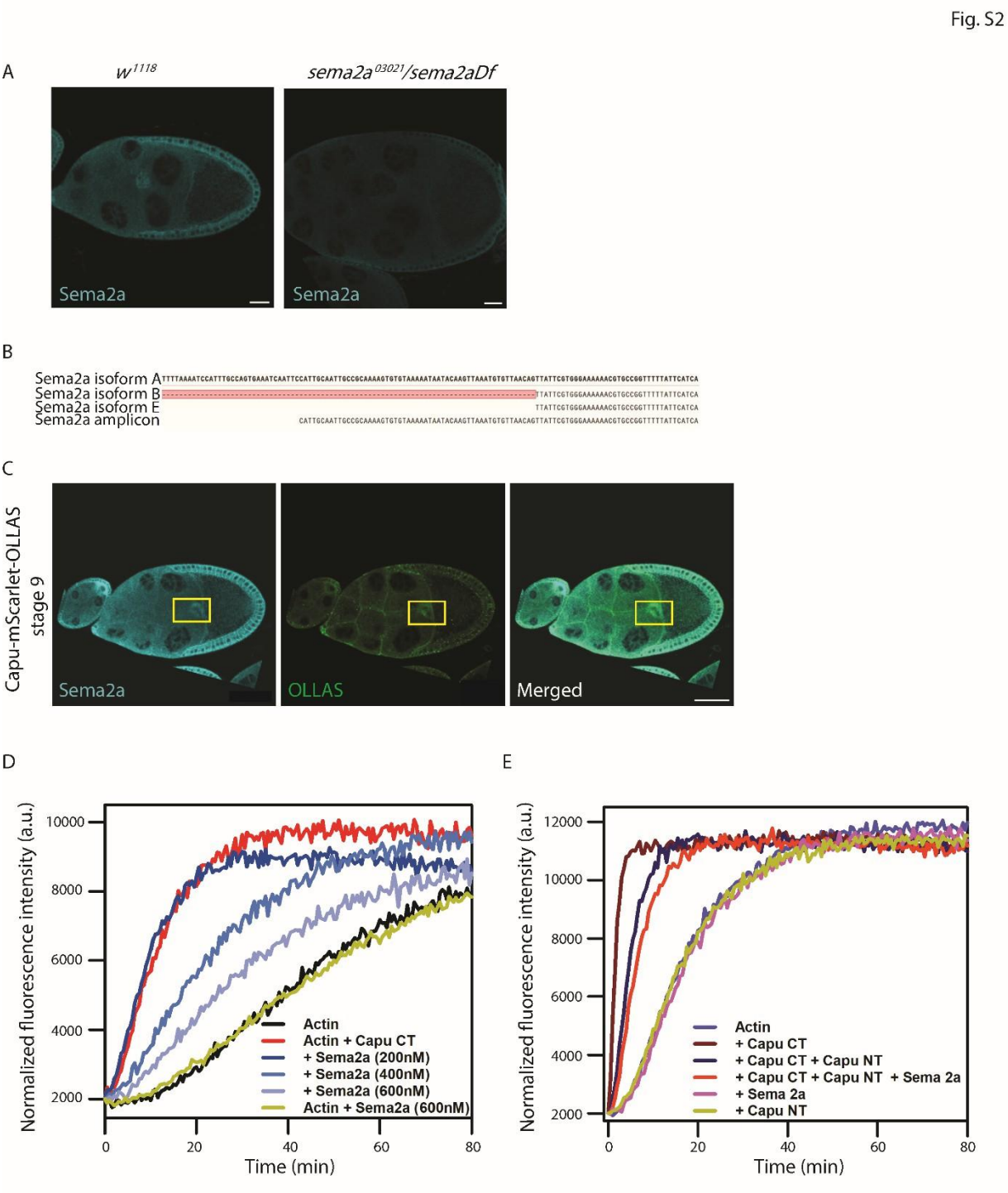

Figure 2-S2. Sema2a localization, isoform, and interaction with Capu. (A) Sema2a staining for *w*^{1118} and *sema2a*^{03021}*/sema2aDf* stage 9 egg chambers. *w*^{1118} shows abundant signal in egg chamber compared to *sema2a*^{03021}*/sema2aDf.* Scale bars are 20 µm. (B) Plasmidsaurus sequencing data comparing Sema2a amplicon to Sema2a isoform sequences. Sema2a amplicon matches that of Sema2a isoform A. (C) Capu-

mScarlet-OLLAS egg chambers stained with Sema2a and OLLAS show signal in the migrating border cells, boxed in yellow. Aside from the well-known role that Capu plays in the mesh, this observation could indicate other unexplored roles of both Capu and Sema2a in border cells. Scale bars are 50 μm. (D) Representative normalized fluorescence traces of actin polymerization for samples containing 2 μM actin monomers (5% pyrene labeled), 20nM Capu CT, and a range of Sema2a. (E) Representative normalized fluorescence traces of actin polymerization for samples containing 4 μM actin monomers (5% pyrene labeled), 20nM Capu CT, 50 nM Capu NT, and 200 nM Sema2a.

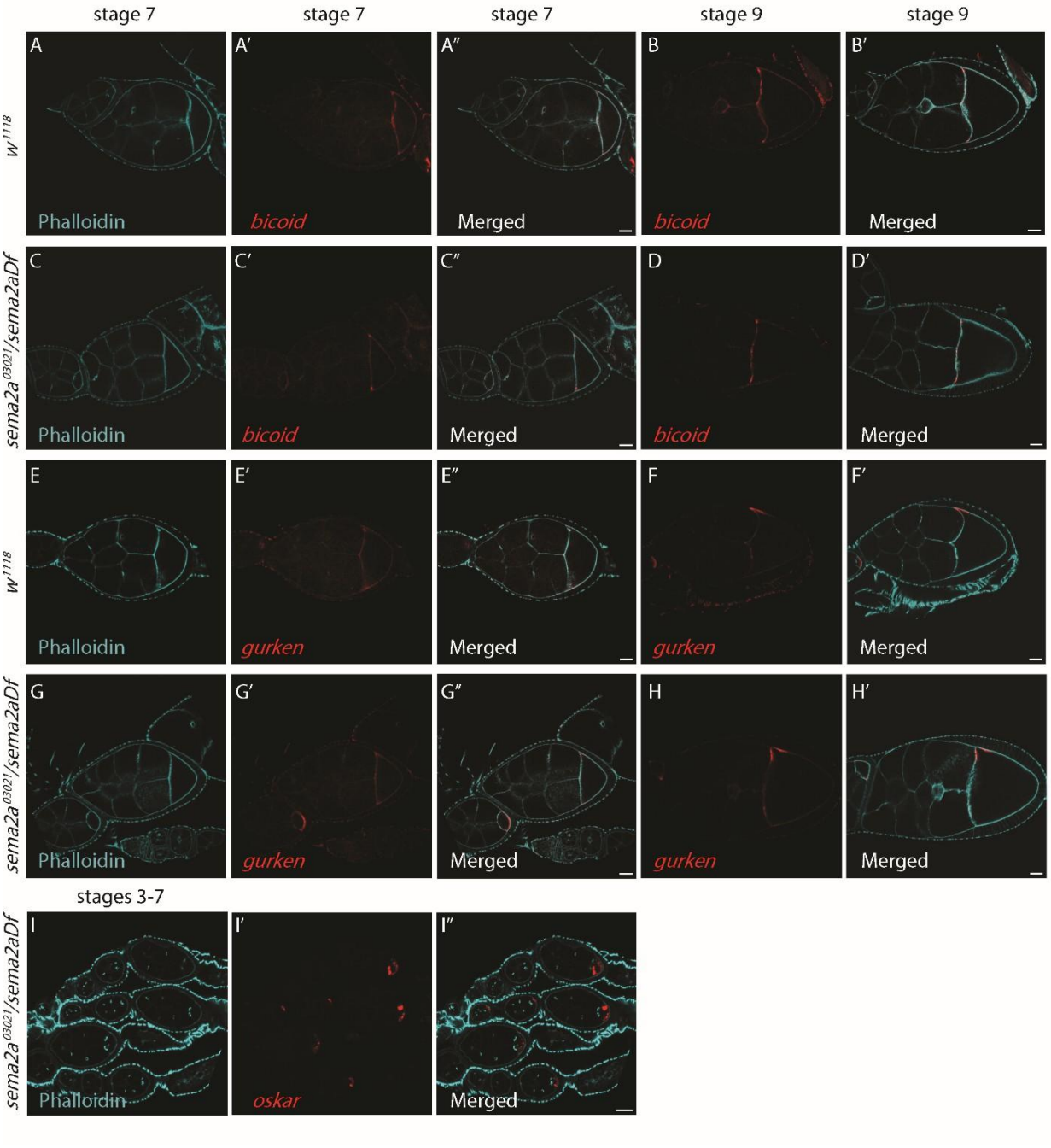

Figure 2-S3. bicoid, gurken, and oskar mRNA localization in sema2a^{03021}/sema2aDf oocytes. Stage 7/8 or stage 9 egg chambers probing for *bicoid (bcd)* (A-B') *w^{1118}* and (C-D') *sema2a^{03021}/sema2aDf.* Localization of *bcd* is normal and comparable to that of wild-type. Stage 7/8 or stage 9 egg chambers probing for *gurken (grk)* (E-F') *w^{1118}* and (G-H') *sema2a^{03021}/sema2aDf.* Localization of *grk* is also unaffected and is similar to that of wild-

type. Scale bars are 20 μm. (I-I'') Stages 3-7 egg chambers of *sema2a*^{03021}*/sema2aDf* stained with phalloidin and *osk* mRNA probe. Disruption of *osk* mRNA starts in very early stages of oogenesis, beginning as early as stage 3.

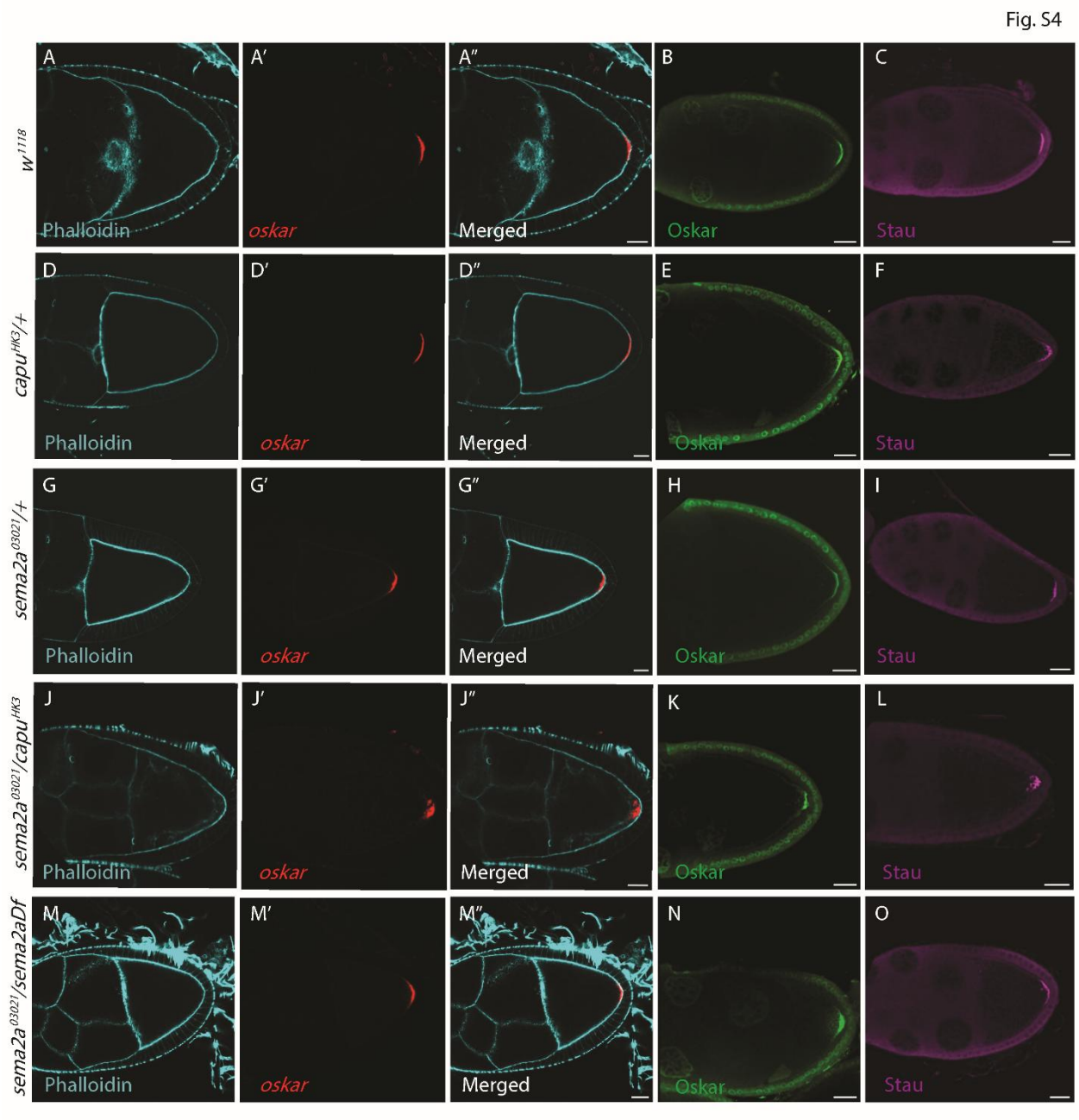

Figure 2-S4. Sema2a/Capu trans-heterozygotes and Sema2a-nulls have normal *osk* mRNA localization by stage 9. Stage 9 egg chambers stained with phalloidin and *osk* mRNA probe, (A-A'') w^{1118}, (D-D'') $capu^{HK3/+}$, (G-G'') $sema2a^{03021}$/+, (J-J'') $sema2a^{03021}$/ $capu^{HK3}$, and (M-M'') $sema2a^{03021}$/*sema2aDf.* The $sema2a^{03021}$/ $capu^{HK3}$ egg chambers have some residual RNP aggregation and clumps while $sema2a^{03021}$/*sema2aDf* have normal *osk* distribution compared to wild-type and heterozygotes. Scale bars are 20 μm. (B, E, H, K, N) Oskar protein staining for the respective constructs. Translation and localization of Osk is normal and matches that of *osk* mRNA. Scale bars are 20 μm. (C, F,

I, L, O) Stau protein staining for the respective constructs. Stau localization is also normal in all genotypes. Scale bars are 20 μm.

Fig. S5

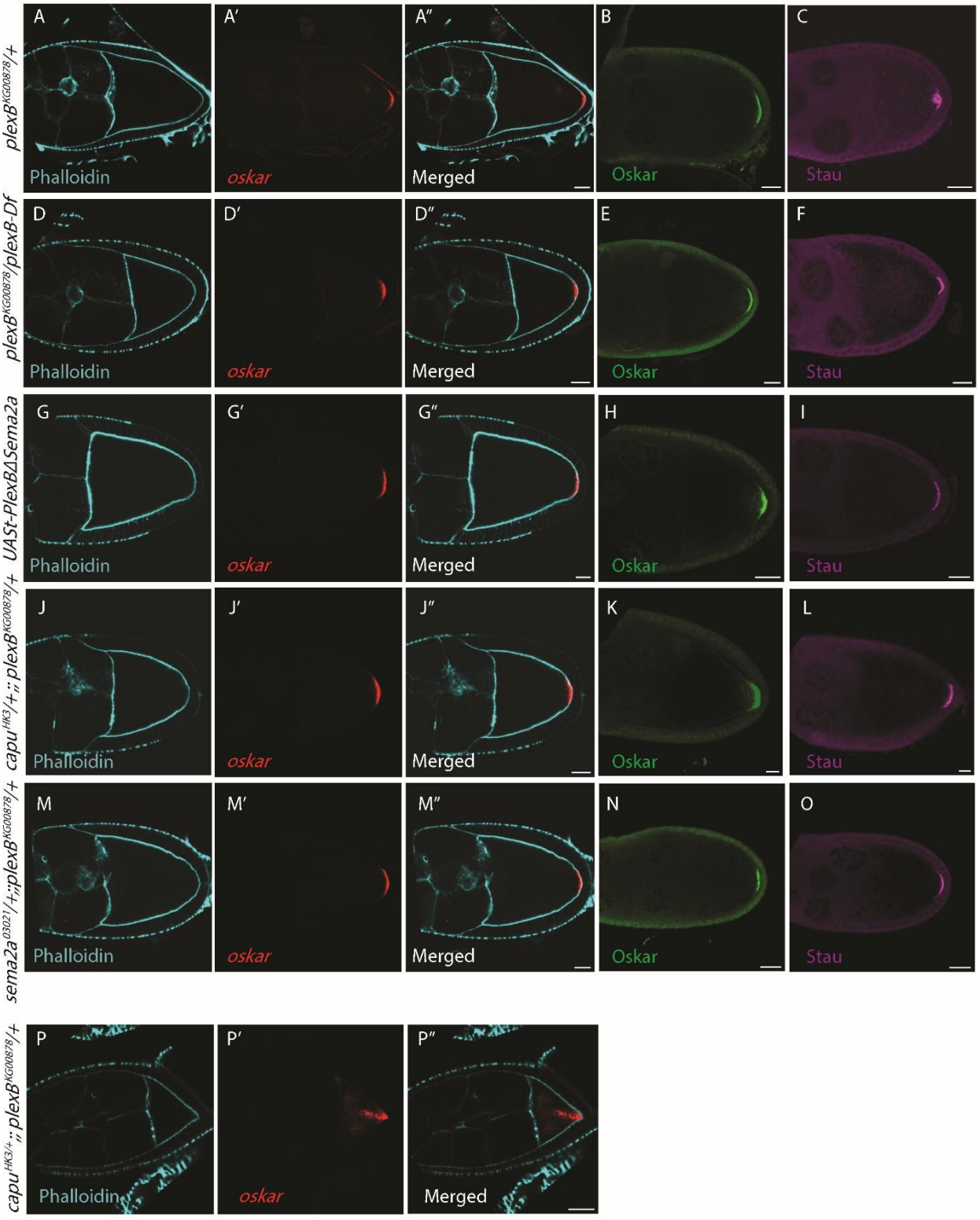
plexB^KG00878/+
A
A′
A″
B
C
Phalloidin
oskar
Merged
Oskar
Stau
plexB^KG00878/plexB-Df
D
D′
D″
E
F
Phalloidin
oskar
Merged
Oskar
Stau
UASt-PlexBΔSema2a
G
G′
G″
H
I
Phalloidin
oskar
Merged
Oskar
Stau
capu^HK3/+;;plexB^KG00878/+
J
J′
J″
K
L
Phalloidin
oskar
Merged
Oskar
Stau
sema2a^03021/+;;plexB^KG00878/+
M
M′
M″
N
O
Phalloidin
oskar
Merged
Oskar
Stau
capu^HK3/+;;plexB^KG00878/+
P
P′
P″
Phalloidin
oskar
Merged

Figure 2-S5. PlexB mutants display *osk* mRNA localization that is normal by stage 9. Stage 9 egg chambers stained with phalloidin and *osk* mRNA probe. (A-A'') *plexB*^{KG00878}/+ chambers, (D-D'') *plexB*^{KG00878}/*plexB-Df* , (G-G'') UASt-PlexBΔSema2a, (J-J'') *capu*^{HK3};; *plexB*^{KG00878} oocytes, and (M-M'') *sema2a*^{03021}/ *plexB*^{KG00878}. *osk* mRNA localization is localized at the posterior and comparable to wild-type in all genotypes. Scale bars are 20 μm. (B, E, H, K, N) Oskar protein staining for the respective genotypes. Translation and localization of Osk is again normal in all genotypes shown. Scale bars are 20 μm. (C, F, I, L, O) Stau protein staining for the respective genotypes. Stau is also normal, similar to both *osk* mRNA and Osk protein. Scale bars are 20 μm. (P-P'') Another phenotype seen in the PlexB-Capu trans-heterozygotes. Stage 8 egg chamber stained with phalloidin and probed for *osk* mRNA. Localization of *osk* shows clumpy spots being transported to the posterior of the oocyte, suggesting defects in transport mechanism. Scale bars are 20 μm.

References

Almuqbil, M., Hamdan, F.F., Mathonnet, G., Rosenblatt, B., Srour, M., 2013. De novo deletion of FMN2 in a girl with mild non-syndromic intellectual disability. Eur. J. Med. Genet. 56, 686–688. https://doi.org/10.1016/j.ejmg.2013.10.003

Ayoob, J.C., Terman, J.R., Kolodkin, A.L., 2006. Drosophila Plexin B is a Sema-2a receptor required for axon guidance. Development 133, 2125–2135. https://doi.org/10.1242/dev.02380

Azoury, J., Lee, K.W., Georget, V., Hikal, P., Verlhac, M.-H., 2011. Symmetry breaking in mouse oocytes requires transient F-actin meshwork destabilization. Development 138, 2903–2908. https://doi.org/10.1242/dev.060269

Bailey, H.M., Cullimore, P.B.M., Bailey, L.A., Quinlan, M.E., 2024. Localization of Drosophila formin, Cappuccino, influences posterior oocyte organization. https://doi.org/10.1101/2024.07.22.604638

Baker, F.C., Neiswender, H., Veeranan-Karmegam, R., Gonsalvez, G.B., 2021. In vivo proximity biotin ligation identifies the interactome of Egalitarian, a Dynein cargo adaptor. Development 148, dev199935. https://doi.org/10.1242/dev.199935

Bates, K.E., Whitington, P.M., 2007. Semaphorin 2a secreted by oenocytes signals through plexin B and plexin A to guide sensory axons in the Drosophila embryo. Dev. Biol. 302, 522–535. https://doi.org/10.1016/j.ydbio.2006.10.015

Bellen, H.J., Levis, R.W., Liao, G., He, Y., Carlson, J.W., Tsang, G., Evans-Holm, M., Hiesinger, P.R., Schulze, K.L., Rubin, G.M., Hoskins, R.A., Spradling, A.C., 2004. The BDGP Gene Disruption Project: Single Transposon Insertions Associated With 40% of Drosophila Genes. Genetics 167, 761–781. https://doi.org/10.1534/genetics.104.026427

Besse, F., Quinto, S.L. de, Marchand, V., Trucco, A., Ephrussi, A., 2009. Drosophila PTB promotes formation of high-order RNP particles and represses oskar translation. Genes Dev. 23, 195–207. https://doi.org/10.1101/gad.505709

Bor, B., Bois, J.S., Quinlan, M.E., 2015. Regulation of the formin Cappuccino is critical for polarity of Drosophila oocytes. Cytoskelet. Hoboken NJ 72, 1–15. https://doi.org/10.1002/cm.21205

Bor, B., Vizcarra, C.L., Phillips, M.L., Quinlan, M.E., 2012. Autoinhibition of the formin Cappuccino in the absence of canonical autoinhibitory domains. Mol. Biol. Cell 23, 3801–3813. https://doi.org/10.1091/mbc.E12-04-0288

Bradley, A.O., Vizcarra, C.L., Bailey, H.M., Quinlan, M.E., 2019. Spire stimulates nucleation by Cappuccino and binds both ends of actin filaments. Mol. Biol. Cell 31, 273–286. https://doi.org/10.1091/mbc.E19-09-0550

Branon, T.C., Bosch, J.A., Sanchez, A.D., Udeshi, N.D., Svinkina, T., Carr, S.A., Feldman, J.L., Perrimon, N., Ting, A.Y., 2018. Egicient proximity labeling in living cells and organisms with TurboID. Nat. Biotechnol. 36, 880–887. https://doi.org/10.1038/nbt.4201

Bremer, K.V., Wu, C., Patel, A.A., He, K.L., Grunfeld, A.M., Chanfreau, G.F., Quinlan, M.E., 2024. Formin tails act as a switch, inhibiting or enhancing processive actin elongation. J. Biol. Chem. 300. https://doi.org/10.1016/j.jbc.2023.105557

Brendza, R.P., Serbus, L.R., Dugy, J.B., Saxton, W.M., 2000. A Function for Kinesin I in the Posterior Transport of oskar mRNA and Staufen Protein. Science 289, 2120–2122. https://doi.org/10.1126/science.289.5487.2120

Calvo, L., Ronshaugen, M., Pettini, T., 2021. smiFISH and embryo segmentation for single-cell multi-gene RNA quantification in arthropods. Commun. Biol. 4, 1–12. https://doi.org/10.1038/s42003-021-01803-0

Cooley, L., Verheyen, E., Ayers, K., 1992. chickadee encodes a profilin required for intercellular cytoplasm transport during Drosophila oogenesis. Cell 69, 173–184. https://doi.org/10.1016/0092-8674(92)90128-Y

Dahlgaard, K., Raposo, A.A., Niccoli, T., St Johnston, D., 2007. Capu and Spire assemble a cytoplasmic actin mesh that maintains microtubule organization in the Drosophila oocyte. Dev Cell 13, 539–53. https://doi.org/10.1016/j.devcel.2007.09.003

Demichev, V., Messner, C.B., Vernardis, S.I., Lilley, K.S., Ralser, M., 2020. DIA-NN: neural networks and interference correction enable deep proteome coverage in high throughput. Nat. Methods 17, 41–44. https://doi.org/10.1038/s41592-019-0638-x

Diao, Fengqiu, Ironfield, H., Luan, H., Diao, Feici, Shropshire, W.C., Ewer, J., Marr, E., Potter, C.J., Landgraf, M., White, B.H., 2015. Plug-and-play genetic access to drosophila cell types using exchangeable exon cassettes. Cell Rep. 10, 1410–1421. https://doi.org/10.1016/j.celrep.2015.01.059

Doerflinger, H., Benton, R., Torres, I.L., Zwart, M.F., St Johnston, D., 2006. Drosophila Anterior-Posterior Polarity Requires Actin-Dependent PAR-1 Recruitment to the Oocyte Posterior. Curr. Biol. 16, 1090–1095. https://doi.org/10.1016/j.cub.2006.04.001

Dold, A., Han, H., Liu, N., Hildebrandt, A., Brüggemann, M., Rücklé, C., Hänel, H., Busch, A., Beli, P., Zarnack, K., König, J., Roignant, J.-Y., Lasko, P., 2020. Makorin 1 controls embryonic patterning by alleviating Bruno1-mediated repression of oskar translation. PLOS Genet. 16, e1008581. https://doi.org/10.1371/journal.pgen.1008581

Dominguez, R., 2016. The WH2 Domain and Actin Nucleation: Necessary but Insugicient. Trends Biochem. Sci. 41, 478–490. https://doi.org/10.1016/j.tibs.2016.03.004

Emery, A., Dunning, K.R., Dinh, D.T., Akison, L.K., Robker, R.L., Russell, D.L., 2023. Dynamic regulation of semaphorin 7A and adhesion receptors in ovarian follicle remodeling and ovulation. Front. Cell Dev. Biol. 11, 1261038. https://doi.org/10.3389/fcell.2023.1261038

Emmons, S., Phan, H., Calley, J., Chen, W., James, B., Manseau, L., 1995. Cappuccino, a Drosophila maternal egect gene required for polarity of the egg and embryo, is related to the vertebrate limb deformity locus. Genes Dev, Q009 9, 2482–94.

Fan, J., Mansfield, S.G., Redmond, T., Gordon-Weeks, P.R., Raper, J.A., 1993. The organization of F-actin and microtubules in growth cones exposed to a brain-derived collapsing factor. J. Cell Biol. 121, 867–878. https://doi.org/10.1083/jcb.121.4.867

Giacobini, P., 2015. Shaping the Reproductive System: Role of Semaphorins in Gonadotropin-Releasing Hormone Development and Function. Neuroendocrinology 102, 200–215. https://doi.org/10.1159/000431021

Goedhart, J., 2021. SuperPlotsOfData—a web app for the transparent display andquantitative comparison of continuous data from digerent conditions. Mol. Biol. Cell 32, 470–474. https://doi.org/10.1091/mbc.E20-09-0583

Gramates, L.S., Agapite, J., Attrill, H., Calvi, B.R., Crosby, M.A., dos Santos, G., Goodman, J.L., Goutte-Gattat, D., Jenkins, V.K., Kaufman, T., Larkin, A., Matthews, B.B., Millburn, G., Strelets, V.B., the FlyBase Consortium, 2022. FlyBase: a guided tour of highlighted features. Genetics 220, iyac035. https://doi.org/10.1093/genetics/iyac035

Higgs, H.N., Peterson, K.J., 2005. Phylogenetic Analysis of the Formin Homology 2 Domain. Mol. Biol. Cell 16, 1–13. https://doi.org/10.1091/mbc.e04-07-0565

Hsiao, Y., Zhang, H., Li, G.X., Deng, Y., Yu, F., Valipour Kahrood, H., Steele, J.R., Schittenhelm, R.B., Nesvizhskii, A.I., 2024. Analysis and Visualization of Quantitative Proteomics Data Using FragPipe-Analyst. J. Proteome Res. 23, 4303–4315. https://doi.org/10.1021/acs.jproteome.4c00294

Hsu, H.-J., Drummond-Barbosa, D., 2017. A visual screen for diet-regulated proteins in the Drosophila ovary using GFP protein trap lines. Gene Expr. Patterns 23–24, 13–21. https://doi.org/10.1016/j.gep.2017.01.001

Hu, H., Marton, T.F., Goodman, C.S., 2001. Plexin B Mediates Axon Guidance in Drosophila by Simultaneously Inhibiting Active Rac and Enhancing RhoA Signaling. Neuron 32, 39–51. https://doi.org/10.1016/S0896-6273(01)00453-6

Hughes, C.S., Moggridge, S., Müller, T., Sorensen, P.H., Morin, G.B., Krijgsveld, J., 2019. Single-pot, solid-phase-enhanced sample preparation for proteomics experiments. Nat. Protoc. 14, 68–85. https://doi.org/10.1038/s41596-018-0082-x

Hung, R.-J., Yazdani, U., Yoon, J., Wu, H., Yang, T., Gupta, N., Huang, Z., van Berkel, W.J.H., Terman, J.R., 2010. Mical links semaphorins to F-actin disassembly. Nature 463, 823–827. https://doi.org/10.1038/nature08724

Jongbloets, B.C., Pasterkamp, R.J., 2014. Semaphorin signalling during development. Development 141, 3292–3297. https://doi.org/10.1242/dev.105544

Kamiyama, D., Kamiyama, R., Nishida, Y., Sego, A., Vining, G.B., Bui, K.C., Fitch, M., Do, H.G.T., Avraham, O., Chihara, T., 2025. The Vap33 signaling axis precisely coordinates the timing of motoneuron dendritogenesis in neural map development. Nat. Commun. 16, 10893. https://doi.org/10.1038/s41467-025-65900-y

Kim-Ha, J., Kerr, K., Macdonald, P.M., 1995. Translational regulation of oskar mRNA by Bruno, an ovarian RNA-binding protein, is essential. Cell 81, 403–412. https://doi.org/10.1016/0092-8674(95)90393-3

Kim-Ha, J., Smith, J.L., Macdonald, P.M., 1991. oskar mRNA is localized to the posterior pole of the Drosophila oocyte. Cell 66, 23–35. https://doi.org/10.1016/0092-8674(91)90136-M

Kolodkin, A.L., Matthes, D.J., Goodman, C.S., 1993. The semaphorin genes encode a family of transmembrane and secreted growth cone guidance molecules. Cell 75, 1389–1399. https://doi.org/10.1016/0092-8674(93)90625-Z

Krauss, J., López de Quinto, S., Nüsslein-Volhard, C., Ephrussi, A., 2009. Myosin-V Regulates oskar mRNA Localization in the Drosophila Oocyte. Curr. Biol., Q005 19, 1058–1063. https://doi.org/10.1016/j.cub.2009.04.062

Kundu, T., Dutta, P., Nagar, D., Maiti, S., Ghose, A., 2020. Coupling of dynamic microtubules to F-actin by Fmn2 regulates chemotaxis of neuronal growth cones. bioRxiv 2020.01.18.911131. https://doi.org/10.1101/2020.01.18.911131

Lasko, P., 2012. mRNA Localization and Translational Control in Drosophila Oogenesis. Cold Spring Harb. Perspect. Biol. 4, a012294. doi.org/10.1101/cshperspect.a012294

Lehmann, R., 2016. Germ Plasm Biogenesis—An Oskar-Centric Perspective. Curr. Top. Dev. Biol., Essays on Developmental Biology, Part A 116, 679–707. https://doi.org/10.1016/bs.ctdb.2015.11.024

Lu, W., Lakonishok, M., Gelfand, V.I., 2023. The dynamic duo of microtubule polymerase Mini spindles/XMAP215 and cytoplasmic dynein is essential for maintaining Drosophila oocyte fate. Proc. Natl. Acad. Sci. 120, e2303376120. https://doi.org/10.1073/pnas.2303376120

Luo, Y., Raible, D., Raper, J.A., 1993. Collapsin: A protein in brain that induces the collapse and paralysis of neuronal growth cones. Cell 75, 217–227. https://doi.org/10.1016/0092-8674(93)80064-L

Manseau, L., Calley, J., Phan, H., 1996. Profilin is required for posterior patterning of the Drosophila oocyte. Development 122, 2109–16.

Manseau, L.J., Schupbach, T., 1989. cappuccino and spire: two unique maternal-egect loci required for both the anteroposterior and dorsoventral patterns of the Drosophila embryo. Genes Dev 3, 1437–52.

Messina, A., Giacobini, P., 2013. Semaphorin Signaling in the Development and Function of the Gonadotropin Hormone-Releasing Hormone System. Front. Endocrinol. 4. https://doi.org/10.3389/fendo.2013.00133

Mhlanga, M.M., Bratu, D.P., Genovesio, A., Rybarska, A., Chenouard, N., Nehrbass, U., Olivo-Marin, J.-C., 2009. In Vivo Colocalisation of oskar mRNA and Trans-Acting Proteins Revealed by Quantitative Imaging of the Drosophila Oocyte. PLOS ONE 4, e6241. https://doi.org/10.1371/journal.pone.0006241

Micklem, D.R., Adams, J., Grünert, S., St Johnston, D., 2000. Distinct roles of two conserved Staufen domains in oskar mRNA localization and translation. EMBO J. 19, 1366–1377. https://doi.org/10.1093/emboj/19.6.1366

Montaville, P., Jégou, A., Pernier, J., Compper, C., Guichard, B., Mogessie, B., Schuh, M., Romet-Lemonne, G., Carlier, M.-F., 2014. Spire and Formin 2 Synergize and Antagonize in Regulating Actin Assembly in Meiosis by a Ping-Pong Mechanism. PLOS Biol. 12, e1001795. https://doi.org/10.1371/journal.pbio.1001795

Montell, D.J., Rorth, P., Spradling, A.C., 1992. slow border cells, a locus required for a developmentally regulated cell migration during oogenesis, encodes Drosophila C/EBP. Cell 71, 51–62.

Moreira, C.M. do N., Kelemen, C.D., Obado, S.O., Zahedifard, F., Zhang, N., Holetz, F.B., Gauglitz, L., Dallagiovanna, B., Field, M.C., Kramer, S., Zoltner, M., 2023. Impact of inherent biases built into proteomic techniques: Proximity labeling and aginity capture compared. J. Biol. Chem. 299, 102726. https://doi.org/10.1016/j.jbc.2022.102726

Nagar, D., Carrington, B., Burgess, S.M., Ghose, A., 2021. Development of motor neurons and motor activity in zebrafish requires F-actin nucleation by Fmn2b. https://doi.org/10.1101/2021.08.10.455777

Ong, J.Y., Bailey, H.M., Carley, E., Panzica, M., Rixen, M., Billington, N., Liu, R., Quinlan, M.E., n.d. The Influence of Drosophila Spire and Myosin V During Mid-Oogenesis Is Independent of Their Direct Interaction. Cytoskeleton n/a, 1–16. https://doi.org/10.1002/cm.70080

Otto, I.M., Raabe, T., Rennefahrt, U.E., Bork, P., Rapp, U.R., Kerkhog, E., 2000. The p150-Spir protein provides a link between c-Jun N-terminal kinase function and actin reorganization. Curr Biol, Q003 10, 345–8.

Öztürk-Çolak, A., Marygold, S.J., Antonazzo, G., Attrill, H., Goutte-Gattat, D., Jenkins, V.K., Matthews, B.B., Millburn, G., dos Santos, G., Tabone, C.J., FlyBase Consortium, 2024. FlyBase: updates to the Drosophila genes and genomes database. Genetics 227, iyad211. https://doi.org/10.1093/genetics/iyad211

Palese, M., Ferretti, G., Perruolo, G., Serafini, S., Sirabella, R., Marrone, V., De Rosa, M., Sarno, L., Strina, I., Matrone, C., Guida, M., 2024. Semaphorin 3A Increases in the Plasma of Women with Diminished Ovarian Reserve Who Respond Better to Controlled Ovarian Stimulation. Life 14, 358. https://doi.org/10.3390/life14030358

Parton, R.M., Hamilton, R.S., Ball, G., Yang, L., Cullen, C.F., Lu, W., Ohkura, H., Davis, I., 2011. A PAR-1–dependent orientation gradient of dynamic microtubules directs posterior cargo transport in the Drosophila oocyte. J. Cell Biol. 194, 121–135. https://doi.org/10.1083/jcb.201103160

Pfender, S., Kuznetsov, V., Pleiser, S., Kerkhog, E., Schuh, M., 2011. Spire-Type Actin Nucleators Cooperate with Formin-2 to Drive Asymmetric Oocyte Division. Curr. Biol. 21, 955–960. https://doi.org/10.1016/j.cub.2011.04.029

Pruyne, D., 2016. Revisiting the Phylogeny of the Animal Formins: Two New Subtypes, Relationships with Multiple Wing Hairs Proteins, and a Lost Human Formin. PLOS ONE 11, e0164067. https://doi.org/10.1371/journal.pone.0164067

Pylypenko, O., Welz, T., Tittel, J., Kollmar, M., Chardon, F., Malherbe, G., Weiss, S., Michel, C.I.L., Samol-Wolf, A., Grasskamp, A.T., Hume, A., Goud, B., Baron, B., England, P., Titus, M.A., Schwille, P., Weidemann, T., Houdusse, A., Kerkhog, E., 2016.
Coordinated recruitment of Spir actin nucleators and myosin V motors to Rab11 vesicle membranes. eLife 5, e17523. https://doi.org/10.7554/eLife.17523

Quinlan, M.E., 2016. Cytoplasmic Streaming in the Drosophila Oocyte. Annu. Rev. Cell Dev. Biol. 32, 173–195. https://doi.org/10.1146/annurev-cellbio-111315-125416 Quinlan, M.E., 2013. Direct interaction between two actin nucleators is required in Drosophila oogenesis. Development 140, 4417–4425. https://doi.org/10.1242/dev.097337

Quinlan, M.E., Hilgert, S., Bedrossian, A., Mullins, R.D., Kerkhog, E., 2007. Regulatory interactions between two actin nucleators, Spire and Cappuccino. J. Cell Biol. 179, 117–128. https://doi.org/10.1083/jcb.200706196

Roh, S., Yang, D., Jeong, S., 2016. Digerential ligand regulation of PlexB signaling in motor neuron axon guidance in Drosophila. Int. J. Dev. Neurosci. 55, 34–40. https://doi.org/10.1016/j.ijdevneu.2016.09.006

Rosales-Nieves, A.E., Johndrow, J.E., Keller, L.C., Magie, C.R., Pinto-Santini, D.M., Parkhurst, S.M., 2006. Coordination of microtubule and microfilament dynamics by Drosophila Rho1, Spire and Cappuccino. Nat Cell Biol 8, 367–76. https://doi.org/10.1038/ncb1385

Rozbesky, D., Robinson, R.A., Jain, V., Renner, M., Malinauskas, T., Harlos, K., Siebold, C., Jones, E.Y., 2019. Diversity of oligomerization in Drosophila semaphorins suggests a mechanism of functional fine-tuning. Nat. Commun. 10, 3691. https://doi.org/10.1038/s41467-019-11683-y

Schuh, M., 2011. An actin-dependent mechanism for long-range vesicle transport. Nat. Cell Biol. 13, ncb2353. https://doi.org/10.1038/ncb2353

Snee, M.J., Macdonald, P.M., 2009. Dynamic organization and plasticity of sponge bodies. Dev. Dyn. 238, 918–930. https://doi.org/10.1002/dvdy.21914

Stedden, C.G., Menegas, W., Zajac, A.L., Williams, A.M., Cheng, S., Özkan, E., Horne-Badovinac, S., 2019. Planar-Polarized Semaphorin-5c and Plexin A Promote the Collective Migration of Epithelial Cells in Drosophila. Curr. Biol. 29, 908-920.e6. https://doi.org/10.1016/j.cub.2019.01.049

Theurkauf, W.E., 1994. Premature microtubule-dependent cytoplasmic streaming in cappuccino and spire mutant oocytes. Science 265, 2093–6.

Thio, G.L., Ray, R.P., Barcelo, G., Schüpbach, T., 2000. Localization of gurken RNA in Drosophila Oogenesis Requires Elements in the 5′ and 3′ Regions of the Transcript. Dev. Biol. 221, 435–446. https://doi.org/10.1006/dbio.2000.9690

Trovisco, V., Belaya, K., Nashchekin, D., Irion, U., Sirinakis, G., Butler, R., Lee, J.J., Gavis, E.R., Johnston, D.S., 2016. bicoid mRNA localises to the Drosophila oocyte anterior by random Dynein-mediated transport and anchoring. eLife 5, e17537. https://doi.org/10.7554/eLife.17537

Tsanov, N., Samacoits, A., Chouaib, R., Traboulsi, A.-M., Gostan, T., Weber, C., Zimmer, C., Zibara, K., Walter, T., Peter, M., Bertrand, E., Mueller, F., 2016. smiFISH and FISH-quant – a flexible single RNA detection approach with super-resolution capability. Nucleic Acids Res. 44, e165. https://doi.org/10.1093/nar/gkw784

Vizcarra, C.L., Kreutz, B., Rodal, A.A., Toms, A.V., Lu, J., Zheng, W., Quinlan, M.E., Eck, M.J., 2011. Structure and function of the interacting domains of Spire and Fmn-family formins. Proc. Natl. Acad. Sci. 108, 11884–11889. https://doi.org/10.1073/pnas.1105703108

Wellington, A., Emmons, S., James, B., Calley, J., Grover, M., Tolias, P., Manseau, L., 1999. Spire contains actin binding domains and is related to ascidian posterior end mark-5. Development 126, 5267–74.

Winberg, M.L., Mitchell, K.J., Goodman, C.S., 1998. Genetic Analysis of the Mechanisms Controlling Target Selection: Complementary and Combinatorial Functions of Netrins, Semaphorins, and IgCAMs. Cell 93, 581–591. https://doi.org/10.1016/S0092-8674(00)81187-3

Wu, Z., Sweeney, L.B., Ayoob, J.C., Chak, K., Andreone, B.J., Ohyama, T., Kerr, R., Luo, L., Zlatic, M., Kolodkin, A.L., 2011. A Combinatorial Semaphorin Code Instructs the Initial Steps of Sensory Circuit Assembly in the Drosophila CNS. Neuron 70, 281–298. https://doi.org/10.1016/j.neuron.2011.02.050

Ye, B., Petritsch, C., Clark, I.E., Gavis, E.R., Jan, L.Y., Jan, Y.N., 2004. nanos and pumilio Are Essential for Dendrite Morphogenesis in Drosophila Peripheral Neurons. Curr. Biol. 14, 314–321. https://doi.org/10.1016/j.cub.2004.01.052

Yoo, H., Roth-Johnson, E.A., Bor, B., Quinlan, M.E., 2015. Drosophila Cappuccino alleles provide insight into formin mechanism and role in oogenesis. Mol. Biol. Cell 26, 1875–1886. https://doi.org/10.1091/mbc.E14-11-1558

Yu, G., Wang, L.-G., Han, Y., He, Q.-Y., 2012. clusterProfiler: an R Package for Comparing Biological Themes Among Gene Clusters. OMICS J. Integr. Biol. 16, 284–287. https://doi.org/10.1089/omi.2011.0118

Zeth, K., Pechlivanis, M., Samol, A., Pleiser, S., Vonrhein, C., Kerkhog, E., 2011. Molecular basis of actin nucleation factor cooperativity: crystal structure of the Spir-1 kinase non-catalytic C-lobe domain (KIND)•formin-2 formin SPIR interaction motif (FSI) complex. J. Biol. Chem. 286, 30732–30739. https://doi.org/10.1074/jbc.M111.257782

Zhang, H., Dhillon, J., Soloway, P.D., Shui, B., Lee, S., Grenier, J.K., Munn, P.R., Ljungberg, M.C., Williams, R.B., Lanz, R.B., Liao, Y.-H., Ren, Y.A., 2025. Semaphorin 3E-Plexin-D1 Pathway Downstream of the Luteinizing Hormone Surge Regulates Ovulation, Granulosa Cell Luteinization, and Ovarian Angiogenesis in Mice. Adv. Sci. 12, e17163. https://doi.org/10.1002/advs.202417163

Zimyanin, V.L., Belaya, K., Pecreaux, J., Gilchrist, M.J., Clark, A., Davis, I., St Johnston, D., 2008. In Vivo Imaging of oskar mRNA Transport Reveals the Mechanism of Posterior Localization. Cell 134, 843–853. https://doi.org/10.1016/j.cell.2008.06.053

Chapter 3: Investigation of Capu-associated protein candidates

Introduction

Common approaches to identify protein-protein interactions include co-immunoprecipitation (co-IP) and proximity labeling. Co-IP involves the use of an antibody specific to the protein of interest (POI) to pull down the POI along with its interacting partners while proximity labeling uses an engineered enzyme fused to the POI to covalently label proteins in close proximity to the POI. We recently combined co-immunoprecipitation and proximity labeling to determine interactors of Spire (Spir) and Cappuccino (Capu), two actin nucleators that are required to build the actin mesh. Of the Capu-associated candidates that were consistently identified, we focused on Cut-up (Ctp), Homer, and TBC1D23.

Ctp is the *Drosophila* homolog of the LC8 dynein light chain that was first identified as part of large dynein motor complexes (King and Patel-King, 1995). Despite its role as a subunit in dyneins, Ctp has been shown to be expressed across a variety of different cell types and involved in many dynein-independent processes, including transposon silencing, viral transcription, and apoptosis (Eastwood et al., 2021; Singh et al., 2019; Raux et al., 2000). More generally, Ctp serves as a dimerization hub that promotes assembly and structural stabilization by binding to a conserved TQT motif within intrinsically disordered regions (Barbar and Nyarko 2014; Jespersen and Barbar, 2020). Because Capu forms a dimer, Ctp could be interacting with Capu by playing a structural role in facilitating the dimerization (Bor et al., 2012).

Homer proteins have been extensively studied in the central nervous system (CNS), functioning in synaptogenesis, locomotor activity, and sleep (Tao-Cheng et al., 2014; Diagana et al., 2002; Ly et al., 2020). They associate with metabotropic glutamate

receptors (mGluR), filamentous actin (F-actin), and the Rho family of proteins (Shiraishi et al., 1999). In *Drosophila,* Homer, together with Bifocal (Bif), has been shown to be involved in anchoring polarity determinants, such as Oskar (Osk) and Staufen (Stau), to the posterior pole (Babu et al., 2004). Thus, the known roles of Homer and Capu in *osk* localization suggest that it is possible that Capu and Homer interact to mediate this localization in some way.

Furthermore, TBC1D23 is a member of the Rab GTPase activating proteins (GAP) that plays a role in endosome-to-Golgi trafficking (Shin et al., 2017; Johnson and Andrew, 2019). It has been shown to bind to the Wiskott-Aldrich syndrome protein and Scar Homologue (WASH) complex on endosome vesicles. It colocalizes with several Rab GTPases associated with endosomal trafficking, including Rab 5, Rab 9, Rab X1, Rab 8, Rab 10, and Rab 11 (Johnson and Andrew, 2019). Loss of TBC1D23 results in a decrease in fertility, which could be due to defects in border cell migration or *osk* localization related to Rab11 (Johnson and Andrew, 2019; Laflamme et al., 2012; Ramel et al., 2013; Dollar et al., 2002). In mammals, Spir and Fmn-2 (Capu ortholog), colocalize and nucleate actin on Rab11-positive vesicles (Holubcová et al., 2013; Pylypenko et al., 2016). In *Drosophila,* we see Spir and Capu enriched in the migrating border cells (Bailey et al., 2024). Perhaps Spir, Capu, TBC1D23, and Rab11 all play a role in border cell migration.

Here, we investigate the roles of Ctp, Homer, and TBC1D23. We find that Ctp binds to the N-terminal half of Capu (Capu-NT) and makes it a more potent inhibitor of the C-terminal half of Capu (Capu-CT). In *Drosophila,* loss of Ctp leads to changes in *osk* mRNA localization compared to wild-type. Similarly, loss of Homer and TBC1D23 also alters *osk* mRNA localization. In all cases, protein levels of these candidates and Capu

are important for regulation. Together, our findings present several high-confidence Capu-interactors that play a role in *osk* mRNA localization and establish the foundation for future studies to determine the mechanism behind these interactions in *Drosophila* oogenesis.

Results

osk mRNA localization is disrupted in ctp, homer, and TBC1D23 mutants

Because the actin mesh is important for properly localizing polarity determinants, we performed initial candidate-based screens probing for *osk* mRNA localization in *ctp*, *TBC1D23*, and *homer* mutants. We used loss-of-function alleles for all of these proteins (*ctp*^{G0371}, *TBC1D23*$^{CR00980\text{-}TG4.2}$, and *homer*^{R102}) and crossed them either to *capu*^{HK3} mutants or a deficiency fly line to generate mutant trans-heterozygotes or hypomorphs/nulls, respectively. We were unable to generate *ctp* hypomorphs because Ctp is essential for many processes, both dynein-dependent and independent processes. However, *ctp*^{G0371}/+ heterozygotes exhibited clumpy spots of *osk* mRNA similar to what was seen for Sema2a mutants in stages 7/8 egg chambers (55%, n=11) (**Figures 3-1C-C'',V, Chapter 2**), and there was also one clump of *osk* near the posterior of the oocyte compared to wild-type in stage 9 (83%, n=12) (**Figures 3-1B-B', D-D', W**). In addition, the majority of clumpy spots in both stages 7/8 and 9 were suppressed in *ctp*^{G0371}/*capu*^{HK3} trans-heterozygotes, suggesting that Ctp and Capu levels are important for proper localization of *osk* mRNA (**Figures 3-1E-F', V-W**).

Similarly, *TBC1D23*$^{CR00980\text{-}TG4.2}$/*capu*^{HK3} trans-heterozygotes did not contain any of the single spots of *osk* mRNA that were seen in *TBC1D23*$^{CR00980\text{-}TG4.2}$/+ heterozygotes

(**Figures 3-1G-G'', M-M'', V**). However, *TBC1D23* hypomorphs (*TBC1D23*$^{CR00980\text{-}TG4.2}$/Df) had a greater percentage of a single cluster of *osk* (62.5%, n=16) compared to *TBC1D23*$^{CR00980\text{-}TG4.2}$/+ heterozygotes (29%, n=7) (**Figures 3-1G-G'', K-K'', and V**). Intriguingly, there were a couple of instances where *TBC1D23* hypomorphs contained conjoined egg chambers (**Figure 3-1K-K''**). Furthermore, *homer* mutants all consisted of clumpy spots in stages 7/8 oocytes, with *homer*-nulls (homozygous *homer*^{R102}) containing mostly clumpy spots (88%, n=17) (**Figures 3-1N-N'', P-P'', R-R'', V**) while *homer*^{R102}/*capu*^{HK3} trans-heterozygotes suppressed the clumpy spots and instead contained mostly one single cluster of *osk* (**Figures 3-1T-T'', V**). Together, these data suggest that Ctp, TBC1D23, and Homer all play a role in *osk* mRNA localization and the levels of these proteins relative to Capu are important.

Ctp binds to Capu-NT

Both the proteomics data and initial candidate-based screens suggested that the aforementioned proteins are real Capu interactors. We focused specifically on Ctp, which was also found in TAP-tagged Capu proteomic datasets (data not shown). It was also found in Spir co-IPs but was not statistically significant (Chapter 2). Ctp has been shown to be involved in many dynein-independent processes by functioning as a dimerization hub that binds to a specific TQT sequence (Barbar and Nyarko 2014; Jespersen and Barbar, 2020). Using LC8Pred, we found that Capu contains the motif sequence TDAETQTE at a disordered region before the FH1 domain at anchor position 448 (Jespersen et al., 2019). Thus, we performed fluorescence anisotropy experiments with purified recombinant Ctp, the C-terminal half of Capu (Capu-CT, amino acids 467-1059),

and the N-terminal half of Capu (Capu-NT, amino acids 1-466), which contains the putative Ctp binding site. In these anisotropy experiments with or without the addition of BSA, Ctp binds to Capu-NT and not Capu-CT, as indicated by the increase in anisotropy with increasing concentrations of Capu-NT (**Figures 3-2A-B**). Moreover, cross-linking mass spectrometry (XL-MS) experiments with Ctp and Capu-NT also confirm binding and can inform on the 3D structure (**Figure 3-2C**).

To determine how Ctp might be regulating Capu, we tested these proteins in a pyrene-actin polymerization assay. Consistent with a previous study, addition of Capu-NT inhibits the actin assembly activity of Capu-CT in a dose-dependent manner (**Figure 3-2D**) (Bor et al., 2012). Addition of Ctp to a low concentration of Capu-NT inhibits Capu-CT mediated actin assembly more than Capu-NT alone, suggesting that Ctp is making Capu-NT a more potent inhibitor of Capu-CT (**Figure 3-2D**). Taken together, Ctp binds to Capu-NT to inhibit Capu-CT, which could have implications *in vivo.*

Discussion

The candidate-based screens showed similar clumpy spots of *osk* mRNA, suggesting that these proteins all play a role in the localization and transport of *osk.* It was interesting that the majority of ctp^{G0371}/+ heterozygotes contained one spot of *osk* mRNA close to the posterior of the oocyte, but this phenotype was suppressed in Ctp-Capu trans-heterozygote mutants. The same result of phenotype suppression was also seen in Homer- and TBC1D23-Capu trans-heterozygote mutants, indicating the levels of all these proteins and Capu are important for proper localization of *osk* mRNA. However, further investigations are needed to understand how exactly all these proteins interact

with Capu to influence this mislocalization and what other processes these proteins might be involved in, as the Sema2a-Capu interaction suggested that Capu plays other roles beyond the actin mesh, particularly in processes related to the migrating border cells and sponge bodies (**Chapter 2**). Whether all these proteins function together or form alternating complexes would be interesting, as Sema2a and Ctp are both shown to inhibit Capu.

In addition, investigating the Ctp-Capu interaction by mutating the TQT motif in Capu would provide insight into the putative binding site and allow us to test how abolishing the Ctp-Capu interaction might affect Capu activity *in vitro* and *in vivo*. As Ctp was also found to be enriched in Spir co-IPs, it would also be intriguing if Ctp also affects Spir binding and its role in oogenesis. Deeper investigation into other processes that Capu and these candidates are involved in will ultimately provide more insight into Capu's role in oogenesis that extends beyond the actin mesh.

Methods

Drosophila stocks

The following fly lines were obtained from Bloomington Drosophila Stock Center: w^{1118}, ctp^{G0371}/FM7c (RRID:BDSC_11988, (Peter et al., 2002)), Df(1)ED6727/FM7h (RRID:BDSC_8956, (Ryder et al., 2007)), TBC1D23[CR00980-TG4.2]/SM6a (RRID:BDSC_83232, (Lee et al., 2018)), Df(2L)Exel6004 (RRID:BDSC_7491, (Parks et al., 2004)), $homer^{R102}$ (RRID:BDSC_9564, (Diagana et al., 2002)), Df(2L)Exel7027 (RRID:BDSC_7801, (Parks et al., 2004)).

Microscropy, smiFISH, and mass spectrometry preparation were all performed as described in Chapter 2.

Protein expression and purification

Acanthamoeba castellani actin, Capu-CT, and Capu-NT constructs were expressed and purified using published protocols seen in Chapter 2.

KCK-ctp::pGEX-6P-2 was expressed in Rosetta competent cells and grown in Terrific Broth at 37°C until they reached an OD_{600} of 0.6. Cells were induced with 0.25 mM isopropyl-β-d-thiogalactoside at 18°C overnight. The resulting cell pellets were flash frozen with liquid nitrogen and stored at -80°C.

Purification of KCK-ctp was performed using glutathione agarose resin and the protein was cleaved from GST using PreScission Protease overnight at 4°C. Then, proteins were dialyzed in 20 mM HEPES pH 7.0 and run on the MonoS cation exchange column. Purified fractions were dialyzed into storage buffer (10 mM Tris pH 8.0, 50 mM NaCl, 1 mM DTT, 20% glycerol). Aliquots were flash frozen with liquid nitrogen and stored at -80°C.

For labeling, KCK-ctp was incubated with C5-Maleimide-Alexafluor488 overnight in HEPES buffer right after running MonoS. Reaction was quenched with 10 mM DTT. Purified fractions were dialyzed into storage buffer (10 mM Tris pH 8.0, 50 mM NaCl, 1 mM DTT, 20% glycerol). Aliquots were flash frozen with liquid nitrogen and stored at -80°C.

Fluorescence anisotropy

Serial dilutions from 0-1 μM Capu-NT were added to a solution of 10 nM KCK-ctp-AlexaFluor488 in 1X KMEH (10 mM HEPES, pH 7.5, 1 mM EGTA, 1 mM $MgCl_2$, 50 mM KCl, and 0.2 mM ATP) and incubated for 20-30 min in the dark. 90 μL of each solution was added to a Corning 384-well microplate and fluorescence polarization was measured (with excitation at 485 and emission at 535) in an Infinite Pro 200 plate reader (Tecan). The follow parameters were used: 5 cycles, 25 flashes, 20 μs integration time, 25 ms settle time, and a calibrated G-factor of 1.245.

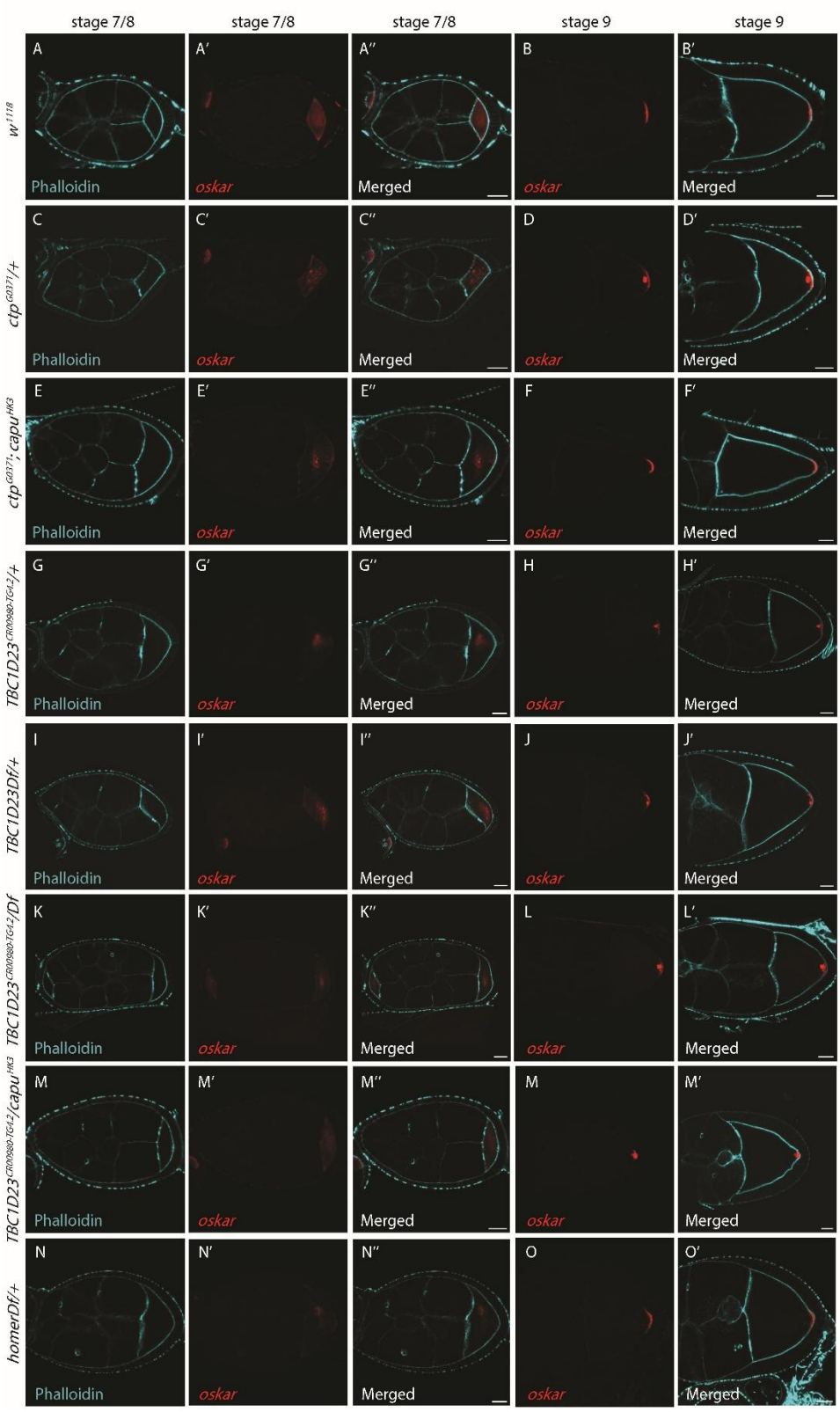
stage 7/8
stage 7/8
stage 7/8
stage 9
stage 9
w1118
ctpGD371/+
ctpGD371; capuHK3
TBC1D23CRIM9880-TG4.2/+
TBC1D23Df/+
TBC1D23CRIM9880-TG4.2/Df
TBC1D23CRIM9880-TG4.2/capuHK3
homerDf/+
A
A′
A″
B
B′
C
C′
C″
D
D′
E
E′
E″
F
F′
G
G′
G″
H
H′
I
I′
I″
J
J′
K
K′
K″
L
L′
M
M′
M″
M
M′
N
N′
N″
O
O′
Phalloidin
oskar
Merged

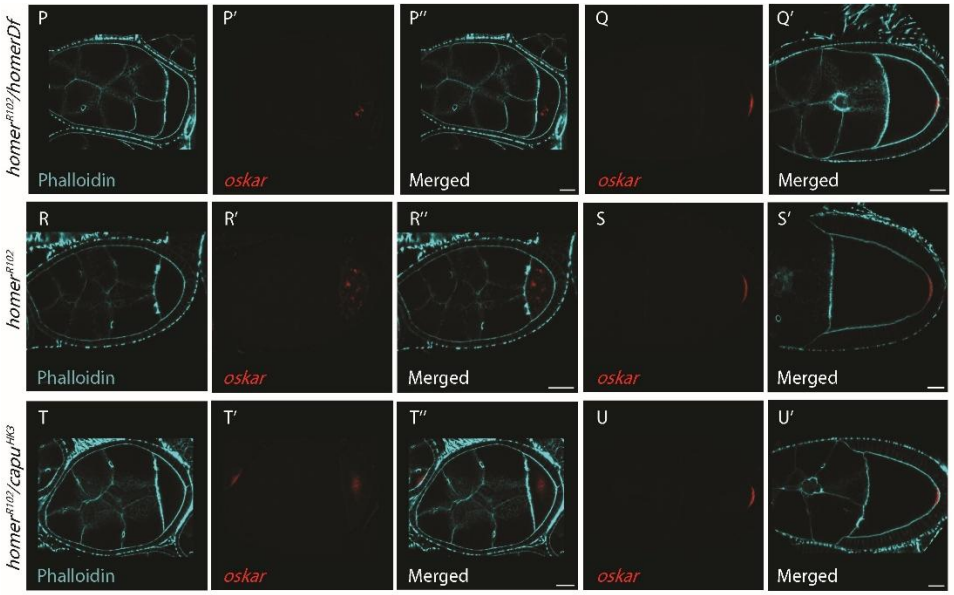
homer^R102/homerDf
P
P′
P″
Q
Q′
Phalloidin
oskar
Merged
homer^R102
R
R′
R″
S
S′
homer^R102/capu^HK3
T
T′
T″
U
U′

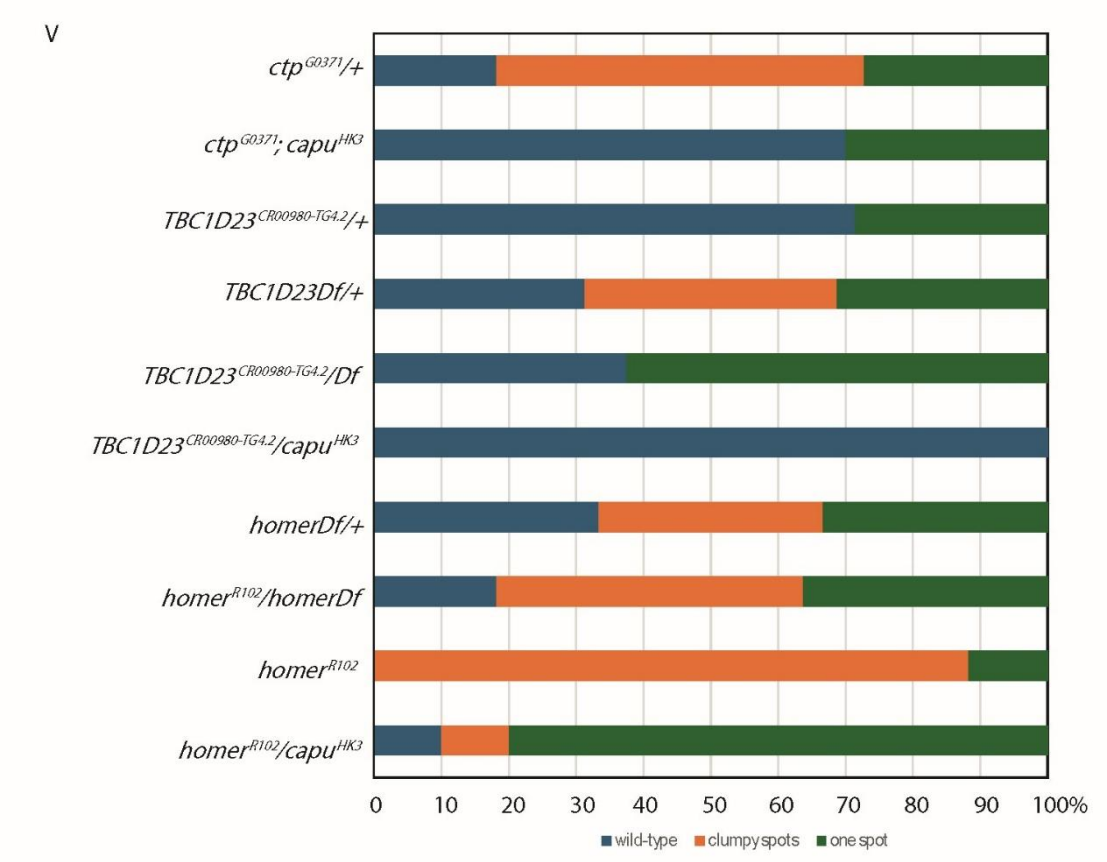
V
ctp^G0371/+
ctp^G0371; capu^HK3
TBC1D23^CR00980-TG4.2/+
TBC1D23Df/+
TBC1D23^CR00980-TG4.2/Df
TBC1D23^CR00980-TG4.2/capu^HK3
homerDf/+
homer^R102/homerDf
homer^R102
homer^R102/capu^HK3
0
10
20
30
40
50
60
70
80
90
100%
wild-type
clumpy spots
one spot

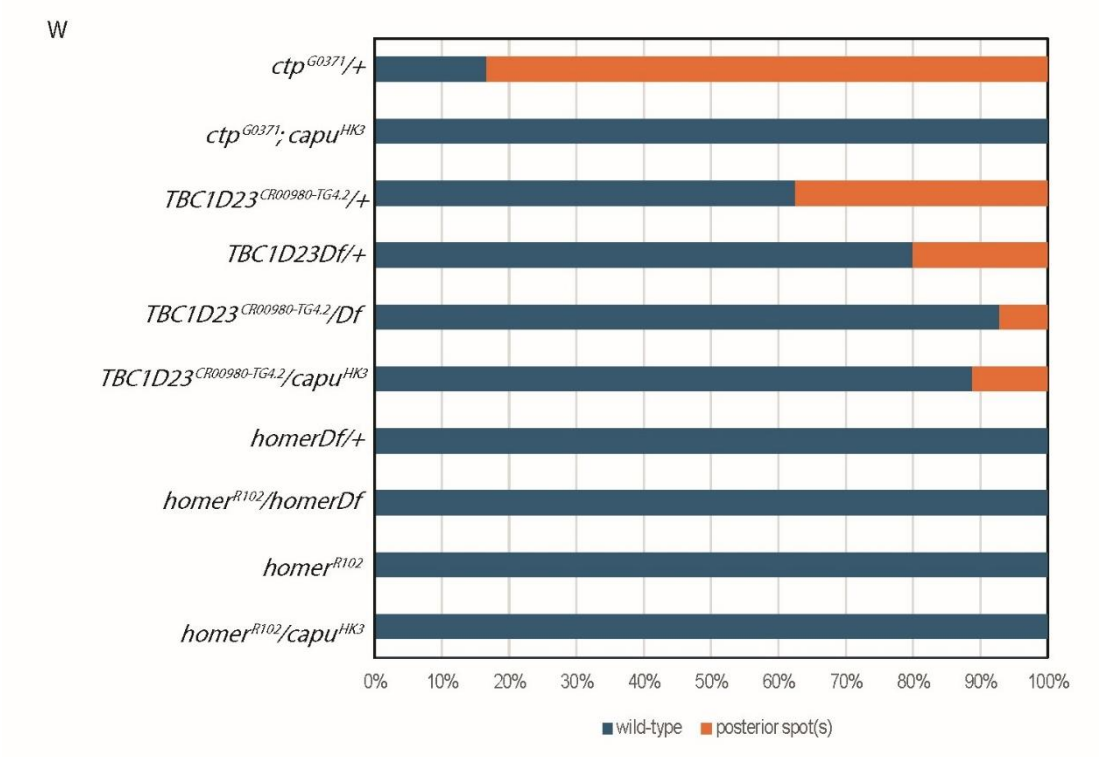

Figure 3-1. osk mRNA is altered in ctp, homer, and TBC1D23 mutants. Stage 7 or 9 egg chambers stained with phalloidin and *osk* mRNA probe, (A-B') w^{1118}, (C-D') ctp^{G0371}/+, (E-F') ctp^{G0371}/+; $capu^{HK3}$/+, (G-H') $TBC1D23^{CR00980\text{-}TG4.2}$/+, (I-J') *TBC1D23Df/+,* (K-L') $TBC1D23^{CR00980\text{-}TG4.2}$*/Df,* (M-M') $TBC1D23^{CR00980\text{-}TG4.2}$/ $capu^{HK3}$, (N-O') *homerDf/+,* (P-Q') $homer^{R102}$*/homerDf,* (R-S') $homer^{R102}$, (T-U') $homer^{R102}$/ $capu^{HK3}$*.* Ctp, homer, and TBC1D23 mutants exhibit clumpy spots or one central cluster but this phenotype is relieved in trans-heterozygotes. Scale bars are 20 μm. (W) Quantification of different phenotypes for stage 7 egg chambers for ctp^{G0371}/+ (n=11), ctp^{G0371}/+; $capu^{HK3}$/+ (n=10), $TBC1D23^{CR00980\text{-}TG4.2}$/+ (n=7), *TBC1D23Df/+* (n=16), $TBC1D23^{CR00980\text{-}TG4.2}$*/Df* (n=16), $TBC1D23^{CR00980\text{-}TG4.2}$/ $capu^{HK3}$ (n=6), *homerDf/+* (n=15), $homer^{R102}$*/homerDf* (n=11), $homer^{R102}$ (n=17), $homer^{R102}$/ $capu^{HK3}$ (n=10). (V) Quantification of different phenotypes for stage 9 egg chambers for ctp^{G0371}/+ (n=12), ctp^{G0371}/+; $capu^{HK3}$/+ (n=7), $TBC1D23^{CR00980\text{-}TG4.2}$/+ (n=16), *TBC1D23Df/+* (n=5), $TBC1D23^{CR00980\text{-}TG4.2}$*/Df* (n=14), $TBC1D23^{CR00980\text{-}TG4.2}$/ $capu^{HK3}$ (n=18), *homerDf/+* (n=5), $homer^{R102}$*/homerDf* (n=8), $homer^{R102}$ (n=6), $homer^{R102}$/ $capu^{HK3}$ (n=14).

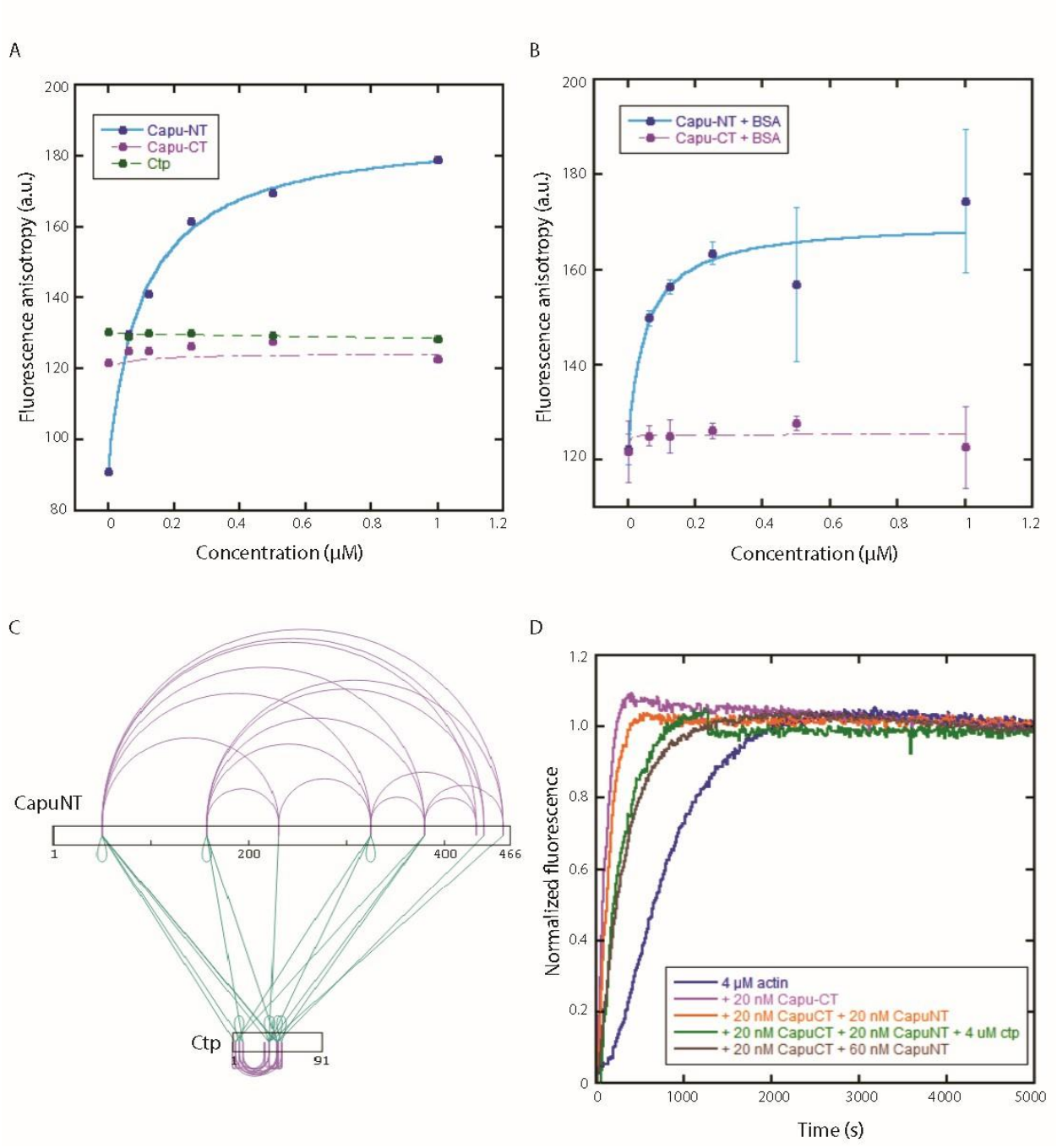

Figure 3-2. Ctp binds to Capu-NT and increases the inhibition activity of Capu-NT. (A) Fluorescence anisotropy of increasing concentrations of Capu-NT and Capu-CT with 10 nM KCK-ctp-AlexaFluor488 and KCK-ctp-AlexaFluor488 alone. (B) Fluorescence anisotropy of increasing concentrations of Capu-NT and Capu-CT with 10 nM KCK-ctp-AlexaFluor488. BSA was added to prevent non-specific binding to wells. (C) Cross-linking mass spectrometry with Capu-NT and Ctp. (D) Pyrene-actin polymerization assays showing that Ctp makes Capu-NT a more potent inhibitor.

References

Babu, K., Cai, Y., Bahri, S., Yang, X., & Chia, W. (2004). Roles of Bifocal, Homer, and F-actin in anchoring Oskar to the posterior cortex of Drosophila oocytes. *Genes & development*, *18*, 138–143.

Bailey, H.M., Cullimore, P.B.M., Bailey, L.A., Quinlan, M.E., 2024. Localization of Drosophila formin, Cappuccino, influences posterior oocyte organization.

Barbar, E., & Nyarko, A. (2014). NMR Characterization of Self-Association Domains Promoted by Interactions with LC8 Hub Protein. *Computational and structural biotechnology journal*, *9*, e201402003.

Bor, B., Vizcarra, C. L., Phillips, M. L., & Quinlan, M. E. (2012). Autoinhibition of the formin Cappuccino in the absence of canonical autoinhibitory domains. *Molecular biology of the cell*, 23, 3801–3813.

Diagana, T. T., Thomas, U., Prokopenko, S. N., Xiao, B., Worley, P. F., & Thomas, J. B. (2002). Mutation of Drosophila homer disrupts control of locomotor activity and behavioral plasticity. *The Journal of neuroscience : the official journal of the Society for Neuroscience*, *22*, 428–436.

Dollar, G., Struckhoff, E., Michaud, J., & Cohen, R. S. (2002). Rab11 polarization of the Drosophila oocyte: a novel link between membrane trafficking, microtubule organization, and oskar mRNA localization and translation. *Development (Cambridge, England)*, *129*(2), 517–526.

Eastwood, E. L., Jara, K. A., Bornelöv, S., Munafò, M., Frantzis, V., Kneuss, E., Barbar, E. J., Czech, B., & Hannon, G. J. (2021). Dimerisation of the PICTS complex via LC8/Cut-up drives co-transcriptional transposon silencing in *Drosophila*. *eLife*, *10*, e65557.

Holubcová, Z., Howard, G., & Schuh, M. (2013). Vesicles modulate an actin network for asymmetric spindle positioning. *Nature cell biology*, *15*(8), 937–947.

Jespersen, N., & Barbar, E. (2020). Emerging Features of Linear Motif-Binding Hub Proteins. *Trends in biochemical sciences*, *45*, 375–384.

Jespersen, N., Estelle, A., Waugh, N., Davey, N. E., Blikstad, C., Ammon, Y. C., Akhmanova, A., Ivarsson, Y., Hendrix, D. A., & Barbar, E. (2019). Systematic identification of recognition motifs for the hub protein LC8. *Life science alliance*, *2*(4), e201900366.

Johnson, D. M., & Andrew, D. J. (2019). Role of tbc1 in Drosophila embryonic salivary glands. *BMC molecular and cell biology*, *20*, 19.

King, S. M., & Patel-King, R. S. (1995). The M(r) = 8,000 and 11,000 outer arm dynein light chains from Chlamydomonas flagella have cytoplasmic homologues. *The Journal of biological chemistry*, *270*, 11445–11452.

Laflamme, C., Assaker, G., Ramel, D., Dorn, J. F., She, D., Maddox, P. S., & Emery, G. (2012). Evi5 promotes collective cell migration through its Rab-GAP activity. *The Journal of cell biology*, *198*, 57–67.

Lee, P. T., Zirin, J., Kanca, O., Lin, W. W., Schulze, K. L., Li-Kroeger, D., Tao, R., Devereaux, C., Hu, Y., Chung, V., Fang, Y., He, Y., Pan, H., Ge, M., Zuo, Z., Housden, B. E., Mohr, S. E., Yamamoto, S., Levis, R. W., Spradling, A. C., … Bellen, H. J. (2018). A gene-specific *T2A-GAL4* library for *Drosophila*. *eLife*, *7*, e35574.

Ly, S., Strus, E., & Naidoo, N. (2020). Genetic disruption of the putative binding site for Homer on DmGluRA reduces sleep in Drosophila. *Sleep*, *43*, zsz190.

Parks, A. L., Cook, K. R., Belvin, M., Dompe, N. A., Fawcett, R., Huppert, K., Tan, L. R., Winter, C. G., Bogart, K. P., Deal, J. E., Deal-Herr, M. E., Grant, D., Marcinko, M., Miyazaki, W. Y., Robertson, S., Shaw, K. J., Tabios, M., Vysotskaia, V., Zhao, L., Andrade, R. S., … Francis-Lang, H. L. (2004). Systematic generation of high-resolution deletion coverage of the Drosophila melanogaster genome. *Nature genetics*, *36*(3), 288–292

Peter, A., Schöttler, P., Werner, M., Beinert, N., Dowe, G., Burkert, P., Mourkioti, F., Dentzer, L., He, Y., Deak, P., Benos, P. V., Gatt, M. K., Murphy, L., Harris, D., Barrell, B., Ferraz, C., Vidal, S., Brun, C., Demaille, J., Cadieu, E., … Schäfer, U. (2002). Mapping and identification of essential gene functions on the X chromosome of Drosophila. *EMBO reports*, *3*(1), 34–38.

Pylypenko, O., Welz, T., Tittel, J., Kollmar, M., Chardon, F., Malherbe, G., Weiss, S., Michel, C. I., Samol-Wolf, A., Grasskamp, A. T., Hume, A., Goud, B., Baron, B., England, P., Titus, M. A., Schwille, P., Weidemann, T., Houdusse, A., & Kerkhoff, E. (2016). Coordinated recruitment of Spir actin nucleators and myosin V motors to Rab11 vesicle membranes. *eLife*, *5*, e17523.

Ramel, D., Wang, X., Laflamme, C., Montell, D. J., & Emery, G. (2013). Rab11 regulates cell-cell communication during collective cell movements. *Nature cell biology*, *15*, 317–324.

Raux, H., Flamand, A., & Blondel, D. (2000). Interaction of the rabies virus P protein with the LC8 dynein light chain. *Journal of virology*, *74*, 10212–10216.

Shin, J. J. H., Gillingham, A. K., Begum, F., Chadwick, J., & Munro, S. (2017). TBC1D23 is a bridging factor for endosomal vesicle capture by golgins at the trans-Golgi. *Nature cell biology*, *19*, 1424–1432.

Ryder, E., Ashburner, M., Bautista-Llacer, R., Drummond, J., Webster, J., Johnson, G., Morley, T., Chan, Y. S., Blows, F., Coulson, D., Reuter, G., Baisch, H., Apelt, C., Kauk, A., Rudolph, T., Kube, M., Klimm, M., Nickel, C., Szidonya, J., Maróy, P., … Russell, S. (2007). The DrosDel deletion collection: a Drosophila genomewide chromosomal deficiency resource. *Genetics*, *177*(1), 615–629.

Shiraishi, Y., Mizutani, A., Bito, H., Fujisawa, K., Narumiya, S., Mikoshiba, K., & Furuichi, T. (1999). Cupidin, an isoform of Homer/Vesl, interacts with the actin cytoskeleton and activated rho family small GTPases and is expressed in developing mouse cerebellar granule cells. *The Journal of neuroscience : the official journal of the Society for Neuroscience*, *19*, 8389–8400.

Singh, P. K., Roukounakis, A., Weber, A., Das, K. K., Sohm, B., Villunger, A., Garcia-Saez, A. J., & Häcker, G. (2020). Dynein light chain binding determines complex formation and posttranslational stability of the Bcl-2 family members Bmf and Bim. *Cell death and differentiation*, *27*, 434–450.

Tao-Cheng, J. H., Thein, S., Yang, Y., Reese, T. S., & Gallant, P. E. (2014). Homer is concentrated at the postsynaptic density and does not redistribute after acute synaptic stimulation. *Neuroscience*, *266*, 80–90.

Chapter 4: Formin tails act as a switch, inhibiting or enhancing processive actin elongation

JBC RESEARCH ARTICLE

Formin tails act as a switch, inhibiting or enhancing processive actin elongation

Received for publication, September 1, 2023, and in revised form, November 30, 2023 Published, Papers in Press, December 12, 2023,
https://doi.org/10.1016/j.jbc.2023.105557

Kathryn V. Bremer[1], Carolyn Wu[1], Aanand A. Patel[1], Kevin L. He[1], Alex M. Grunfeld[1], Guillaume F. Chanfreau[1,2], and Margot E. Quinlan[1,2,*]

From the [1]Department of Chemistry and Biochemistry, and [2]Molecular Biology Institute, University of California Los Angeles, Los Angeles, California, USA

Reviewed by members of the JBC Editorial Board. Edited by Enrique De La Cruz

Formins are large, multidomain proteins that nucleate new actin filaments and accelerate elongation through a processive interaction with the barbed ends of filaments. Their actin assembly activity is generally attributed to their eponymous formin homology (FH) 1 and 2 domains; however, evidence is mounting that regions outside of the FH1FH2 stretch also tune actin assembly. Here, we explore the underlying contributions of the tail domain, which spans the sequence between the FH2 domain and the C terminus of formins. Tails vary in length from ~0 to >200 residues and contain a number of recognizable motifs. The most common and well-studied motif is the ~15-residue-long diaphanous autoregulatory domain. This domain mediates all or nothing regulation of actin assembly through an intramolecular interaction with the diaphanous inhibitory domain in the N-terminal half of the protein. Multiple reports demonstrate that the tail can enhance both nucleation and processivity. In this study, we provide a high-resolution view of the alternative splicing encompassing the tail in the formin homology domain (Fhod) family of formins during development. While four distinct tails are predicted, we found significant levels of only two of these. We characterized the biochemical effects of the different tails. Surprisingly, the two highly expressed Fhod-tails inhibit processive elongation and diminish nucleation, while a third supports activity. These findings demonstrate a new mechanism of modulating actin assembly by formins and support a model in which splice variants are specialized to build distinct actin structures during development.

Formins are a highly conserved family of proteins that nucleate actin and modify filament growth by remaining processively associated with the fast-growing barbed end of actin filaments (1–4). They are defined by their homodimeric formin homology (FH)-2 domains and proline-rich FH1 domains. The FH2 domain dimerizes to form a donut-shaped structure that is sufficient for nucleation and processive binding at the barbed end of elongating filaments (5–7). The proline-rich FH1 domain recruits profilin-bound actin monomers and delivers them to the FH2-bound barbed end, accelerating the actin assembly rate (8, 9). In addition to the FH1/2 domains, most formins contain a loosely defined tail domain between the FH2 domain and the C terminus. The tail often contains a diaphanous autoregulatory domain (DAD), which binds to an N-terminal diaphanous inhibitory domain to inhibit formin activity (10, 11). The tail also contributes to nucleation and elongation (12, 13).

The tail length varies greatly across formins, ranging from absent to >200 residues. By testing several truncations of the formin Cappuccino (Capu) and chimeras of tails from various formins added to the Capu-FH1FH2 domains, we previously showed that the tail strongly influences processivity but not the elongation rate (13). The dissociation rate of Capu from the barbed end was over two orders of magnitude higher when the ~30-residue tail of Capu was deleted. Processivity could also be improved by replacing the Capu-tail with tails from the highly processive formins, mDia1 and mDia2. The dissociation rate loosely correlated with the pI of the tail. Strikingly, close to wildtype processivity was recovered when we scrambled the order of the Capu-tail residues. These observations led to a model in which the tail domain makes nonspecific electrostatic contacts with the sides of growing filaments to enhance processivity, consistent with the idea that the pI may be a useful predictor of processivity.

The *Drosophila melanogaster* formin homology 2 domain family protein, referred to here as Fhod (the gene name is annotated as *fhos* or *knittrig* (14)), plays many roles in development, including myofibril assembly, tracheal development, and programmed autophagic cell death in salivary glands (15–17). In adults, Fhod plays a maintenance role in muscle cells and contributes to macrophage motility and the immune response (15, 16, 18). Fhod is alternatively spliced to produce as many as nine isoforms that differ by their N termini and their tails, but all contain identical FH1 and FH2 domains (14). Functional analysis demonstrates critical roles for at least two different N termini (15, 16). However, there is no known role for the four Fhod tails that are generated by alternative splicing. We previously reported that the C-terminal half of one of these Fhod isoforms, Fhod-A, nucleates actin filaments and binds barbed ends but is only weakly processive (19). To better understand the role of Fhod and the role of the formin

* For correspondence: Margot E. Quinlan, margot@chem.ucla.edu.
Present address for Aanand A. Patel: Department of Laboratory Medicine and Pathology, University of Washington, 1959 Northeast Pacific Street, Seattle, WA 98195, USA.

tail in actin assembly, we exploited the natural variation of Fhod transcripts, comparing actin assembly activities of Fhod-FH1FH2 with different tails. Interestingly, we found that a shorter tail (Fhod-B) supports processivity. In contrast to what we previously observed for Capu, we found that longer Fhod tails suppress processivity and decrease nucleation. Nucleation correlates with tail length in Fhod, whereas processivity is impaired by a specific cluster of nine residues. Thus, formin tails can be highly specialized and, even within a single gene, confer distinct actin assembly properties.

Results

Oxford Nanopore sequencing provides a high-resolution view of Fhod variants expressed differentially during fly development

The *Drosophila* formin Fhod provides a powerful model to study contributions to actin assembly by the domains outside of the FH1 and FH2 domains. Only one *fhos* gene, which encodes the protein Fhod, is found in the fly genome, but alternative splicing results in at least nine predicted protein products, which vary by their N termini and C-terminal tails while retaining identical FH1 and FH2 domains (Fig. 1*A*).

We focused on the *fhos* isoforms that differ by their tails and asked which of the variants are expressed as a function of development. Note that there are two groups of isoforms that each share a common tail. For simplicity, we refer to the tail shared by isoforms A, G, H, I, and J as the Fhod-A tail and the tail shared by isoforms E and F as the Fhod-E tail (Fig. 1, *A* and *B*). The Fhod-B and Fhod-D tails are not shared by other isoforms.

To study expression patterns, we isolated total RNA from whole larvae, pupae, and at days 1, 3, and 5 post eclosion. We enriched these samples for Fhod, from the FH2 domain to the poly-A tail, using end-point RT-PCR (primer sequences are included in Experimental procedures). We then used

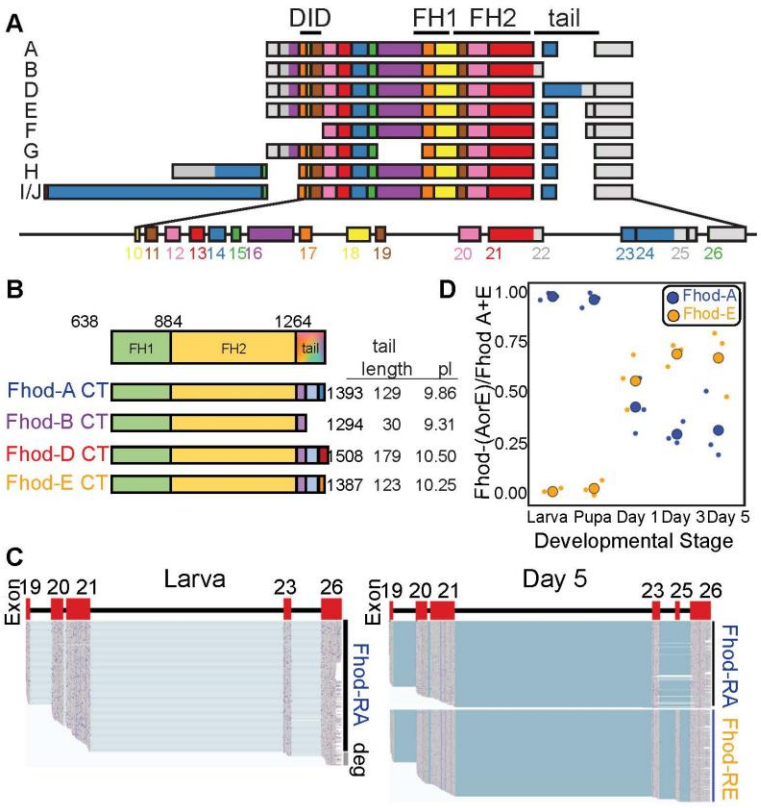

Figure 1. Fhod variants with distinct tails are differentially expressed during development. *A*, alternative splicing of *fhos* leads to nine putative protein variants. *B*, four distinct tails are possible (*A*, *B*, *D*, and *E*). They have the same Formin homology-1 (FH1) and FH2 domains. FH1 green; FH2 yellow; within the tail, colors represent exons. The tails vary in length and theoretical pI as shown. *C*, Oxford Nanopore sequencing—samples of reads mapped to the *fhos* gene for the larval stage and day 5. Data from all five stages are shown in Supporting information (Fig. S1). *D*, ratio of reads of Fhod-A (*blue*) relative to reads of Fhod-E (*yellow*) for each developmental stage. Plot generated using SuperPlotsOfData (30). *Small circles* represent reads from independent samples. The *large circles* are means (n = 3 in all cases). Fhod-A is present at all stages while Fhod-E is not detected in larva and pupa but read numbers increase with age post eclosion. DID, diaphanous inhibitory domain.

Nanopore amplicon sequencing to determine which isoforms were expressed at different developmental stages. We detected Fhod-A in all developmental stages tested, while the Fhod-E tail was only observed in eclosed flies (Fig. 1, *C* and *D*). Data from all five developmental stages are shown in Supporting information (Fig. S1). While Fhod-A levels decrease relative to Fhod-E, it is still highly expressed in adult flies as shown by the abundance of Fhod-A reads. Fhod-B and Fhod-D were not detected using this approach, suggesting that Fhod-B and Fhod-D may not be expressed or, if they are, they are possibly expressed in specific tissues and at levels too low to be detected in samples from whole animals.

Interestingly, we detected an extended species of exon 19, which terminated within the following intron (Fig. S2*A*). The FH2 domain spans exons 19, 20, and 21. This species would encode only a small portion of the FH2 domain. An additional species accumulated in adult flies that terminated at exon 21, which could be Fhod-B; however, it does not contain the distinct Fhod-B 3′UTR (Fig. S2*B*), which we did detect a few times. To our knowledge, neither of these transcripts has been previously reported.

In conclusion, the Nanopore sequencing data provided a high-resolution picture of the expression of the different Fhod isoforms during development. Because of their distinct developmental expression patterns and apparently high levels of expression, we chose to focus on Fhod-A and Fhod-E. We included Fhod-B in our biochemical analysis because, when translated, it is effectively a truncation of the other three tails.

Fhod-B is a processive elongation factor

In order to characterize the biochemical properties of the different Fhod tails, we purified the C-terminal halves of the two most highly expressed isoforms (A and E), which include their common FH1 and FH2 domains and their distinct C-terminal tails (Fig. 1*B*). The tails of isoforms A, B, and E share the same first 30 residues. Fhod-B terminates at this point, whereas Fhod-A and Fhod-E have longer tails, consisting of 75 residues that are shared between the two followed by a short sequence unique to each (24 residues long for Fhod-A and 18 residues long for Fhod-E; Fig. 1*B*). Using total internal reflection fluorescence (TIRF) microscopy, we did not detect obvious differences in elongation rate or fluorescence intensity when actin filaments were grown in the presence of 0.5 nM Fhod-A or Fhod-E and profilin, compared with profilin–actin alone (Fig. 2*A*). (Formin-bound filaments usually appear dimmer because the FH1 domains recruit profilin-bound actin and profilin has a weaker affinity for actin that is fluorescently labeled on cysteine 374 (8).) In fact, filaments do grow slightly but significantly faster in the presence of Fhod-A (7.4 ± 0.9 [n = 9] *versus* 5.5 ± 1.0 [n = 16] subunits/sec, mean ± SD, $p < 0.05$; description and details regarding statistical analysis are given in Experimental procedures and Supporting information; Fig. 2, *A*–*C*). The data suggest that these isoforms have very short run lengths. This conclusion is also consistent with our previous study of Fhod-A, in which we indirectly measured a characteristic run length of ∼2 μm, which is too short to reliably detect in typical TIRF microscopy assays (19). Owing to their short run lengths, we could not determine whether Fhod-E or how much Fhod-A alters the elongation rate when bound to barbed ends.

In contrast to Fhod-A and Fhod-E, actin assembly in the presence of 0.5 nM Fhod-B and profilin resulted in bright and dim filaments, where the dim filaments grew ∼4-fold faster than their bright counterparts (17 ± 3 [n = 10] *versus* 4 ± 1 [n = 6] subunits/sec, mean ± SD, $p < 10^{-8}$; Fig. 2, *A*–*C*). We thus conclude that Fhod-B remains processively associated with the barbed end of filaments and accelerates elongation. We estimated the characteristic run length of Fhod-B by measuring the length distribution of actin filaments in this elongation assay after 5 min (Fig. 2*D*). The distribution of (dim) filament lengths indicates a median run length of 24 μm (n = 66). The data are not well fit by an exponential, in part because we cannot detect the shortest filaments. However, we expect that this value is an underestimate of the characteristic run length because we were unable to measure filaments longer than 50 μm or that grow for longer than 5 min.

Thus, we have identified a *Drosophila* Fhod isoform, Fhod-B, which elongates filaments with at least 10-fold increased processivity compared with the previously characterized isoform Fhod-A and the newly characterized isoform Fhod-E. The amino acid sequences of these isoforms only differ within their tail region, where Fhod-B possesses the shortest tail. Therefore, our data show that there is nothing inherent to Fhod-FH1FH2 that prevents processive elongation. Instead, the data indicate that Fhod processivity switches depending on its tail and that processivity is markedly decreased or even inhibited by certain tails.

Residues near the end of the Fhod-A tail inhibit processivity

We sought to determine the basis of processivity loss, given that Fhod-A and Fhod-E include the sequence of Fhod-B. To do so, we first asked whether each tail adopts any secondary structure using circular dichroism (CD) spectroscopy. The spectra for all three isoforms were consistent with random coil, leading us to conclude that all three tails lack secondary and, therefore, tertiary structure (Fig. 3*A*). We next asked whether impaired processivity of Fhod-A and Fhod-E requires a specific region or simply relates to tail length. Because the tails are unfolded, we reasoned that we could truncate the tail without disrupting the formin structure. We truncated the last 24 residues of Fhod-A (Fhod-AΔ24, identical to truncating the last 18 residues of Fhod-E), the last 50 residues of Fhod-A (Fhod-AΔ50), and the last 75 residues of Fhod-A (Fhod-AΔ75) (Fig. 3*B*). Truncating the last 99 residues of Fhod-A leaves Fhod-B (Fig. 3*B*). We then analyzed actin elongation in the presence of each Fhod-A tail truncation *via* TIRF microscopy and compared these results with both Fhod-A and Fhod-B (Fig. 3*C*). All tested Fhod-A tail truncations processively elongated actin filaments based on the presence of dim filaments and their increased elongation rates relative to the bright filaments (Fig. 3, *C* and *D*). The median run length (at t = 5 min) for each construct appears slightly shorter than that

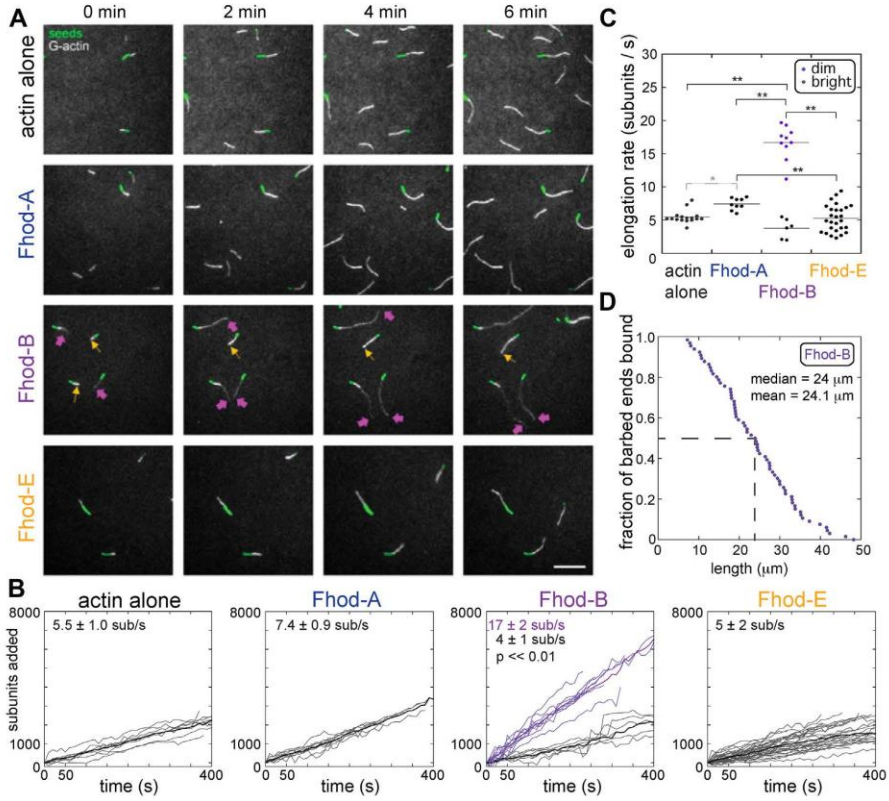

Figure 2. Fhod-B is a processive elongator. *A*, direct observation of barbed-end elongation by total internal reflection fluorescence microscopy with 0.5-nM seeds (1% biotinylated, labeled with Alexa Fluor 647-phalloidin; *green*), 1 μM G-actin (20% *Oregon green labeled; white*), 5 μM Chic (*Drosophila* profilin), ± 0.5 nM indicated Fhod construct. *Yellow arrows* denote the barbed-ends of *bright*, slow-growing filaments (no Fhod bound). *Magenta arrows* denote the barbed-ends of *dim*, fast-growing filaments (Fhod bound). The scale bar represents 10 μm. *B*, quantification of elongation from (*A*). *Fine gray* traces denote bright, slow-growing filaments. *Fine purple traces denote dim*, fast-growing filaments. *Thick gray* and *purple traces* denote means of the bright and dim growing populations, respectively. Elongation rates at the top of each plot are the mean ± standard deviation from ≥2 flow chambers for each condition (n = 16, actin alone; n = 9, Fhod-A; n = 10 [*dim*] and n = 6 [*bright*], Fhod-B; n = 27, Fhod-E). Fhod-B bright *versus dim* were compared with a two-tailed Student's t test. *C*, comparison of elongation rates for Fhod isoforms. *Lines* indicate the means. *Dim* filaments elongating in the presence of Fhod-B were significantly faster than all three other conditions. $^{**}p < 0.01$, $^{*}p < 0.05$, p values were determined with a one-way ANOVA and Tukey HSD *post hoc* tests. If no value is indicated, $p > 0.05$. *D*, measurement of Fhod-B processivity shown as an empirical cumulative distribution function plot. Data points are from three experimental replicates (n = 66 filaments). The *dashed line* indicates the median of the combined samples (24 μm). The mean ± standard deviation of the three independent samples is 24.1 ± 0.6 μm.

of Fhod-B (19.4–20.6 μm, number of filaments for each given in Fig. 3*E*), but there was no correlation between the decrease in processivity and the number of residues truncated (Fig. 3*E*). Together, these data show that Fhod processivity does not reflect the length of the tail and instead suggest that the last 24 residues of the Fhod-A tail (or the last 18 residues of the Fhod-E tail) are required to impair Fhod's processivity (Fig. 3*B*).

Examination of the primary sequences reveals a highly conserved basic region that extends beyond the traditional definition of the DAD but could be a continuation of this domain (Fig. 3*B*). This basic region straddles the Δ24 truncation site. To determine whether this region was responsible for loss of processivity, we made one further truncation, only removing 15 residues from the Fhod-A tail. Similar to wildtype Fhod-A, filaments grown in the presence of Fhod-AΔ15 were exclusively bright and grew at an average rate indistinguishable from actin alone (Fig. 3*D*). The data indicate that the nine residues immediately adjacent to the DAD basic region are necessary to inhibit processivity, although we do not know if they are also sufficient.

A one-way ANOVA revealed a statistically significant difference in the elongation rates of at least two groups in Figure 3*C*. A Tukey Kramer *post hoc* test showed that the mean values of the elongation rates for the three processive truncations were not significantly different from each other (summary tables are in Supplementary Information). However, the test indicated that Fhod-AΔ24 and Fhod-AΔ75 were significantly different from Fhod-B. A difference is unexpected

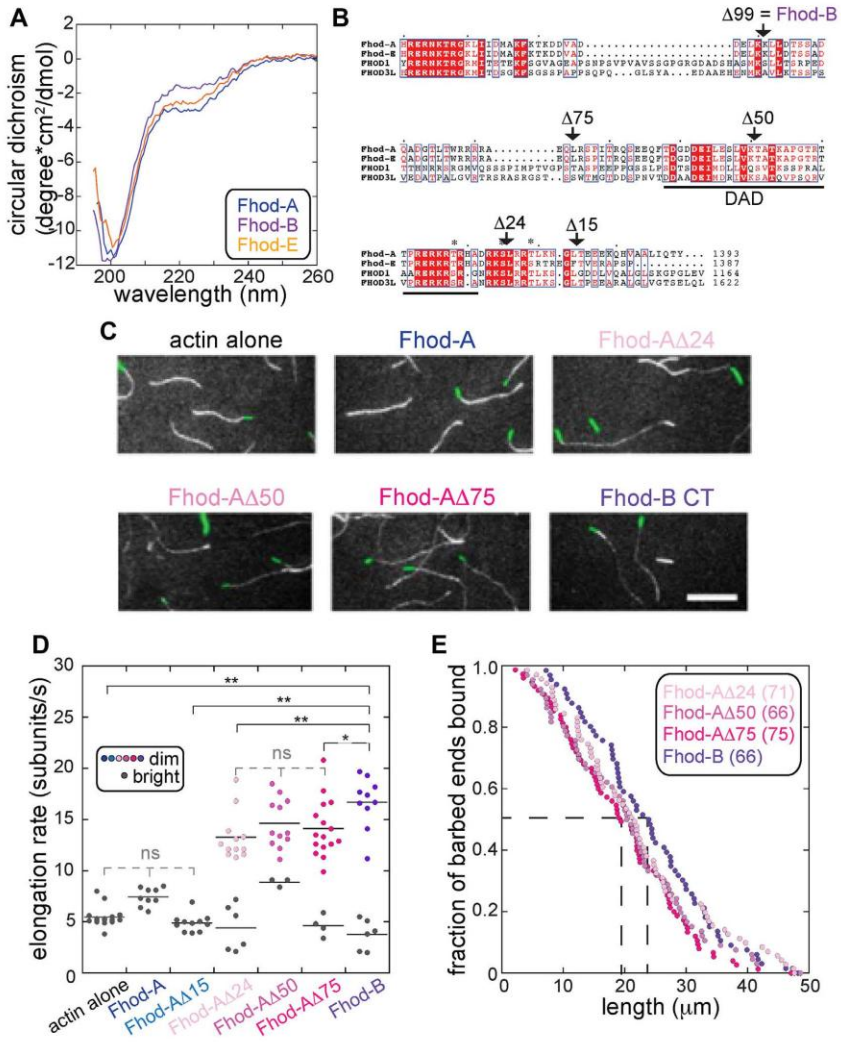

Figure 3. Residues at the end of the Fhod-A tail inhibit processivity. *A*, wavelength scans of circular dichroism indicate that Fhod tails are disordered. *B*, alignment of two *Drosophila* and two human Fhod tails. Truncation points for subsequent experiments are indicated. *Asterisks* denote phosphorylated residues (24). *C*, direct observation of barbed-end elongation by total internal reflection fluorescence microscopy. Conditions are the same as in Figure 2. Images were acquired 10 min after the start of polymerization. The scale bar represents 10 μm. *D*, quantification of elongation rates; ≥2 flow chambers for each condition. *Bright* filaments are represented by *gray dots* and *dim* filaments are colored. *Lines* indicate the means. $^{**}p < 0.01$, $^{*}p < 0.05$, $^{ns}p > 0.05$, *p* values were determined with a one-way ANOVA and Tukey HSD *post hoc* tests. *Bright* filaments were excluded from analysis between constructs if dim filaments were observed. Difference between the three truncation constructs were not significant. *E*, measurement of processivity shown as an empirical cumulative distribution function plot. Data points are from three experimental replicates (the number of filaments analyzed for each construct is given in the figure). The *dashed lines* indicate the medians (19.4–20.6 μm). The mean ± standard deviation of the three independent samples for each construct is 22.5 ± 0.3 μm (Fhod-AΔ24), 20.8 ± 0.7 μm (Fhod-AΔ50), 19.9 ± 0.6 μm (Fhod-AΔ75), and 24.1 ± 0.6 μm (Fhod-AΔ99 = FhodB).

because tails of previously studied formins (*e.g.*, mDia1 and Capu) do not change elongation rates (12, 13). Here, the difference is not large (for example, Fhod-AΔ75 [14 ± 3, n = 16] and Fhod-B [17 ± 3, n = 10]). If real, it suggests that a region of the tail within the first 25 residues is sufficient to slightly delay FH2 stepping.

Fhod tails decrease nucleation

Formin tails also contribute to nucleation (12, 13). We, therefore, examined the impact of the different Fhod tails on the initial step of actin assembly. We performed both pyrene assays and TIRF microscopy. All three isoforms accelerated actin assembly in pyrene assays compared with actin alone but

at different rates (Fig. 4*A*). Because pyrene assays report the product of nucleation and elongation, we confirmed that increased activity in the pyrene assay reflected, at least in part, nucleation, by spotting on coverslips actin polymerized in the absence or presence of Fhod isoforms. All three isoforms greatly enhanced the number of filaments per field of view relative to actin alone (Fhod-E shown as representative, Fig. 4*B*) (19). In order to be able to separate the impact on nucleation from elongation, we measured the elongation rates of each isoform without added profilin (to match the conditions used in Fig. 4, *A* and *B*) using TIRF microscopy. All three isoforms were processive in the absence of profilin, unlike what we observed in the presence of profilin. The rates were significantly slower than actin alone but indistinguishable between tails (Fig. 4*C*). We occasionally observed brief pauses. The elongation rates before and after a pause were the same. Perhaps the Fhod-FH2 domain can be in two different states: one with gating factor of ~0.5 and another with gating close to 0, which is rarely occupied under these conditions.

We also measured the activity of the Fhod-A tail truncation constructs in pyrene assays. These assays show a trend of increasing actin assembly as the tail is shortened (Fig. 4*D*). Because the elongation rates for Fhod-A and -B were indistinguishable in the absence of profilin, we assume that the elongation rates of the truncations are also the same as Fhod-A and Fhod-B (in the absence of profilin). It follows that nucleation is gradually increased with tail truncation. Thus, the longer Fhod tails inhibit nucleation, analogous to their effect on processivity, but through distinct mechanisms since only nucleation changes gradually with tail length. Electrostatics may be more important for nucleation than elongation, for Fhod.

Tails are major determinants of formin processivity

To examine how potent the enhancing and inhibitory effects of tails can be, we built chimeras (Fig. 5*A*). We chose Capu, a highly processive formin (λ ~250 μm; Fig. 5, *A*, *B*, and *D*) and Delphilin, a formin that has little, if any, tail or processivity (Fig. 5, *A*–*C*) (13, 20, 21). First, we asked whether the Fhod-A tail is sufficient to inhibit even the strong processivity of Capu. Indeed, when we replaced the 30-residue tail of Capu with the ~100-residue tail of Fhod-A, all evidence of processivity was lost and actin elongation was indistinguishable from actin alone (Fig. 5*E*). Because we previously found that the Capu construct lacking its tail (Capu1-1031) retains processivity

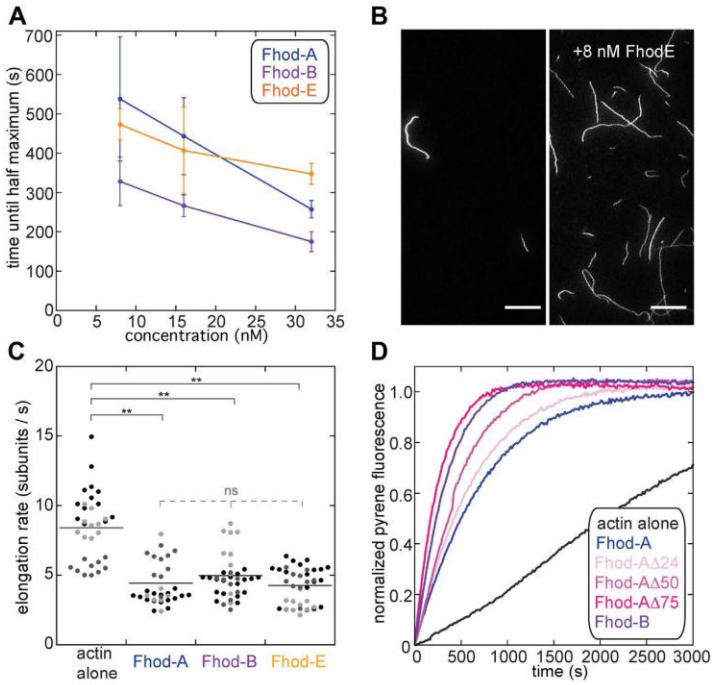

Figure 4. Fhod tails decrease nucleation. *A*, average time until half maximum polymerization measured from assembly reactions with 2 μM (10% pyrene-labeled) actin and 8 to 32 nM of indicated Fhod constructs. (n = 3 for all conditions; bars represent standard deviations.) *B*, actin, 2 μM, was polymerized in the presence or absence of 8 nM Fhod-E for 5 min, stabilized with Alexa Fluor 488-phalloidin, and imaged by total internal reflection fluorescence microscopy. The scale bars represent 10 μm. *C*, comparison of elongation rates for Fhod isoforms without profilin, 0.5 μM G-actin (20% *Oregon green*). Shades of gray represent independent replicates (n = 3 for each condition). *Lines* indicate the means. $^{**}p < 0.01$, $^{ns}p > 0.05$, *p* values were determined with a one-way ANOVA and Tukey HSD *post hoc* tests. All three constructs were slower than actin alone. Differences between Fhod-A, -B, and -E were not significant. *D*, representative kinetic traces of pyrene actin assembly assays with 2 μM (10% pyrene-labeled) actin and 8 nM of indicated Fhod constructs.

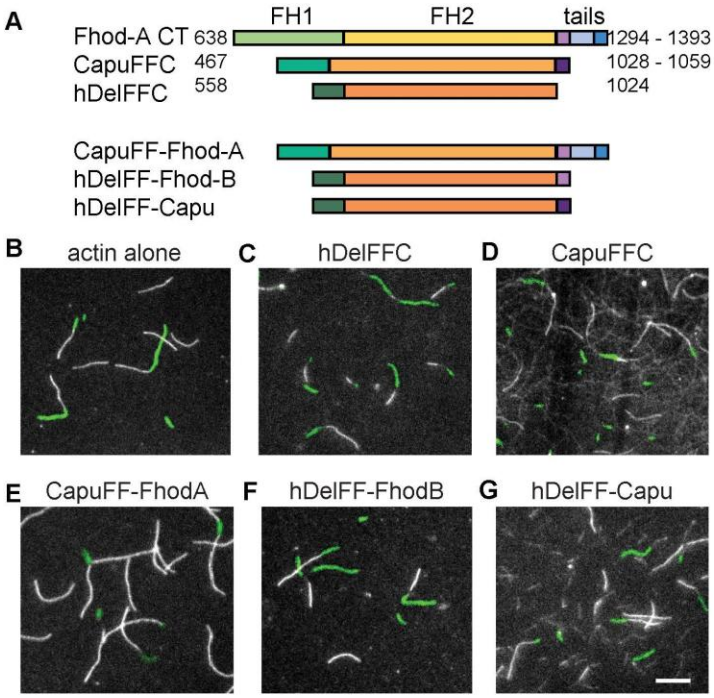

Figure 5. Tails determine processivity. *A*, cartoons of chimeras between FH1FH2 domains and tails of multiple formins. *B-G*, direct observation of barbed-end elongation by total internal reflection fluorescence microscopy. Conditions are the same as in Figure 2 except the indicated construct was added at different concentrations (*C*, hDelFFC = 15 nM, *D*, CapuCT = 1 nM, *E*, CapuFhodA = 0.5 nM, *F*, hDelFhodB = 15 nM, *G*, hDelCapu = 15 nM). The scale bar represents 10 μm.

(λ ~75 μm) (13), we conclude that the Fhod-A tail inhibits processivity. To ask if a tail is sufficient to impart processivity, we added the tails of Fhod-B and Capu to the FH1FH2 of Delphilin (hDelFF). With the Fhod-B tail we observed only short dim stretches, not obviously different from those we occasionally observed for wildtype Delphilin (Fig. 5, *C* and *F*). On the other hand, the Capu tail greatly enhanced processivity of Delphilin, based on the long, dim filaments observed in these assays (Fig. 5, *D* and *G*). Thus, formin tails can enhance the processivity of the FH2 domain, with the Capu tail even overcoming the inherently weak processivity of Delphilin. In sum, the tails determine whether or not a formin is processive.

Discussion

Multiple Fhod tails are used

Drosophila Fhod contributes to many different functions, such as programmed cell death in the salivary gland, myogenesis, and immune response (15, 16, 18). *Drosophila* only have one Fhod gene, *fhos*, but nine splice variants are annotated in Flybase (14). We propose that splice variants are necessary for the wide range of roles. There is already clear evidence for differential expression of splice variants that vary in their N termini: Fhod-A is sufficient to rescue the lethality and wing phenotypes of $Fhos^{\Delta 1}$, a presumptive null (16). However, severe flight muscle phenotypes are observed when Fhod-A is the only variant expressed. Instead, Fhod-H, I, and/or J are responsible for proper localization of Fhod, in developing muscle, which is required for thin filament formation (15). These longer isoforms contain distinct 5′ regions, including exons and introns, but they all have the same tail as Fhod-A. While the N-terminal half of formins contribute to autoinhibition it is also the most variable region and is often responsible for specific localization and/or binding interactions.

We asked if by changing the C terminus of the formin one could alter the actin assembly activity, essentially creating formins capable of building distinct structures. Our data indicating that Fhod-A tail mRNA is present through development are consistent with the known ability of Fhod-A to rescue viability. Interestingly, mRNA of the Fhod-E tail is expressed only after eclosion. The Fhod-E tail is expressed at increasing levels in the young adult, eventually reaching a level comparable with Fhod-A (based on read number), suggesting that it plays a widespread role in the adult fly. In contrast, Fhod-B and -D were not detectable by this method. Each represents a unique transcript. In preliminary RT-PCR experiments, we saw evidence of both Fhod-B and -D but at levels too low to quantify (data not shown). Perhaps they are each expressed in only one or a few tissue types. Notably, Fhod-B lacks a DAD domain and, presumably, cannot be

autoinhibited. If this is truly a constitutively active formin, it seems judicious to tightly control its expression levels.

Processivity

Processivity (the dissociation rate of a formin from a barbed end) and the elongation rate determines the average filament length built by a formin (also called the characteristic run length). Studies of processivity show that the dissociation rate is correlated with the elongation rate, suggesting that the FH2–barbed end interaction is weakened in response to addition of actin monomers to the barbed end (9, 22). In addition, it has been shown that mDia1's processivity is highly sensitive to force (22). Processivity is presumably a property of the specific FH2 domain bound to a barbed end. Experiments with altered ionic strength show that electrostatic interactions play an important role, and molecular dynamics simulations of bound barbed ends provide corroborating evidence for electrostatic interactions at the FH2–barbed end interface (22, 23). However, processivity is also influenced by the two regions that straddle the FH2 domain: the FH1 domain and the C-terminal tail (13, 22). Processivity enhancement by the FH1 domain depends on profilin and is proposed to be stabilization by ring closure, suggesting that the weak state, perhaps translocation of the trailing FH2 half, occurs upon actin monomer addition (22). Thus, we were surprised to find the apparently high processivity of Fhod in the absence of profilin, while the processivity of Fhod-A and Fhod-E are negligible in the presence of profilin. We qualify the claim of high processivity because we cannot be sure that the formins are on the barbed ends 100% of the time. We observe constant elongation rates within the time resolution of our experiments (seconds), but elongation could be slowed by capping that switches between "on" and "off" of the barbed end at a higher rate. The occasional pauses we observed could also be an indicator of Fhod's ability to switch gating states rapidly, for example.

We previously hypothesized that the Capu-tail increased processivity through nonspecific electrostatic interactions with the actin filament, which aligns with ionic strength assays (13, 22). Perhaps not surprisingly, we found that the tail's influence on processivity is more complex in some cases. The pI's of the Fhod-A and Fhod-E tails are higher than that of Fhod-B yet lower than or similar to other tails that support processivity (*e.g.*, Capu and FMNL1 (13)) (Fig. 1*B*). Combined with the lack of correlation between processivity and length of truncation, we can rule out simple electrostatics to explain why Fhod-A and Fhod-E are not processive. We attempted to perform cosedimentation assays with isolated tails to measure their affinities for actin filaments. Unfortunately, owing to nonspecific binding at higher tail concentrations, the data did not plateau and we could not make interpretable measurements.

At first, we did not know if the low processivity of Fhod-A (λ = ~2 um) was inherent to the FH2 domain and/or due to its tail. Based on our previous observations with Capu, and the length of the FhodA-tail (99 AA), we hypothesized that the FH2 domain was not capable of processive elongation and even a long tail could not overcome the weak interaction. Instead, we found that Fhod-B, with a shorter tail (that is included in the Fhod-A tail), is 10-fold more processive. It follows that the Fhod-FH2 domain can support processive actin elongation but the time that it remains bound depends on the tail. Consistent with this conclusion, we found that the tail determined whether or not multiple chimeras were processive. Notably, adding the Capu tail to Delphilin enabled Delphilin to processively elongate filaments.

There appears to be a marked difference between Fhod and Capu in how their FH2 domains and tails contribute to processivity. The data demonstrate that tail length and pI, which correlate with processivity in some formins, do not predict processivity for Fhod isoforms. So how does the Fhod-A tail inhibit processivity of the FH2 domain? We found that a stretch of basic amino acids extending beyond DAD is necessary to inhibit processivity. All three long Fhod tails as well as both mammalian Fhod isoforms contain additional basic residues that extend past the typical DAD. This basic region might directly bind to the FH2 domain to decrease its processivity. We do not favor this model because the Fhod-A tail was also able to inhibit processivity by the unrelated FH2 domain of Capu. Alternatively, the extended basic region could bind the sides of actin filaments "too tightly," pulling the FH2 domain off of the barbed end instead of loosely stabilizing it. As stated, we were unable to test this model directly.

Within the DAD domain and the adjacent inhibitory region that we identified are three well-documented phosphorylation sites (Fig. 3*B*). Studies with both Fhod-A and mammalian homologs show that Rho-dependent kinase (ROK/ROCK) phosphorylates these sites (16, 24). Phosphorylation of these residues is sufficient to release the autoinhibitory interaction in pull-down assays and activate the formins in tissue culture experiments (16, 24). For example, expressing Fhod3 with phosphomimetic S -> D mutations in HeLa cells resulted in higher filamentous actin levels compared with expressing wildtype Fhod. However, the analogous mutations did not alter the chemistry of the tail enough to make Fhod-A processive (not shown). This leaves us with the question of whether there is a mechanism to convert Fhod-A and -E into more processive elongation factors. Alternatively, low processivity may be essential to building shorter filaments, such as the thin filaments in sarcomeres and stress fibers that are assembled by Fhod-family formins. Thin filaments are typically ~1 μm long. Thus, Fhod-A's characteristic run length of ~2 μm is sufficient and well suited to build such structures. Perhaps, Fhod-family formins have evolved away from the highly processive formins.

In sum, the role of formins tails was originally believed to be restricted to all or nothing regulation through autoinhibition. In fact, many experiments have been performed with constructs lacking the tail, in order to create a constitutively active formin. We now know that formin tails can have dramatic effects on nucleation and elongation and, therefore, should not be ignored.

Experimental procedures

Construct cloning and purification

All constructs were built from Fhod isoform A cDNA (clone SD08909, obtained from the *Drosophila* Genomics Resource

Center). The cDNA was used as a template to clone C-terminal constructs into either a modified version of the pET-15b plasmid with an N-terminal His_6 tag (Fhod-A, Fhod-AΔ15, Fhod-AΔ24, Fhod-AΔ50, Fhod-AΔ75, and Fhod-E) or a pGEX-6P-2 plasmid (Fhod-B and Fhod-A,-B,-E tails). All truncated tail constructs were produced *via* FastCloning (25). The Fhod-E exon was synthesized and added by Gibson Assembly.

All constructs were expressed in Rosetta I cells, induced with 0.25 mM ITPG and grown overnight, shaking, at 18 °C.

Fhod-A, Fhod-AΔ15, Fhod-AΔ24, Fhod-AΔ50, Fhod-AΔ75, and Fhod-E

Purification was performed as described (19). In brief, these constructs were purified using a HiTrapSP-FF cation exchange column (GE Life Sciences) followed by a MonoQ anion exchange column (GE Life Sciences). Peak fractions were dialyzed into Fhod storage buffer (10 mM Tris, pH 8.0, 150 mM NaCl, 1 mM DTT). The purified constructs were aliquoted, flash frozen using liquid nitrogen, and stored at −80 °C.

Fhod-B

Purification was carried out using glutathione sepharose resin. The eluted protein was dialyzed in PBS with 1 mM DTT and cleaved with Precission Protease overnight. The cleaved protein was filtered through glutathione sepharose and dialyzed into 10 mM Tris, pH 8.0 50, mM NaCl, 1 mM DTT. It was next run on a MonoQ anion exchange column (GE Life Science). Peak fractions were dialyzed into Fhod storage buffer. Aliquots were stored at −80 °C.

Fhod tails

Initial purification of Fhod tails was carried out using glutathione Sepharose resin as described for Fhod-B. Protein was eluted with 50 mM Hepes, pH 7.3, 50 mM NaCl, 1 mM DTT, 20 mM glutathione. This buffer is similar to PBS but has better buffering capacity for the glutathione and is at slightly lower salt concentration for direct loading on a MonoS cation exchange column (GE Life Sciences). The GST tag was cleaved with Precission Protease overnight and then purified with a step from 50 mM to 600 mM NaCl on the MonoS column (GST does not bind to this column). Peak fractions were dialyzed into 10 mM Tris, pH 8.0, 50 mM NaCl, 0.5 mM TCEP for storage. Aliquots were stored at −80 °C. Fresh protein was treated as described below for CD spectroscopy.

Acanthamoeba castellanii actin and *Drosophila* profilin (Chic) were purified as described (26, 27). Actin was labeled with pyrene-iodoacetamide (27), Oregon Green 488-iodoacetamide (Invitrogen) (26), or EZ-link maleimide-PEG2-biotin (Thermo Scientific) (28) as described.

Pyrene assays

Bulk actin polymerization assays were performed on an Infinite 200 Pro plate reader (Tecan) essentially as described (26). In brief, 2 μM 10% pyrene-labeled actin monomers were incubated for 2 min in ME buffer (200 μM ethylene glycol tetraacetic acid [EGTA] and 50 μM $MgCl_2$) to convert Ca^{2+}-actin to Mg^{2+}-actin. Polymerization was initiated by adding KMEH buffer (final concentration: 10 mM Na-Hepes, 1 mM EGTA, 50 mM KCl, and 1 mM $MgCl_2$) to the Mg^{2+}-actin. Fhod constructs were added to the KMEH buffer before addition to Mg^{2+}-actin, at indicated concentrations. To complement nucleation assays, we polymerized actin under the same conditions and stopped the reaction after 5 min by adding Alexa Fluor 488 phalloidin. Samples were then diluted and spotted on poly-L-lysine-coated coverslips.

TIRF microscopy

TIRF microscopy was utilized to measure the elongation rates and processivity of the Fhod constructs. Biotinylated coverslips were prepared as described (19). Flow chambers of ∼15 μl were assembled on slides with strips of double-sided tape. Flow chambers were prepared with the following steps: (1) incubated for 2 min with block containing 25 μl of 1% Pluronic F-127 (Sigma), 50 μg/ml casein in PBS; (2) washed with 25 μl of KMEH; (3) incubated for 1 min with 25 μl of 40 nM streptavidin in KMEH; (4) washed with 25 μl of TIRF buffer (KMEH, 0.5% methylcellulose [400 cP, Sigma], 50 mM DTT, 0.2 mM ATP, 20 mM glucose). A 2× stock of Fhod construct and F-actin seeds was incubated for 45 s prior to addition of an equal volume of Mg^{2+}-G-actin. Oregon green–labeled G-actin was incubated with *Drosophila* profilin for 2 min in ME buffer to convert Ca^{2+}-actin to Mg^{2+}-actin. The final concentrations in the flow chambers were as follows: 1 μM Mg^{2+}-G-actin (20% Oregon green labeled) in KMEH, 5 μM profilin (except in experiments shown in Fig. 4), 0.5 nM (unless otherwise indicated) Fhod construct, 0.5 nM F-actin seeds (1% biotinylated, stabilized with Alexa Fluor 647-phalloidin), 250 μg/ml glucose oxidase, 50 μg/ml catalase, and 50 μg/ml casein in TIRF buffer. Most experimental data were acquired with a DMI6000 TIRF microscope (Leica) with an HCX PL APO objective (100 × magnification, N.A. = 1.47) and an Andor DU-897 camera, using the Leica application suite advanced fluorescence software. The data in Figures 4 and 5 were acquired with a Zeiss Axio Observer 7 Basic Marianas Microscope with Definite Focus 2 equipped with a 3i Vector TIRF System, an Alpha Plan-Apochromat 63×/1.46NA Oil TIRF Objective, and an Andor iXon3 897 512x512 10 MHz EMCCD Camera, using Slidebook 6 software. Experiments were performed at room temperature. Images were captured at 10-s intervals for 10 min. Filament lengths were quantified with the JFilament plug-in in FIJI (29).

Circular dichroism spectroscopy

Freshly purified protein stocks were dialyzed into 50 mM potassium phosphate (pH 7.5), 1 mM DTT and then precleared by centrifugation at 100,000*g* for 20 min at 4 °C. CD spectra were measured on a J-715 spectropolarimeter (Jasco) by averaging two wavelength scans from 195 to 260 nm.

Nanopore sequencing

D. melanogaster w^{1118} flies were collected at different developmental stages: third instar larva, pupa, and days 1, 3, and 5 post

eclosion. Total RNA was extracted by freezing flies for 10 min in TRIzol Reagent (ThermoFisher Scientific, catalog #15596026) and grinding with a pestle. Homogenized samples were then centrifuged at 12k rpm for 30 s to remove fly debris. The supernatant was transferred to a new tube, chloroform extracted, and centrifuged at 10k rpm for 15 min. The rest of the RNA purification was performed using the Direct-zol RNA MiniPrep Kit (Genesee Scientific, catalog #11-330) and Zymo-Spin IIICG columns (Zymo Research, catalog #C1006-50-G) as per the manufacturer's instructions with a minor change in the flowthrough step, which was centrifuged for 2k rpm for 2 min and repeated once more. cDNA was synthesized using SuperScript III (ThermoFisher Scientific, catalog #18080093) using an Oxford Nanopore sequence 5′ ACTTGCCTGTCGCTCTATCTTC oligo$(dT)_{18}$ 3′. Ethanol precipitation was performed to purify and concentrate the cDNA. The purity and concentration were assessed with a NanoDrop. The cDNA was then amplified with Phusion High-Fidelity DNA Polymerase (New England Biolabs, catalog #M0530S) using the following steps: initial denaturation 98 °C, 0:30; 30 cycles 98 °C, 0:30, 64 °C, 0:30, 72 °C, 1:30, final extension 72 °C, 5:00, and infinite hold 4 °C. Standard 40-uL reaction was followed but with a 3× increase in forward primer.

Forward primer: 5′ TTTCTGTTGGTGCTGATATTGCA TGATACCGCAGGTGGTGGG 3′

(Note that the Nanopore sequence TTTCTGTTGGT GCTGATATTG is not needed after switching from the PCR Sequencing Kit to the Native Barcoding Kit but was used for ease).

Reverse primer: 5′ ACTTGCCTGTCGCTCTATCTTC 3′

Ethanol precipitation was performed to purify and concentrate the PCR amplicons. The purity and concentration were assessed using a NanoDrop.

Nanopore libraries were prepared from 130 ng of Fhos amplicons using the Native Barcoding Kit 24 V14 from Oxford Nanopore (ONT, catalog #: SQK-NBD114.24) as per the manufacturer's instructions. Sequencing was performed using R10.4.1 flow cells on a MinION Mk1B device and sequenced for 48 h. Basecalling was performed using Guppy Basecaller (Version 6.4.6). Reads were then mapped to a *FHOS* reference sequence obtained from NCBI (Gene ID: 39004) using Minimap 2 (Version 2.17-r941). Reads were visualized using IGV (Version 2.12.3), and figures were prepared using Inkscape (Version 1.1.2).

Statistical analysis

Elongation rates were analyzed two ways: (1) If dim and bright filaments were detected for a given construct, a two-tailed Student's t test with equal variance was performed. The mean elongation rates of dim *versus* bright filaments were significantly different, $p < 0.05$, in all cases. (2) To compare sets of data, bright filaments were excluded from samples that had dim filaments. A one-way ANOVA was performed to compare the elongation rates as a function of formin isoform/construct. A Tukey Kramer *post hoc* test was used to further examine the data in pairwise sets. Summary tables of these tests are included in Supporting information.

Data availability

All data will be shared upon request sent to the corresponding author.

Supporting information—This article contains supporting information.

Acknowledgments—The authors would like to thank the entire Quinlan lab for support and useful discussions throughout this project. Thanks especially Margo Myers and Bryan Christian, who did some important thinking and supporting experiments. Thanks also to Theodosia Bartashevitch for qPCR experiments that inspired the nanopore sequencing work.

Author contributions—K. V. B., A. A. P., A. M. G., M. E. Q. conceptualization; C. W., K. L. H., G. F. C. methodology; K. V. B., C. W., K. L. H., M. E. Q. formal analysis; K. V. B., C. W., A. A. P., K. L. H., A. M. G. investigation; K. V. B. writing – original draft; C. W., A. A. P., K. L. H., A. M. G., G. F. C., M. E. Q. writing – review & editing.

Funding and additional information—This work was supported by National Institutes of Health Grants under Award Numbers T32 GM145388 (to C. W.), R35 GM130370 (to G. F. C.), and R01 HL14659 (to M. E. Q.). The content is solely the responsibility of the authors and does not necessarily represent the official views of the National Institutes of Health.

Conflict of interest—The authors declare that they have no conflicts of interest with the contents of this article.

Abbreviations—The abbreviations used are: Capu, Cappuccino; CD, circular dichroism; DAD, diaphanous autoregulatory domain; FH, formin homology; Fhod, formin homology domain; TIRF, total internal reflection fluorescence.

References

1. Goode, B. L., and Eck, M. J. (2007) Mechanism and function of formins in the control of actin assembly. *Annu. Rev. Biochem.* **76**, 593–627
2. Courtemanche, N. (2018) Mechanisms of formin-mediated actin assembly and dynamics. *Biophys. Rev.* **10**, 1553–1569
3. Breitsprecher, D., and Goode, B. L. (2013) Formins at a glance. *J. Cell Sci* **126**, 1–7
4. Valencia, D. A., and Quinlan, M. E. (2021) Formins. *Curr. Biol.* **31**, R517–R522
5. Xu, Y., Moseley, J. B., Sagot, I., Poy, F., Pellman, D., Goode, B. L., *et al.* (2004) Crystal structures of a Formin Homology-2 domain reveal a tethered dimer architecture. *Cell* **116**, 711–723
6. Kovar, D. R., and Pollard, T. D. (2004) Insertional assembly of actin filament barbed ends in association with formins produces piconewton forces. *Proc. Natl. Acad. Sci. U. S. A.* **101**, 14725–14730
7. Pruyne, D., Evangelista, M., Yang, C., Bi, E., Zigmond, S., Bretscher, A., *et al.* (2002) Role of formins in actin assembly: nucleation and barbed-end association. *Science* **297**, 612–615
8. Kovar, D. R., Harris, E. S., Mahaffy, R., Higgs, H. N., and Pollard, T. D. (2006) Control of the assembly of ATP- and ADP-actin by formins and profilin. *Cell* **124**, 423–435
9. Paul, A., and Pollard, T. (2008) The role of the FH1 domain and profilin in formin-mediated actin-filament elongation and nucleation. *Curr. Biol.* **18**, 9–19
10. Li, F., and Higgs, H. N. (2005) Dissecting requirements for autoinhibition of actin nucleation by the formin, mDia1. *J. Biol. Chem.* **280**, 6986–6992

11. Alberts, A. S. (2001) Identification of a carboxyl-terminal diaphanous-related formin homology protein autoregulatory domain. *J. Biol. Chem.* **276**, 2824–2830
12. Gould, C. J., Maiti, S., Michelot, A., Graziano, B. R., Blanchoin, L., and Goode, B. L. (2011) The formin DAD domain plays dual roles in autoinhibition and actin nucleation. *Curr. Biol.* **21**, 384–390
13. Vizcarra, C. L., Bor, B., and Quinlan, M. E. (2014) The role of formin tails in actin nucleation, processive elongation, and filament bundling. *J. Biol. Chem.* **289**, 30602–30613
14. Gramates, L. S., Agapite, J., Attrill, H., Calvi, B. R., Crosby, M. A., dos Santos, G., *et al.* (2022) FlyBase: a guided tour of highlighted features. *Genetics* **220**, iyac035
15. Shwartz, A., Dhanyasi, N., Schejter, E. D., and Shilo, B.-Z. (2016) The Drosophila formin Fhos is a primary mediator of sarcomeric thin-filament array assembly. *Elife* **5**, e16540
16. Lammel, U., Bechtold, M., Risse, B., Berh, D., Fleige, A., Bunse, L., *et al.* (2014) The Drosophila FHOD1-like formin Knittrig acts through Rok to promote stress fiber formation and directed macrophage migration during the cellular immune response. *Development* **141**, 1366–1380
17. Anhezini, L., Saita, A. P., Costa, M. S. A., Ramos, R. G. P., and Simon, C. R. (2012) Fhos encodes a Drosophila Formin-Like Protein participating in autophagic programmed cell death. *Genesis* **50**, 672–684
18. Johansson, K. C., Metzendorf, C., and Söderhäll, K. (2005) Microarray analysis of immune challenged Drosophila hemocytes. *Exp. Cell Res.* **305**, 145–155
19. Patel, A. A., Durer, Z. A. O., van Loon, A. P., Bremer, K. V., and Quinlan, M. E. (2018) Drosophila and human FHOD family formin proteins nucleate actin filaments. *J. Biol. Chem.* **293**, 532–540
20. Yoo, H., Roth-Johnson, E. A., Bor, B., and Quinlan, M. E. (2015) Drosophila Cappuccino alleles provide insight into formin mechanism and role in oogenesis. *Mol. Biol. Cell* **26**, 1875–1886
21. Silkworth, W. T., Kunes, K. L., Nickel, G. C., Phillips, M. L., Quinlan, M. E., and Vizcarra, C. L. (2018) The neuron-specific formin Delphilin nucleates nonmuscle actin but does not enhance elongation. *Mol. Biol. Cell* **29**, 610–621
22. Cao, L., Kerleau, M., Suzuki, E. L., Wioland, H., Jouet, S., Guichard, B., *et al.* (2018) Modulation of formin processivity by profilin and mechanical tension. *Elife* **7**, e34176
23. Baker, J. L., Courtemanche, N., Parton, D. L., McCullagh, M., Pollard, T. D., and Voth, G. A. (2015) Electrostatic interactions between the Bni1p formin FH2 domain and actin influence actin filament nucleation. *Structure* **23**, 68–79
24. Iskratsch, T., Reijntjes, S., Dwyer, J., Toselli, P., Dégano, I. R., Dominguez, I., *et al.* (2013) Two distinct phosphorylation events govern the function of muscle FHOD3. *Cell. Mol. Life Sci.* **70**, 893–908
25. Li, C., Wen, A., Shen, B., Lu, J., Huang, Y., and Chang, Y. (2011) FastCloning: a highly simplified, purification-free, sequence- and ligation-independent PCR cloning method. *BMC Biotechnol.* **11**, 92
26. Bor, B., Vizcarra, C. L., Phillips, M. L., and Quinlan, M. E. (2012) Autoinhibition of the formin Cappuccino in the absence of canonical autoinhibitory domains. *Mol. Biol. Cell* **23**, 3801–3813
27. Zuchero, J. B. (2007) *In vitro* actin assembly assays and purification from Acanthamoeba. *Methods Mol. Biol.* **370**, 213–226
28. Roth-Johnson, E. A., Vizcarra, C. L., Bois, J. S., and Quinlan, M. E. (2014) Interaction between microtubules and the Drosophila formin Cappuccino and its effect on actin assembly. *J. Biol. Chem.* **289**, 4395–4404
29. Smith, M. B., Li, H., Shen, T., Huang, X., Yusuf, E., and Vavylonis, D. (2010) Segmentation and tracking of cytoskeletal filaments using open active contours. *Cytoskeleton (Hoboken)* **67**, 693–705
30. Lord, S. J., Velle, K. B., Mullins, R. D., and Fritz-Laylin, L. K. (2020) SuperPlots: communicating reproducibility and variability in cell biology. *J. Cell Biol* **219**, e202001064